

[COHERENT OPTICAL SHORT-REACH COMMUNICATIONS]

Di Che

Coherent Optical Short-Reach Communications

Di Che

Submitted in total fulfilment of the requirements of the degree of
Doctor of Philosophy

National ICT Australia - Victoria Research Laboratory

Department of Electrical and Electronic Engineering

The University of Melbourne

Parkville, VIC 3010, Australia

December 2016

Copyright © DI CHE

All rights reserved. No part of the publication may be reproduced in any form by print, photoprint, microfilm or any other means without written permission from the author.

ABSTRACT

Optical communication using high-speed on-off-keying by direct modulation (DM) and direct detection (DD) was one of the most inspiring breakthroughs for telecommunication in 1970s. The wide deployment of 2.5-Gb/s per wavelength submarine fiber links in 1990s helped drive the emergence of the Internet as a global phenomenon. However, the evolution of optical coherent detection during the last decade brought a thorough transformation for long-haul transmission, which completely substitutes the role of DM-DD and contributes a 10-time scaling of the fiber channel capacity.

Now, DM-DD still holds its position in optical short-reach applications, due to its natural advantage – the simplicity. With the ever-increasing Internet traffic demand, short-reach links require a capacity upgrade in line with the long-haul progression. There is no doubt that coherent detection will gradually penetrate to shorter distance to offer higher data-rate and better system performance than the conventional DM-DD. This thesis investigates how the coherent detection can be transformed to short reach communications cost-efficiently.

There are two fundamental transmission impairments for DM-DD systems: (i) chromatic dispersion (CD); (ii) DM laser frequency chirp. The CD-induced frequency selective fading generates nulls within the signal spectrum after DD, which brings severe inter-symbol interference (ISI). This thesis proposes a set of self-coherent detection subsystems to linearize the DD channel, which effectively overcomes the dispersion by digital compensation. DM frequency chirp used to be regarded as the performance barrier for DM-DD, because it expands the optical spectrum, making the signal much more sensitive to the dispersion impairment. For the first time, we show that the detrimental chirp can be converted to an advantage by coherent detection, which significantly improves the system OSNR sensitivity compared with the conventional DM.

Moreover, coherent detection enables powerful digital signal processing (DSP) to optimize system performance. This thesis involves a variety of DSP schemes for short reach applications, such as the OFDM modulation for high electrical spectral efficiency, maximum likelihood sequence estimation for optical channel with memory, adaptive equalization for ISI mitigation, digital polarization demultiplexing for multi-dimension direct detection, and advanced forward error corrections. The DSP offers economical solutions to overcome these impairments (or limitations) in short reach systems.

The thesis bridges the gap between DM-DD and standard coherent systems, aiming to accelerate the coherent detection application to short reach optical communications.

This is to certify that

- (1) the thesis comprises only my original work,
- (2) due acknowledgement has been made in the text to all other material used,
- (3) the thesis is less than 100,000 words in length, exclusive of table, maps, bibliographies, appendices and footnotes.

Signature

Date

DECLARATION

I hereby declare that this thesis comprises only my original work. No material in this thesis has been previously published and written by another person, except where due reference is made in the text of the thesis. I further declare that this thesis contains no material which has been submitted for a degree or diploma or other qualifications at any other university. Finally, I declare that the thesis is less than 100,000 words in length, exclusive of tables, figures, bibliographies, appendices and footnotes.

ACKNOWLEDGEMENTS

The work in this thesis cannot be fulfilled without the support, collaboration and assistance from many people, to whom I hope to express my sincere gratitude.

First, I would like to express my appreciation to my principle supervisor Prof. William Shieh and co-supervisor Dr. Trevor Anderson for their high-quality academic guidance and direction, which help develop my knowledges in optical communications quickly and lead me to the cutting-edge research fields. Their generous supports accompany me throughout the PhD candidature. My thank also goes to Prof. Tansu Alpcan, my PhD committee chair.

Second, I would like to express my appreciation to Dr. Fred Buchali at Bell Labs (Stuttgart, Germany), for offering me the internship opportunity in this world-leading research organization. His patient guidance provides me deeper understanding on not only the academia, but also the industry of this field.

Third, I would like to express my appreciation to the colleagues who collaborated with me during the past 4 years: Hamid Khodakarami, An Li, Xi Chen, Jiayuan He, Qian Hu, Yifei Wang, Feng Yuan, and Jian Fang. The research outcome is no doubt the teamwork from us together.

I would like to thank The University of Melbourne and National ICT Australia for their financial sponsoring of the PhD, the Photonics Research Lab in the Department of Electrical and Electronic Engineering for the outstanding research environment and facilities.

Last but not the least on a personal level, I would like to express my appreciation to my family for supporting me spiritually throughout completing this PhD.

CONTENTS

Abstract	i
Declaration	iii
Acknowledgements	iv
Contents	v
List of Figures	vii
List of Tables	ix
1. Introduction	1
1.1 Optical fiber communications	1
1.2 Digital coherent detection	3
1.3 State-of-the-art DM-DD short-reach applications	5
1.4 Bottlenecks of DM-DD short reach optical applications	8
1.5 Thesis contributions	12
1.6 Thesis outline	15
1.7 Author’s publications related to this thesis	17
2. Optical detection methods	21
2.1 Intensity-only direct detection	21
2.2 Self-coherent differential-phase detection	21
2.3 3-dimension direct detection in Stokes space	23
2.4 4-dimension coherent detection in Jones space	25
2.5 Optical detection methods in this thesis	25
3. Subcarrier reliability aware LDPC for CO-OFDM	27
3.1 Forward error correction codes in optical communication	27
3.2 Subcarrier reliability aware (SRA) soft-decision LDPC codes	30
3.3 Experiment demonstration of SRA-LDPC codes	33
3.4 Conclusions	38
4. Frequency chirp enabled complex modulation	39
4.1 Discrete signal model for laser frequency chirp	40
4.2 Chirp parameters characterization using coherent detection	42
4.3 Maximum likelihood sequence estimation (MLSE) for CDM	43
4.4 CDM PAM-4: approaching QPSK in terms of OSNR sensitivity	44
4.5 NRZ PAM-4 transmission experiment	47

4.6 Revisit MLSE: a probabilistic perspective	50
4.7 Nyquist-pulse-shaped PAM-4 transmission experiment.....	51
4.8 Towards high order PAM utilizing large frequency chirp.....	55
4.9 NRZ PAM-8 transmission experiment	59
4.10 Conclusions	60
5. Optical self-coherent subsystems	61
5.1 Why channel linearization?	62
5.2 Self-Coherent Modulation and Detection.....	63
5.3 Intensity Only 1-Dimension Direct Detection	64
5.4 Phase Diverse 2-Dimension Direct Detection	66
5.5 Discrete-time Gaussian Channel with Conjugate Intersymbol Interference	69
5.6 102.4-Gb/s single-polarization signal carrier interleaved direct detection	71
5.7 Conclusions.....	74
6. Stokes vector detection subsystems.....	75
6.1 Self-coherent Stokes space modulation.....	75
6.2 Polarization demultiplexing in Stokes space	76
6.3 Transmission experiments of Stokes vector direct detection.....	82
6.4 Experiment for polarization demultiplexing algorithms	88
6.5 PMD impact on Stokes vector direct detection	91
6.6 Comparison between different self-coherent subsystems.....	92
6.7 Conclusions.....	95
7. Multi-dimension polarization modulation	97
7.1 Multi-dimension Stokes-space modulation (SSM).....	98
7.2 Revisit polarization demultiplexing: a universal MIMO perspective	99
7.3 Frequency-domain MIMO in Stokes space	100
7.4 Polarization-multiplexed discrete multitone experiment.....	101
7.5 Conclusions.....	104
8. Summary	105
Abbreviations	109
Bibliography	113

LIST OF FIGURES

Figure 1.1 4-D optical field transmitter.....	8
Figure 1.2 Electrical spectra of IM-DD signal after dispersive fiber transmission	10
Figure 1.3 Power fading notch characteristics at difference fiber distance	11
Figure 1.4 Thesis contributions categorised by the transmission distance	12
Figure 2.1 Intensity-only direct detection receiver	21
Figure 2.2 B-DPSK self-coherent receiver.	21
Figure 2.3 M-DPSK self-coherent receiver	22
Figure 2.4 Stokes vector receiver.....	24
Figure 2.5 Dual-polarization coherent receiver	25
Figure 3.1 Encoding procedures for a linear block codes	28
Figure 3.2 LDPC (12,8) code. (a) Generating matrix; (b) Tanner graph	29
Figure 3.3 Concatenated LDPC and RS codes	30
Figure 3.4 Subcarrier assignments for SRA-LDPC encoding.....	31
Figure 3.5 Experimental setup for SRA-LDPC coding scheme in CO-OFDM systems.....	33
Figure 3.6 Subcarrier SNR distribution in CO-OFDM experiment	34
Figure 3.7 BER performance for all subcarriers and absolute value of LLR for LDPC value nodes within different subcarriers	35
Figure 4.1 Simulation procedures for obtaining the spectra with DM frequency chirp.....	41
Figure 4.2 10-Gbaud DM PAM-4 signal spectra.....	42
Figure 4.3 Training patterns for laser frequency chirp coefficients.....	42
Figure 4.4 Simulation setup for CDM coherent systems	44
Figure 4.5 SNR sensitivity comparison among 4-level modulations.....	45
Figure 4.6 SNR sensitivity comparison for CDM using different frequency chirp parameters...	46
Figure 4.7 Experiment Setup for DP CDM system (NRZ PAM).....	47
Figure 4.8 Optical spectrum of DP PAM-4 signal at transmitter end.....	48
Figure 4.9 DM PAM-4 signal: (a) constellation; (b) Measured differential phase	48
Figure 4.10 Experiment OSNR sensitivity for 40-Gb/s DP PAM-4 system.....	49
Figure 4.11 40-Gb/s DP PAM-4 transmission performance.....	50
Figure 4.12 Experiment setup for DP CDM system (Nyquist PAM)	52
Figure 4.13 Optical spectra of the two lasers with Nyquist PAM modulation.....	52
Figure 4.14 Measured probability density function of the DM PAM-4: (a) intensity and (b) differential phase	53
Figure 4.15 100 Gb/s polarization-multiplexed PAM-4 system OSNR sensitivity.....	54
Figure 4.16 100 Gb/s polarization-multiplexed PAM-4 system transmission performance.....	54
Figure 4.17 CDM system SNR sensitivity (simulation results)	55
Figure 4.18 Chirp parameters impact on the differential phase distribution.....	57
Figure 4.19 Chirp parameters impact on the SNR sensitivity of CDM systems	58
Figure 4.20 Experiment results. (a) 40-Gb/s DP PAM-4 system OSNR sensitivity. 60-Gb/s DP PAM-8 system: (b) OSNR sensitivity; (c) PAM-8 constellation after polarization demultiplexing; (d) BER versus transmission distance.....	59
Figure 5.1 Structure of a typical self-coherent transmitter	63
Figure 5.2 Transmitter structure for the optical single sideband (SSB) signal generation	65

Figure 5.3 SSBN cancellation schemes.....	66
Figure 5.4 Principle of block-wise phase switching transmitter.	66
Figure 5.5 Time-domain blocks illustration for SCI-DD	68
Figure 5.6 OSNR sensitivity for 100-Gb/s DP-SCI-DD systems	71
Figure 5.7 Experimental setup for SCI-DD transmission.....	72
Figure 5.8 Experiment results for SCI-DD transmission over 80-km SSMF.....	73
Figure 6.1 Transmitter structure for (a) POL-MUX complex modulation; (b) self-coherent Stokes-space modulation	76
Figure 6.2 Training symbols structure for SV rotation matrix	77
Figure 6.3 4-QAM constellation in (a) Jones space; (b) Stokes space. 16-QAM constellation in (c) Jones space; (d) Stokes space. (e) Surface of Eq. (6-13) in Stokes space (time-domain OFDM signal distribution)	80
Figure 6.4 Structure of the blind adaptive equalizer for SV-DD	81
Figure 6.5 Experimental setup for SV-DD	82
Figure 6.6 (a) Electrical spectra of received signals before and after the SV rotation; (b) Electrical spectra of received signal and 2nd order nonlinearity after SV rotation.....	83
Figure 6.7 System OSNR sensitivity in an 80 Gb/s SV-DD experiment.....	84
Figure 6.8 160-Gb/s SV-DD system performance	85
Figure 6.9 Experimental setup for 10-wavelength 1-Tb/s SV-DD	86
Figure 6.10 1-Tb/s SV-DD transmission performance.....	87
Figure 6.11 1-Tb/s SV-DD system OSNR sensitivity	87
Figure 6.12 Received Stokes vectors in Poincare sphere with 4-QAM modulation (a) before polarization de-multiplexing; (b) after polarization de-multiplexing; 4-QAM constellation (c) before polarization de-multiplexing; (d) after polarization de-multiplexing; (e) after channel equalization.....	89
Figure 6.13 System OSNR sensitivity comparison between the POL-DEMUX algorithms for 20-Gb/s 4-QAM SV-DD system	90
Figure 6.14 System OSNR sensitivity comparison between the POL-DEMUX algorithms for 40-Gb/s 16-QAM SV-DD system	90
Figure 6.15 PMD induced Q penalty as a function of DGD at BER level of 10^{-3}	92
Figure 6.16 OSNR sensitivity comparison among 100G SCOH systems	94
Figure 7.1 Transmitter structure for the SV-DD using (a) self-coherent complex modulation; (b) POL-MUX intensity modulation (IM); (c) X-POL complex modulation and Y-POL intensity modulation; (d) 3-D modulation in Stokes space with polar coordinates	98
Figure 7.2 Structure of frequency-domain MIMO equalizer for the POL-MUX DMT (an example of adaptive decision-directed mode)	101
Figure 7.3 Experiment setup for PDM-DMT using DD SV-R.....	102
Figure 7.4 Frequency domain MIMO equalization. (a-d) 4-QAM; (e-h) 16-QAM. (a,e) 3x1 equalizer coefficients per subcarrier; received X-POL constellation: (b,f) before MIMO; (c,g) after MIMO; (d,h) after OFDM channel equalization.....	103
Figure 7.5 Q-factor per subcarrier in the PDM-DMT experiment.....	104
Figure 8.1 OSNR requirements of the 100-Gb/s (raw data-rate) signal at 20% FEC threshold	106

LIST OF TABLES

Table I. Application categories of optical fiber transmissions	3
Table II. Comparison of transceivers proposed in this thesis	14
Table III. LDPC decoding procedures	29
Table IV. Experiments with self-coherent subsystems	93
Table V. Overcoming the DM-DD bottlenecks with the schemes in this thesis	106

1. INTRODUCTION

1.1 Optical fiber communications

Optical fiber links underpin the infrastructure of global communication networks. History of the optical fiber communications can be traced back to 1966, when K. C. Kao and G. A. Hockham, working at the Standard Telecommunication Laboratory in England, published the landmark paper [1] proposing that optical fiber has potential to become a transmission medium if its attenuation could be kept under 20 dB/km. After almost 4 years of trial and error, the breakthrough of making single mode fiber with attenuation less than 20 dB/km was achieved by scientists at Corning Glass [2], through the titanium doped silica glass. Since early 1970s, the capacity of optical fiber has made dramatic strides. Early optical communication developments focused on increasing the bit rate of single optical channel by high-speed directly modulated semiconductor lasers [3]. The early 1990s witnessed the dramatic fiber capacity increases brought by the wavelength division multiplexing (WDM) technology enabled by erbium-doped fiber amplifiers (EDFA) [4]. This evolution ignited massive investments on the deployment of optical fiber links, and the capacity of commercial optical communication systems increased from less than 100 Mb/s debuted in 1970s to 1 Tb/s by 2000 [5].

Telecommunication researchers used to believe that WDM would eventually meet the ever-increasing network traffic demand, until the early 21st century, when nearly all the available frequency bands for optical fiber were occupied. The task went back to how to increase the capacity per wavelength. The revival of optical coherent detection offers a powerful solution, which drove 10 times increase of fiber capacity since 2006 [6]. Till recently, researchers have demonstrated multi-Terabit/s optical transmission over transoceanic distance [7].

The network data demand will face at least another 10-fold growth in the next 5 years [8], mainly stimulated by the following factors:

- (1) More devices will be connected to the Internet, including not only the conventional personal computers, but also the mobile devices such as smart phone, tablet, and even wearable devices. For example, according to the Cisco whitepaper [8], “more than half a billion (563 million) mobile devices and connections were added in 2015. Global mobile devices and connections in 2015 grew to 7.9 billion, up from 7.3 billion in 2014.”
- (2) Each online device requires more data rate. For example, according to the Cisco whitepaper, “The average smartphone will generate 4.4 GB of traffic per month by 2020, nearly a fivefold increase over the 2015 average of 929 MB per month. By 2020, aggregate smartphone traffic will be 8.8 times greater than it is today.”

- (3) The cloud services generate large amounts of data exchange between personal devices and service providers. “Cloud” centralized the data and computing from the personal users to the data center, which provides easy, secure and scalable access to applications and resources with low cost and power consumption. This partition of data is not originated from the customers’ desire of Internet contents, but from the optimization perspective of the overall networks. In the future, personal devices may only have the capability of display and communication, while all the other functions are centralized to service providers.

The huge data demand requires not only the breakthrough of fiber capacity limit, but a throughout transmission capacity evolution of every layer of optical communications, namely, from 10^5 -kilometers scale transoceanic long-haul transmission, to meter-scale blade server interconnect, and even photonics-integrated on-chip communications.

The cost per bit increases with the transmission distance. When the distance increases, it is reasonable to have more advanced technologies involved in the communication system. Modern coherent transceivers gather the highest-level optical communication technologies to maximize the optical spectral efficiency per channel, by exploiting the light field through complex modulation, polarization multiplexing [9-10], and ever-advanced modulation formats [11-12]. Moreover, the coherent transmitter based on external modulation enables the sharp Nyquist pulse shaping per channel, giving rise to the superchannel [13-14] (WDM without frequency gap between the adjacent channels) transmission which push the overall spectral efficiency of all WDM channels to that of each channel. On the opposite side, direct modulation (DM) with direct detection (DD) systems own a natural attraction – the simplicity, offering the lowest hardware cost and power consumption which are critical for the cost-sensitive and power-hungry short-reach optical communications. Consequently, DM-DD is now dominant for short-reach applications, and coherent transceivers serve as the long-haul solutions. This thesis focuses on how to transform the traditional DM and DD systems by the advanced coherent technologies in order to bridge the application gap between DM-DD and coherent systems.

To reveal the application range of the schemes proposed in this thesis, Table I categories optical fiber transmissions into 4 categories by the transmission distance. These categories are defined based on the fiber channel influence instead of the absolute distance, although the Table provides approximated distance ranges for reference. It is noted that these reference distances have a close relationship with the signal baud-rate per channel, because higher baud-rate signal always suffers from severer channel impairment under the same transmission distance. In Table I the signal baud-rate is assumed around tens of Gbaud. Cat. I ignores any fiber channel impairment, and therefore the transceiver expense is the dominant consideration for system design. As a counterpart, in terms of Cat. IV, the fiber installation is much more expensive than the

transceiver, and generally the transceiver should utilize the most advanced hardware and signal processing to realize the best fiber transmission performance. Between Cat. I and IV, there exist a trade-off between the transceiver expense and system transmission performance. Throughout the thesis, we term the “short reach” as the transmission categories I, II and III, where the transceiver could be simplified (with reference to the modern coherent transceiver for Cat. IV) to meet the cost-effective feature of optical short-reach applications.

Table I. Application categories of optical fiber transmissions

Category	Definition	Application examples	Reference distance
I	Little channel impact	Mobile fronthaul	0 – 100 m (multimode fiber)
		Fiber to the x (FTTx) Inside data center	0 – 10 km (single-mode fiber)
II	Fiber dispersion becomes a major channel impairment	Passive optical network (PON)	10 – 80 km (single-span amplification)
		Data center interconnect	
III	Beyond Cat. II, optical amplification noise becomes a major channel impairment (due to multiple spans)	Metropolitan area network (MAN)	80 – 1000 (multi-span amplification)
		Inter-city links	
IV	Beyond Cat. III	Submarine links	>1000

1.2 Digital coherent detection

Optical coherent detection was first proposed and experimentally demonstrated in 1980 [15]. Applying a local oscillator (LO) at receiver as reference, coherent detection can recover the full information of the optical field, including the intensity, phase, and even polarization states. This enables various modulation formats for coherent system, such as the phase shift keying (PSK), frequency shift keying (FSK), and quadrature amplitude modulation (QAM). However, coherent detection is not preferred at its early era, because the coherent system is much complicated compared with the direct detection system. LO brings many problems to the receiver, such as the frequency stabilization, phase noise compensation and polarization alignment. Moreover, the invention of EDFA [4] in early 1990s improves the pre-amplified receiver sensitivity of direct detection that

matches those of coherent detection. The widespread application of EDFAs also made researchers believe that the available optical bandwidth resources could be endless, and there is no need to further increase the capacity per wavelength channel via coherent detection.

In early 21st century, there emerged a crucial bottleneck of the network capacity – the available optical bandwidth was being quickly exhausted. It became urgent to upgrade the channel capacity per wavelength. The revival of coherent optical systems successfully made a breakthrough within the last decade. Instead of intensity-only modulation, coherent systems map the baseband signal to optical field, and thus enables the multi-dimension modulation. This revival owes not only to the development at optical device level, but, more importantly, to the powerful digital signal processing (DSP) technologies concatenated after the coherent receiver. DSP enables a variety of compensation methods for transmission impairments:

- (1) Chromatic dispersion. CD is a linear channel impairment to the optical field. In DD subsystem, the square-law intensity detection converts this linear impairment to a nonlinear impact. Before the revival of digital coherent detection, early signal processing tried the nonlinear equalizer, such as the maximum likelihood sequence estimation (MLSE) [16] to alleviate the CD induced inter-symbol interference (ISI). However, this indirect approach can never achieve the optimum performance, and the nonlinear equalization usually has high computational complexity. Coherent detection recovers the optical field, offering a straightforward way to linearly compensate the CD. For example, the most popular CD post-compensation is performed by the digital finite impulse response (FIR) filter [17]; alternatively, CD equalizer can also be realized in frequency domain [18]. For OFDM modulation, CD can be tolerated by the cyclic prefix [10], without any extra DSP consumption. CD is no longer a barrier of transmission distance.
- (2) MIMO channel equalization. Polarization state changes randomly during fiber transmission. The polarization recovery used to be accommodated by the optical polarization tracker [19-20], which outputs a fixed polarization state regardless of the incoming state. However, this optical device is bulky, expensive, and most importantly, limited by the polarization variation speed. Coherent detection sheds light on this classic issue by recovering the digital signal in the Jones space, where a 2×2 Jones matrix characterizes the polarization state. As a time-variant effect, polarization tracking should be performed by the adaptive MIMO equalization. This is normally realized by the adaptive equalizers under the steepest descent criteria, such as the least mean square (LMS) filter and the constant-modulus algorithm (CMA) [17]. Alternatively, the adaptive equalization can also be realized by sending training sequences periodically and performing 1-tap equalization in frequency domain. Optical OFDM systems usually adopt this method [10]. By digital

polarization recovery, polarization multiplexing now has become the standard modulation approach to double the optical spectral efficiency per WDM channel.

- (3) Polarization mode dispersion (PMD) and polarization dependent loss (PDL). These polarization impairments are frequency dependent. Using coherent detection, the most straightforward way to compensate PMD and PDL is to estimate the 2×2 Jones matrix across the frequency, and then perform the 2×2 channel equalization. The process is naturally supported by the OFDM frequency domain equalization [21], and can be easily implemented by the FIR equalizers in time domain [22].
- (4) Carrier phase noise. As coherent detection recovers the optical phase, the received signal is sensitive to the laser phase noise. At early stage of coherent technology, carrier recovery was fulfilled by the optical phase-locked loop (OPLL) [23]. However, the linewidth tolerance was low, and thus not suitable for modern high baud-rate transmission. DSP offers simple and fast phase noise estimation, which offers tens of times tolerance of linewidth – baud-rate product. The most popular approach nowadays in coherent system is the feedforward carrier recovery [24-25].
- (5) Fiber nonlinearity. Fiber channel capacity is restricted by the nonlinear Shannon limit [26]. Fiber nonlinearity can be partially alleviated by DSP [27-29].

The modern coherent detection cannot live without DSP. In this sense, this state-of-the-art technology is normally named digital coherent detection. This thesis will extensively investigate how the advanced digital coherent technology can be applied to the short reach applications to significantly improve the system performance.

1.3 State-of-the-art DM-DD short-reach applications

The primary attraction of DM is the simplicity. With the laser biased above threshold and a baseband modulation superimposed on the drive current, the laser output intensity is an analog of the baseband signal [3]. Traditional DM is performed without phase control, and a single-ended photodiode is sufficient to retrieve the intensity modulation (IM) information by DD ignoring any fiber channel impact. Taking into account a very-short-reach fiber transmission, DM can work on the 850-nm wavelength window with multimode fiber (normally <100 m) to realize the lowest link cost, or on the 1310-nm window with single-mode fiber (<40 km) to elongate the distance. The most widely applied baseband modulation in commercial interconnect product is the non-return-to-zero (NRZ) on-off-keying (OOK). Typically, this does not require the digital-to-analog converter (DAC) or analog-to-digital converter (ADC) inside the transceiver, and thus, no digital signal processing (DSP) is involved in DM-DD system. Towards 100G Ethernet, DM-DD can deliver 100 Gb/s data via 10-channel 10-Gb/s or 4-

channel 25-Gb/s systems, using coarse WDM (CWDM), or even parallel fiber bundles, according to the IEEE 802.3ba task force [30].

To upgrade the Ethernet interface to 400GbE or even beyond, the most straightforward way is to enhance the modulation bandwidth of the DM lasers (DML). Recent advances on a variety types of DMLs have pushed their bandwidth approaching or even exceeding that of the external modulators applied in coherent systems. For example, an 850-nm vertical-cavity surface-emitting lasers (VCSEL) realizes bandwidth beyond 30 GHz in [31]; a 1310-nm distributed feedback (DFB) laser achieves 30-GHz bandwidth in [32]; a most recent report on the 1300-nm distributed reflector laser shows a DM bandwidth up to 55 GHz [33]. There even emerges DMLs designed at 1550-nm window with bandwidth beyond 25 GHz [34], which are suitable for transmission applications beyond 80 km. It is noted that some optical IM transmitters exploits external modulation (EM) such as the electro-absorption modulator (EAM) and the Mach-Zehnder modulator (MZM) instead of DM. By photonics integration, these EM devices also realize high modulation bandwidth with low cost. For example, a silicon photonics (SiP) MZM realizes bandwidth beyond 20 GHz in [35]; an indium phosphide (InP) monolithic DFB laser and MZM achieve 44-GHz bandwidth in [36]; an integrated DFB-EAM module even shows 60-GHz bandwidth in [37].

High bit-rate per DM-DD channel requires higher baud-rate baseband signal and higher-order modulation beyond OOK such as PAM-4. This reinforces the detrimental influence combined between DM chirp and fiber dispersion [38-39], even for a very-short distance. Equalizations become essential to mitigate the fiber channel impact, as well as the distortions from the high-speed transceiver itself. Without DSP, the equalization can be realized by analog electronic or optical filters. The advantage of the electronic equalization is that the filters need not to concern the laser wavelength drift. However, it can only compensate the laser modulation distortion, but not the frequency chirp. One example of electronic equalization in [40] uses electrical tapped-delay-line and RF filter before the baseband signal is launch into the bias-T of the DML. The optical equalization inserts a filter after the DML to shape the optical spectrum, and thus requires the wavelength alignment between DML and filter. The most famous optical equalization concept is the chirp-managed DML (CML) [41], which limits the chirp-expanded optical spectrum and enhances the OOK extinction ratio by FM-AM conversion, and thus increases the dispersion tolerance. Some extensions of this idea have been demonstrated recently by realizing the filtering effect with other optical devices, such as the optical delay interferometer [42] and the optical dispersion compensation (ODC) module [43] (the ODC here is not applied for fiber dispersion compensation, but rather provides a negative dispersion to compress the pulse width of DM signals). A more radical method of further increasing the signal baud-rate exceeding the DML modulation bandwidth the duobinary pulse-shaping [44] of NRZ signal. Here,

the purpose of duobinary is to break the band-limitation of the E/O and O/E conversions in DM-DD transceivers [45-46]. In retrospect, another purpose of duobinary shaping is to reduce the signal bandwidth for better dispersion tolerance, and thus, longer transmission distance [47]. Combining both purposes, duobinary currently is a very promising candidate for the passive optical networks (PON) applications.

DSP is normally prohibited in DM-DD commercial short-reach products due to its high complexity and power consumption. However, recent years have witnessed the trend of DSP being applied to DM-DD systems, especially for high baud-rate high-order modulation, to compensate the transceiver imperfection. Moreover, for extend-reach beyond 10 km, DSP becomes acceptable in DM-DD systems, because the combination of DM-DD and DSP is still much cheaper than the coherent solutions within this application range. The most popular digital equalization technique is the linear equalizers like feed-forward equalizer (FFE) and decision-feedback equalizer (DFE). Linear equalizers can be applied either at transmitter for pre-distortion, or at receiver for channel equalization. Experiments have demonstrated effective improvement to remove the end-to-end linear distortion of the intensity transceiver [48-50]. In DM-DD system, nonlinearity may arise from the E/O and O/E conversion, or the link dispersion. Following the similar idea of “weighted superposition of signals” in linear equalization, a popular nonlinear equalizer is the Volterra filter [50-52], which not only contains the weighted superposition of linear terms (such as S_t, S_{t-1}, \dots), but also weighted superposition of nonlinear terms (such as $S_t^2, S_t S_{t-1}, S_{t-1}^2, \dots$). The most powerful nonlinear equalizer is the MLSE [53]. Instead of calculating the tap weights, MLSE determines the maximum likelihood symbol chain (the survivor path) by estimating the probability of every possible path on the trellis graph. However, the complexity increases exponentially with the channel memory.

In retrospect of the fiber channel with extended-reach, dispersion becomes the dominant system impairment for point-to-point DM-DD systems. Although dispersion is a linear distortion to optical field, it becomes a nonlinear distortion in terms of optical intensity. Nonlinear filters can be applied to alleviate the dispersion impact [16], but never eliminate it. A straightforward way of handling large dispersion while maintaining the intensity-only DD is the dispersion compensation. In terms of the electrical pre-compensation, the transmitter is required to control the optical phase for dispersion pre-compensation [54-55], which normally needs a field modulator such as the nested-MZM I/Q modulator. This becomes much more expensive than the DMLs. Alternatively, there may exist a window of opportunity for the revival of ODC technologies [56-58]. ODC is complicated for multi-span long-haul transmission; but in terms of single-span short-reach link, a single ODC module can be shared by multiple WDM channels, which solves the dispersion issue without individual digital equalization for each channel.

A bonus of DSP in DM-DD systems is that it enables advanced modulation formats beyond OOK and PAM. For example, a sharp Nyquist-pulse shaping at transmitter can double the signal baud-rate compared with the NRZ pulses, using the DML with identical bandwidth; the discrete multitone (DMT) [59] and multiband carrier-less amplitude phase (CAP) [60] modulation can be applied to adapt the fading channel frequency response induced by the dispersion which maximizes the link bit-rate. With the cost and power reduction of DSP in the near future, high-baud rate DM-DD with DSP will become the powerful combination for 400GbE or even Terabit Ethernet interface

1.4 Bottlenecks of DM-DD short reach optical applications

DM-DD dominates the commercial short reach applications as discussed in the above section. When upgrading its data rate per channel beyond 100 Gb/s and its distance beyond 100 km, DM-DD faces several fundamental barriers. This section summarizes these bottlenecks which prevent the further enhancement of distance – bit-rate product in DM-DD systems.

A. 1-dimension modulation

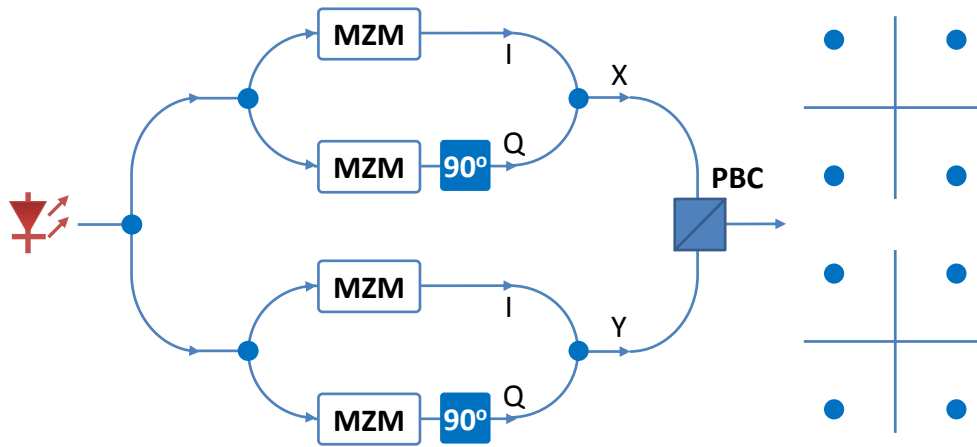


Figure 1.1 4-D optical field transmitter. MZM: Mach-Zehnder modulator; 90°: 90-degree phase delay; PBC: polarization beam combiner.

The light transmitted through a single mode fiber has 3 degrees of freedom: intensity, phase, and polarization. This can be expressed as Jones vector,

$$J = \begin{bmatrix} A_x e^{i\delta_x} \\ A_y e^{i\delta_y} \end{bmatrix} \quad (1-1)$$

where A stands for the amplitude of each polarization, δ stands for the phase, and x/y stands for the two polarizations. Obviously, the optical field in Eq. (1-1) has 4 dimensions.

This 4-D field signal can be generated by 4 optical intensity modulators, such as the Mach-Zehnder modulator (MZM) driven at null point, shown by Figure 1.1. However, DM-DD only performs 1-D modulation and detection, which significantly limit its spectral efficiency, namely, the achievable data rate given a fixed bandwidth.

B. Chromatic dispersion

The optical fiber is dispersive, namely, the group velocity of the light wave depends on its frequency. Different frequency components of the optical pulse transmit through the fiber with various speeds, leading to the pulse spreading in time domain. This phenomenon is named group velocity dispersion (GVD), and can be characterized by the parameter D :

$$D = \frac{1}{L} \frac{dT}{d\lambda} \quad (1-2)$$

where T is the transmission time of an optical pulse with the fiber distance of L , and λ is the wavelength. Physically, D is the measure of pulse spreading (unit: second) per unit bandwidth per unit length of the transmission medium. The pulse spreading of a fiber link can be estimated as:

$$\Delta t = DL\Delta\lambda \quad (1-3)$$

where $\Delta\lambda$ is the bandwidth of the optical signal.

Conventional DM-DD system uses low speed on-off-keying (OOK) modulation, which sends optical pulse as 1. Thus, pulse spreading in time domain, expressed as Eq. (1-3), is the main concern of the system. High speed DM-DD requires large signal bandwidth with advanced modulation format. In this case, it is more straightforward to investigate the CD impact in frequency domain. To reveal the channel frequency response of DM-DD, we use a wide band real-value OFDM signal $s(t)$ at baseband, which has a quasi-discrete spectrum. It is noted that the DM discussion in this sub-section has ignored the frequency chirp for simplicity, and DM is regarded as pure intensity modulation (IM).

$$s(t) = \sum_{-1/2.N+1}^{1/2.N} c_k e^{j2\pi f_k t} \quad (1-4)$$

where N is the OFDM subcarrier number, c_k is the symbol for the k -th subcarrier, f_k is the frequency of the k -th subcarrier. To force the time-domain $s(t)$ as real value, the symbols have to satisfy the condition,

$$c_{-k} = c_k^* \quad (1-5)$$

namely, the spectrum is conjugate symmetric (*' is the conjugate operation).

After the fiber transmission with CD, the signal at baseband frequency f experiences the phase delay:

$$\Phi_D(f) = \frac{\pi\lambda^2 DL}{c} f^2 \quad (1-6)$$

where λ is the carrier wavelength, D is the accumulated CD in the unit of ps/pm , L is the fiber length and c is the speed of light. Since the baseband spectrum is conjugate symmetric, we consider the frequency pair f_k and $-f_k$ in Eq. (1-4). Assuming the symbol at f_k is c_k , the symbol at $-f_k$ should be its conjugate c_k^* . Therefore, the signal pair is:

$$s_{f_k}(t) = c_k e^{j[2\pi f_k t + \Phi_D(f_k)]} \quad (1-7)$$

$$s_{-f_k}(t) = c_{-k} e^{j[-2\pi f_k t + \Phi_D(-f_k)]} = c_k^* e^{-j[2\pi f_k t - \Phi_D(f_k)]} \quad (1-8)$$

When using coherent detection, the receiver recovers a linear replica of the conjugate symmetric baseband spectrum. However, in DD receiver, this pair of signals interferes with each other after the square-law detection. When the phase sum of this pair is the odd multiple of π at frequency f_d , the spectrum suffers the destructive interference at f_d . We deduce the destructive frequency as:

$$f_d = \sqrt{\frac{2n+1}{2}} \cdot \sqrt{\frac{c}{\lambda^2 DL}} \quad n = 0, 1, 2, \dots \quad (1-9)$$

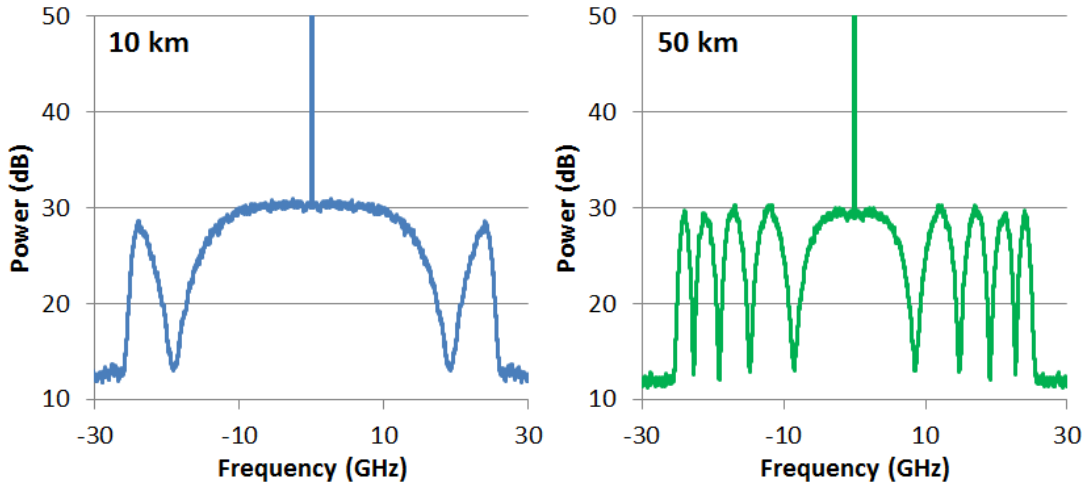


Figure 1.2 Electrical spectra of IM-DD signal after fiber transmission under chromatic dispersion.

Considering an OFDM signal with many subcarriers where the frequency resolution is extremely high, the above analysis can be extended to the single-carrier modulation, which has a continuous spectrum. We send a 50-Gbaud Nyquist pulse shaped PAM-4 signal at 1550-nm and transmit it over different fiber length with the CD of 17-ps/nm/km, and simulate the received spectra. As seen from the Figure 1.2, the power notches of the spectra coincide well with the Eq. (1-9). When the distance increases, the frequency of first notch decreases, and the total number of notch within 50 GHz increases dramatically (Figure 1.3).

The fading channel response resulting in an irreversible loss of information at the destructive frequency. When the product of signal baud-rate and transmission distance

is large [61-62] (e.g. >1000 Gbaud·km), this fading becomes a severe impairment of the DM-DD system.

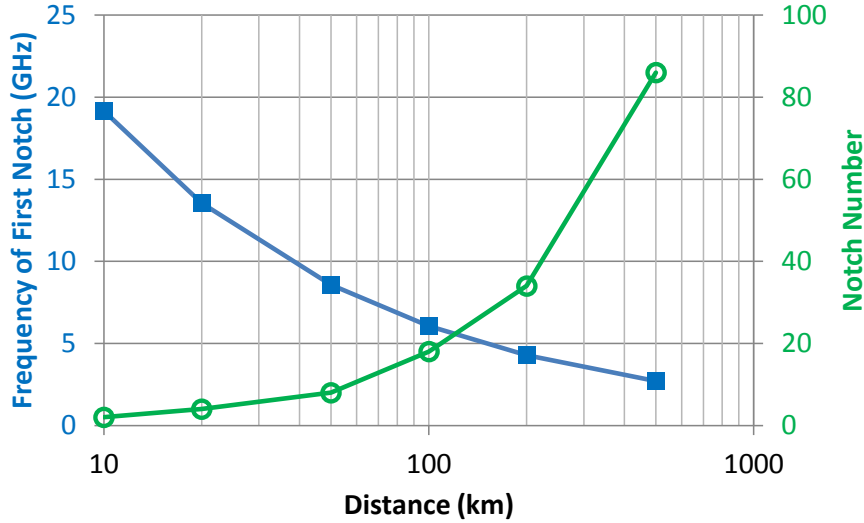


Figure 1.3 Power fading notch characteristics at difference fiber distance. Primary axis (blue): frequency of the first notch; secondary axis (green): the total notch number within 50-Gbaud.

C. Frequency chirp

A semiconductor laser can be directly modulated via the drive current. The current changes the carrier density inside the semiconductor medium, leading to the refractive index (RI) variation of the medium. The RI variation results in a frequency drift of the output light. This intensity modulation induced frequency modulation is normally named as frequency chirp [3,38-39]. The laser diode rate equation provides the relationship between the photon and carrier density. Derived from rate equation, the frequency chirp can be expressed directly by the laser output power $P(t)$ [3]

$$\Delta f = \frac{\alpha}{4\pi} \left(\frac{d}{dt} \ln P(t) + \kappa \cdot P(t) \right) \quad (1-10)$$

where α is the transient chirp coefficient (also named as phase-amplitude coupling coefficient or linewidth enhancement factor [63]), and κ is the adiabatic chirp coefficient.

During the laser direct modulation, the frequency chirp induces a frequency modulation simultaneously with the desired intensity modulation. The most straightforward impairment of chirp is the spectrum expansion. The signal bandwidth signal would be severely broadened after the optical direct modulation, leading to a much wider optical spectrum compared with the baseband electrical spectrum. As discussed in Section 1.3.B, signal with wider bandwidth would no doubt suffer from more severe frequency selective fading under the chromatic dispersion. Together with CD, the chirp significantly limits the transmission performance of a direct modulation system.

1.5 Thesis contributions

The long-haul coherent technology has successfully overcome the above performance barriers by the high-end optical hardware and powerful DSP. However, for cost-sensitive short reach applications, it is challenging to bridge the coherent technologies to the conventional DM-DD by cost-efficient solutions. This thesis aims to bring the coherent technology gradually to ever shorter reach optical transmission. Figure 1.4 shows the thesis contributions categorised by the transmission distance. From Chapter 3 all the way to Chapter 7, the thesis presents its trend of progressively reforming the standard coherent transceiver to simpler architectures suitable for shorter-distance applications.

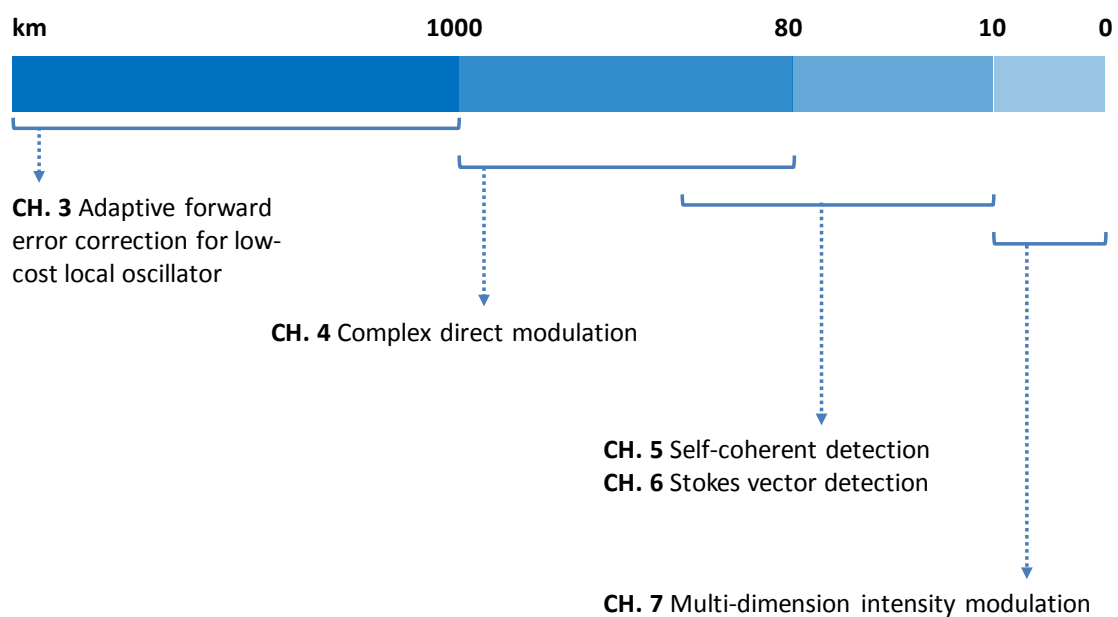


Figure 1.4 Thesis contributions categorised by the transmission distance.

The primary consideration of the system simplification is the optical hardware. With the development of photonics integration circuits (PIC) technology, the expense of passive optical components has potential to decrease significantly in the near future. The major expense derives from the active devices, especially the lasers and optical amplifiers.

Chapter 3 begins the reforming from a typical coherent technology designed for long-haul transmission, the coherent optical OFDM (CO-OFDM) system. To lower the receiver expense, a low-cost laser is utilized as the local oscillator for coherent detection. This induces much severe near-DC noise, which degrades the Q-factor of the subcarriers whose frequency is close to that of the local oscillator. An adaptive forward error correction (FEC) encoding is applied to handle the burst error near the local oscillator, and the channel SNR information is applied to the FEC soft decoding to further improve the decoding gain. This shed light on the path of using advanced DSP to compensate the imperfect optical hardware.

A further cost-down approach for the lasers in coherent systems is to employ the semiconductor lasers at both transmitter and receiver. Especially, semiconductor laser

can be directly modulated, which avoids the sophisticated external modulation. Directly-modulated semiconductor lasers (DML) are normally 2 or even 3 orders cheaper than the nested I/Q modulator. Chapter 4 proposes the system combination of DML and coherent detection for metro distance of around 1000 km, where chromatic dispersion is the dominant fiber channel impairment. Although coherent detection can digitally compensate the dispersion, DM is generally not regarded as a suitable modulation for multi-span fiber transmission, because it only modulates the intensity-only 1-D signal, which strongly limits its achievable system OSNR sensitivity compared with the 2-D external-modulated I/Q signal. Nevertheless, Chapter 4 exploits the digital coherent detection to convert the “detrimental” DML frequency chirp into a system benefit. The chirp offers the phase dimension for modulation, which converts the 1-D DM to a 2-D complex modulation format, and significantly increase the OSNR sensitivity for DM coherent system.

DD without the local oscillator offers an even simpler transceiver structure. Compared with coherent detection, DD owns the following advantages for short-reach application. (i) No receiver-side laser further decrease the expense; especially, it may be crucial to have a low-cost receiver without lasers for optical access applications, where the end-user is extremely cost-sensitive. (ii) The transmitter laser can be uncooled (namely, without the temperature control), because there is no need to align the wavelength between the transmitter and receiver. (iii) DD has larger linewidth tolerance for transmitter laser, while the carrier phase recovery is normally avoidable at receiver. (iv) DD is compatible with single polarization configuration, where the MIMO polarization demultiplexing is not an essential task at receiver. Although the conventional intensity-only DD cannot digitally compensate the dispersion, it can be realized by the DD self-coherent subsystems. Chapter 5 and 6 propose a variety of self-coherent subsystems, including the single-polarization schemes in Chapter 5 and polarization-diversity scheme in Stokes space in Chapter 6. Self-coherent subsystems send the signal along with a constant carrier at transmitter, so that the direct-detection receiver can still detect the signal with the reference, namely, the capability of recovering the optical field. This offers self-coherent subsystems the capability of digital dispersion compensation, which enables DD as the suitable receiver for transmission Cat. II and III in Table I. However, DD has natural system OSNR penalty compared with coherent detection, which limits its achievable optical amplification spans. Therefore, self-coherent subsystems is illustrated as the suitable solution for single or a-few span transmission applications in Figure 1.4.

At very-short-reach range below 10 km, DM-DD is no doubt the dominant interconnect technology. However, as pointed out previously, DM-DD faces the bottleneck of single dimension modulation. When the CWDM channel is exhausted, it is inevitable to exploit the polarization diversity to increase the spectral efficiency per channel. Chapter 7

realizes the multi-dimension intensity modulation by polarization modulation in Stokes space. Although it only detects the optical intensity (namely, the direct detection) along orthogonal polarizations, the Stokes vector receiver needs the polarization coherence for the MIMO in Stokes space. The coherent concept presents its potentials even at such short transmission distance. It is noted that the multi-dimension IM-DD is no longer a coherent system because it cannot recover the signal field (due to the lack of optical reference). Dispersion cannot be compensated, and thus the transmission is limited to Cat. I in Table I.

The gradual transceiver simplification described above is summarized below in Table II to better reveal the thesis contributions.

Table II. Comparison of transceivers proposed in this thesis

	Scheme	Transmitter	Receiver	Key DSP
CH. 3	Coherent systems	Narrow-linewidth laser 2 I/Q modulators	Wide frequency drift laser 2-POL coherent receiver	Dispersion compensation MIMO equalization Carrier phase recovery
CH. 4	Complex direct modulation	2 DMLs	Wide-linewidth laser 2-POL coherent receiver	Dispersion compensation MIMO equalization MLSE
CH. 5	Self-coherent detection	Wide-linewidth laser 1 I/Q modulator	Single photodiode / 1-POL coherent receiver (without laser)	Dispersion compensation Channel equalization
CH. 6	Stokes vector detection	Wide-linewidth laser 1 I/Q modulator	Stokes vector receiver	Dispersion compensation MIMO equalization
CH. 7	Multi-dimension IM-DD	2 DMLs	Stokes vector receiver	MIMO equalization

Optical amplifier (OA) is another crucial active device in optical transmission systems. Whether to use OA or not depend on the target transmission distance. In general, transmission Cat. I in Table I does not require OA because the link distance is short and induce little fiber loss. Cat. II may require one OA in the link for either pre-amplification at transmitter or post-amplification at receiver. Recent research also attempts to utilize the high power DML to avoid OA for Cat. II [64], aimed at minimizing the total system noise. Cat. III and IV no doubt require multi-span amplification. Without OAs in the fiber link, the dominant system noise source is the receiver noise (mainly derived from the photodiode). The link performance of this type of system is characterized by the receiver sensitivity (for example, the BER versus received optical power). Optical access network is hungry for optical power budget. Without OA to amplify the optical power, it normally requires high sensitivity photo-detection, for example, the widely-deployed avalanche photodiode (APD) for Cat. I. It is beyond the scope of this thesis to achieve high receiver sensitivity from the hardware (photodiodes) perspective.

For optical transmission (beyond Cat. I) with OAs in the fiber link, optical amplified spontaneous emission (ASE) noise is the dominant noise source. The transmission performance of this type of system is characterized by the system OSNR sensitivity, for instance, the link OSNR requirement for a target BER (normally a FEC threshold). As the coherent systems recover the optical field which enables the digital dispersion compensation, most subsystems proposed in this thesis (from CH. 3 to 6) are designed for transmission beyond Cat. II, where OAs are essential for the fiber link. Therefore, the system OSNR sensitivity is the criterion to evaluate these subsystems no matter for simulation or experiment. The multi-dimension polarization modulation in CH. 7 is an exception, which is designed for transmission Cat. I (or Cat. II if optical dispersion compensation is utilized). The receiver sensitivity analysis is beyond the scope of this thesis, but the (receiver noise dominant) channel capacity for the multi-dimension polarization modulation has been derived in Ref. [65].

The coherent solutions for short-reach applications are certainly not confined to the contents exploited in this thesis. Nevertheless, this thesis aims to shed light on the cost-efficient coherent solutions, to accelerate the evolution of coherent technology to ever-shorter applications.

1.6 Thesis outline

The thesis is organized as follows:

Chapter 1. Introduction. This chapter introduces the fundamental performance barriers for the conventional DM-DD systems that is dominant in the commercial optical short reach applications.

Chapter 2. Optical detection methods. This chapter introduces the optical detection subsystems including both the direct detection and coherent detection. The receiver detection dimension determines the maximum achievable modulation dimension at transmitter. The detection methods cover from the 1-D intensity detection to the 4-D (complex signal with polarization multiplexing) full optical field detection.

Chapter 3. Subcarrier reliability aware LDPC for CO-OFDM. This chapter uses the advance forward error correction (FEC) scheme to relax the wavelength drift restriction of the local oscillator in coherent detection. FEC has been widely applied to optical communication systems. The chapter briefly explains the encoding scheme of the most widely used FEC – linear block codes. The decoding of linear block codes can be categorised to two groups: hard decision and soft decision. Soft decision requires more complicated computation, but it makes full use of the information in the signal constellation, thus provides much larger coding gain. Based on soft decision, we propose the subcarrier reliability aware low density parity check codes for the multicarrier optical coherent system, by utilizing the subcarriers SNR information. The coding scheme is verified by a 100G coherent optical OFDM experiment.

Chapter 4. Frequency chirp enabled complex modulation. This chapter introduces how to convert the detrimental frequency chirp to a system benefit with the assistance of coherent detection. The chapter first explains the complex modulation model of the semiconductor lasers; and then proposes the modified maximum likelihood sequence estimation to demodulate the signal jointly by the optical intensity and differential phase. Compared with the conventional intensity modulated PAM-4 system, complex modulated PAM-4 system presents more than 10-dB system OSNR sensitivity. Owing to such a large advantage, we experimentally demonstrate the first beyond 1000-km SSMF transmission using dual polarization PAM-4 signal. More surprisingly, we point out that high-order PAM requires even larger chirp to support a better complex modulation performance. We experimentally demonstrate the first dual-polarization PAM-8 signal over 320-km SSMF.

Chapter 5. Optical self-coherent subsystems. This chapter introduces how to linearize the optical direct detection channels using self-coherent subsystems. The chapter first investigates the key technologies involved in self-coherent subsystems, and then discusses a variety of novel direct detection schemes, such as the block-wise phase switching direct detection, and the signal carrier interleave (SCI) direct detection. We experimentally demonstrate the first single channel single polarization 100-Gb/s direct detection reception using SCI scheme. As a by-product of dual polarization SCI system, we propose a novel communication channel model named discrete-time Gaussian channel with conjugate intersymbol interference. We briefly study its channel characteristics, and propose the maximum likelihood sequence estimation for the demodulation of the signal going through such a channel.

Chapter 6. Stokes vector detection subsystems. This chapter begins by introducing the Stokes vector detection subsystems. The principle of Stokes vector detection contains 3 parts: (i) the receiver structures in Section 2.3; (ii) the Stokes space modulation formats in Section 6.1 and 7.1; (iii) polarization demultiplexing in Stokes space in Section 6.2, 7.2 and 7.3. This chapter focuses only on the Stokes vector direct detection with the self-coherent configuration. By assigning the signal and reference carrier to the 2 orthogonal polarizations, Stokes vector receiver realizes the self-coherent detection by polarization diversity, and for the first time realizes the optical direct detection with 100% spectral efficiency referred to the single polarization coherent detection. Section 6.3 offers a thorough comparison among various self-coherent subsystems. Section 6.4 describes some high bit-rate Stokes vector detection experiments, such as the single wavelength 160 Gb/s in section 6.4.A, and 10 wavelengths 1 Tb/s in section 6.4.B.

Chapter 7. Multi-dimension polarization modulation. This chapter introduces the application of Stokes vector detection to the multi-dimension polarization modulation. Short after the first demonstration of self-coherent Stokes vector system, researchers found out that the Stokes vector detection can be a powerful tool to double or even triple the IM-DD system bit rate. Section 7.1 generalizes the Stokes-space modulation to any 2-D or 3-D formats modulated in Stokes space. Section 7.2 revisits the polarization demultiplexing in section 6.2, and generalizes the channel in Stokes space as 3×3 MIMO model, so that the common MIMO equalizations can be applied to the Stokes vector detection systems. Section 7.3 further generalizes the 3×3 MIMO to frequency domain to fit for the OFDM modulation in Stokes space, verified by the polarization multiplexed discrete multitone experiment in section 7.4.

Chapter 8. Summary. This chapter summarizes the thesis.

1.7 Author's publications related to this thesis

- [1] **Di Che**, Feng Yuan, and William Shieh, "Towards high-order modulation using complex modulation of semiconductor lasers," *Optics Express* 24(6), 6644-6649, 2016.
- [2] **Di Che**, Feng Yuan, Hamid Khodakarami, and William Shieh, "Duobinary pulse shaping for frequency chirp enabled complex modulation," *Optics Letters* 41(17), 3968-3971, 2016.
- [3] Feng Yuan, **Di Che**, and William Shieh, "Receiver Bandwidth Effects on Complex Modulation and Detection Using Directly Modulated Lasers," *Optics Letters* 41(9), 2041-2044, 2016.
- [4] **(Invited)** William Shieh, Hamid Khodakarami, and **Di Che**, "Polarization diversity and modulation for high-speed optical communications," *APL Photonics* 1, 040801, 2016.
- [5] **(Invited)** **Di Che**, Feng Yuan, Qian Hu, and William Shieh, "Frequency chirp supported complex modulation of directly modulated lasers," *Journal of Lightwave Technology* 34(8), 1831-1836, 2016.
- [6] **(Invited)** **Di Che**, Qian Hu, and William Shieh, "Linearization of Direct Detection Optical Channels using Self-coherent Subsystems," *Journal of Lightwave Technology* 34(2), 516-524, 2016.

- [7] **(Invited) Di Che**, and William Shieh, “Polarization demultiplexing for Stokes vector direct detection,” *Journal of Lightwave Technology* 34(2), 754-760, 2016.
- [8] Qian Hu, **Di Che**, Yifei Wang, Feng Yuan, Qi Yang, and William Shieh, “Complex modulation and detection with directly modulated lasers,” *Optics Express* 23(25), 32809-32819, 2015.
- [9] **Di Che**, Qian Hu, Feng Yuan, Qi Yang, and William Shieh, “Enabling Complex Modulation of Directly Modulated Signals Using Laser Frequency Chirp,” *IEEE Photonics Technology Letters* 27(22), 2407-2410, 2015.
- [10] **(Invited) Di Che**, An Li, Xi Chen, Qian Hu, Yifei Wang, and William Shieh, “Stokes Vector Direct Detection for Linear Complex Optical Channels”, *Journal of Lightwave Technology* 33(3), 678-684, 2015.
- [11] Qian Hu, **Di Che**, Yifei Wang, An Li, Jian Fang, and William Shieh, “Beyond amplitude-only detection for digital coherent system using directly modulated laser,” *Optics Letters* 40(12), 2762-2765, 2015.
- [12] **(Invited) Qian Hu, Di Che**, Yifei Wang, and William Shieh, “Advanced modulation formats for high-performance short-reach optical interconnects,” *Optics Express* 23(3), 3245-3259, 2015.
- [13] Xi Chen, Jiayuan He, **Di Che**, and William Shieh, “Hybrid Modulated Multiband Coherent Optical OFDM for Low-Complexity Phase Noise Compensation”, *Journal of Lightwave Technology* 33(1), 126-132, 2015.
- [14] **Di Che**, An Li, Xi Chen, Qian Hu, Yifei Wang and William Shieh, “Stokes vector direct detection for short reach optical communication,” *Optics Letters* 39(11), 3110-3113, 2014.
- [15] An Li, **Di Che**, Xi Chen and William Shieh, “Spectrally efficient optical transmission based on Stokes vector direct detection,” *Optics express* 22(13), 15662-15667, 2014.
- [16] **Di Che**, Hamid Khodakarami, An Li, Xi Chen, Trevor Anderson and William Shieh, “Subcarrier reliability aware soft-decision LDPC code in CO-OFDM systems,” *IEEE Photonics Technology Letters* 26(11), 1157-1160, 2014.
- [17] Xi Chen, An Li, Qian Hu, Jiayuan He, **Di Che**, Yifei Wang and William Shieh, “Demonstration of direct detected optical OFDM signals via block-wise phase switching,” *Journal of Lightwave Technology* 32(4), 722-728, 2014.
- [18] Xi Chen, **Di Che**, An Li, Jiayuan He and William Shieh, “Signal-carrier interleaved optical OFDM for direct detection optical communication,” *Optics express* 21(26), 32501-32507, 2013.
- [19] An Li, **Di Che**, Xi Chen, Qian Hu, Yifei Wang and William Shieh, “61 Gbits/s direct-detection optical OFDM based on blockwise signal phase switching with signal-to-signal beat noise cancellation,” *Optics letters* 38(14), 2614-2616, 2013.
- [20] Xi Chen, An Li, **Di Che**, Qian Hu, Yifei Wang, Jiayuan He and William Shieh, “Block-wise phase switching for double-sideband direct detected optical OFDM signals,” *Optics express* 21(11), 13436-13441, 2013.
- [21] **Di Che**, Feng Yuan, and William Shieh, “100-Gb/s Complex Direct Modulation over 1600-km SSMF Using Probabilistic Transition Estimation,” *Optical Fiber Communication Conference*, Los Angeles, CA, paper M3C.5, 2017.
- [22] **Di Che**, Feng Yuan, and William Shieh, “200-Gb/s Polarization-Multiplexed DMT using Stokes Vector Receiver with Frequency-Domain MIMO,” *Optical Fiber Communication Conference*, Los Angeles, CA, paper Tu3D.4, 2017.

- [23] **Di Che**, Feng Yuan, and William Shieh, “*Adiabatic Chirp Impact on the OSNR Sensitivity of Complex Direct Modulation: An Experiment Investigation*,” Optical Fiber Communication Conference, Los Angeles, CA, paper Th2A.47, 2017.
- [24] **(Invited)** William Shieh, An Li, **Di Che**, Feng Yuan, and Hamid Khodakarami, “*Stokes Vector Direct Detection for Optical Communications*,” Photonics West OPTO, San Francisco, CA, paper 10130-15, 2017.
- [25] **(Invited)** **Di Che**, Feng Yuan, Qi Yang, Hamid Khodakarami, Yifei Wang, Jian Fang, and William Shieh “*Reinventing Optical Direct Modulation by Frequency Chirp*,” Asia Communications and Photonics Conference, Wuhan, China, paper AF1C.3, 2016.
- [26] **Di Che**, Feng Yuan, Hamid khodakarami, and William Shieh, “*Duobinary Pulse-Shaped Complex Modulation of Directly Modulated Lasers*,” European Conference on Optical Communication, Dusseldorf, Germany, paper Tu.1.C.1, 2016.
- [27] **Di Che**, Feng Yuan, Qian Hu, and William Shieh, “*Complex Modulation of Directly Modulated Lasers for Medium Reach Optical Communications*,” Optical Fiber Communication Conference, Anaheim, CA, paper Tu2A.5, 2016.
- [28] **Di Che**, Feng Yuan, and William Shieh, “*Towards High-order PAM Utilizing Large Frequency Chirp of Directly Modulated Lasers*,” Optical Fiber Communication Conference, Anaheim, CA, paper W1A.4, 2016.
- [29] Feng Yuan, **Di Che**, Qian Hu, and William Shieh, “*Characterization of Thermal Frequency Modulation of a DFB Laser Using Digital Coherent Detection*,” Optical Fiber Communication Conference, Anaheim, CA, paper W2A.25, 2016.
- [30] **Di Che**, An Li, and William Shieh, “*Blind Polarization De-multiplexing for Stokes Vector Direct Detection*,” European Conference on Optical Communication, Valencia, Spain, paper Mo.3.5.5, 2015.
- [31] **(Top-scored)** **Di Che**, Qian Hu, Feng Yuan, and William Shieh, “*Enabling Complex Modulation Using the Frequency Chirp of Directly Modulated Lasers*,” European Conference on Optical Communication, Valencia, Spain, paper Mo.4.5.3, 2015.
- [32] Fred Buchali, Laurent Schmalen, Qian Hu, and **Di Che**, “*Low latency digital regenerator for dual polarization QAM signal*,” European Conference on Optical Communication, Valencia, Spain, paper Mo.3.3.5, 2015.
- [33] **(Invited)** **Di Che**, Qian Hu, and William Shieh, “*High-Spectral-Efficiency Optical Direct Detection Using the Stokes Vector Receiver*,” European Conference on Optical Communication, Valencia, Spain, paper Mo.3.5.4, 2015.
- [34] **Di Che**, Hamid Khodakarami, and William Shieh, “*Dual-Polarization Signal Carrier Interleaved Direct Detection Through Discrete-time Gaussian Channel with Conjugate Inter-symbol Interference*,” Opto Electronics and Communications Conference, Shanghai, China, 2015.
- [35] **(Top-scored)** **Di Che**, An Li, Qian Hu, Xi Chen, and William Shieh, “*Implementing Simplified Stokes Vector Receiver for Phase Diverse Direct Detection*”, Optical Fiber Communication Conference, Los Angeles, CA, paper Th1E.4, 2015.
- [36] Qian Hu, **Di Che**, Yifei Wang, and William Shieh, “*PMD induced impairment mitigation in Stokes vector direct detection systems*,” Optical Fiber Communication Conference, Los Angeles, CA, paper Th1E.2, 2015.

- [37] **(Invited)** William Shieh, **Di Che**, Qian Hu, and An Li, “*Linearization of Optical Channels with Stokes Vector Direct Detection*,” Optical Fiber Communication Conference, Los Angeles, CA, paper Th1E.5, 2015.
- [38] **(Invited)** **Di Che**, Xi Chen, An Li, Qian Hu, Yifei Wang, and William Shieh, “*Optical direct detection for 100G short reach applications*”, Asia Communications and Photonics Conference, Shanghai, China, paper AF1H. 4, 2014.
- [39] Qian Hu, **Di Che**, and William Shieh, “*Mitigation of PMD Induced Nonlinear Noise in Stokes Vector Direct Detection Systems*,” European Conference on Optical Communication, Cannes, France, paper P.3.4, 2014.
- [40] **(Post-Deadline)** **Di Che**, Qian Hu, Xi Chen, An Li and William Shieh, “*1-Tb/s Stokes Vector Direct Detection over 480-km SSMF Transmission*,” OptoElectronics and Communication Conference, Melbourne, Australia, paper THPDP1-3, 2014.
- [41] **Di Che**, Xi Chen, An Li and William Shieh, “*Signal-Carrier Interleaved Direct-Detection in Optical Single-Carrier Communication Systems*,” OptoElectronics and Communication Conference, Melbourne, Australia, paper WE8D-1, 2014.
- [42] Xi Chen, Jiayuan He, **Di Che**, and William Shieh, “*Low complexity phase noise compensation for multiband coherent optical OFDM*,” OptoElectronics and Communication Conference, Melbourne, Australia, paper TH10E-6, 2014.
- [43] **(Post-Deadline)** **Di Che**, An Li, Xi Chen, Qian Hu, Yifei Wang and William Shieh, “*160-Gb/s Stokes vector direct detection for short reach optical communication*,” Optical Fiber Communication Conference, San Francisco, CA, paper Th5C.7, 2014.
- [44] **Di Che**, Xi Chen, Jiayuan He, An Li, William Shieh, “*102.4-Gb/s Single-Polarization Direct-Detection Reception using Signal Carrier Interleaved Optical OFDM*,” Optical Fiber Communication Conference, San Francisco, CA, paper Tu3G.7, 2014.
- [45] Xi Chen, Jiayuan He, **Di Che** and William Shieh, “*Demonstration of Software-defined Multiband OFDM with Low-complexity Phase Noise Compensation*,” Optical Fiber Communication Conference, San Francisco, CA, paper Tu2G. 3, 2014.
- [46] Xi Chen, **Di Che**, An Li, Jiayuan He, Yifei Wang, Qian Hu and William Shieh, “*Training Symbol Assisted Signal-to-Signal Beat Noise Cancellation for Direct Detected Optical OFDM Systems*,” Asia Communications and Photonics Conference, Beijing, China, paper AF1E. 2, 2013.
- [47] An Li, **Di Che**, Xi Chen, Qian Hu, Yifei Wang and William Shieh, “*Signal-to-Signal Beat Noise Cancellation for Direct Detection Optical OFDM System Based on Block-wise Signal Phase Switching*,” Asia Communications and Photonics Conference, Beijing, China, paper AF1E. 6, 2013.
- [48] **Di Che**, Hamid Khodakarami, An Li, Xi Chen, Trevor Anderson and William Shieh, “*Receiver sensitivity enhancement by using subcarrier reliability aware soft LDPC in CO-OFDM systems*,” European Conference on Optical Communication, London, UK, paper P.3.25, 2013.
- [49] An Li, **Di Che**, Xi Chen, Qian Hu, Yifei Wang and William Shieh, “*48.8-Gb/s 16-QAM direct-detection optical OFDM based on block-wise signal phase switching*,” European Conference on Optical Communication, London, UK, paper P.4.6, 2013.
- [50] **(Post-Deadline)** Xi Chen, An Li, **Di Che**, Qian Hu, Yifei Wang, Jiayuan He and William Shieh, “*High-speed fading-free direct detection for double-sideband OFDM signal via block-wise phase switching*,” Optical Fiber Communication Conference, Anaheim, CA, paper PDP5B.7, 2013.

2. OPTICAL DETECTION METHODS

Optical signal carries information on various dimensions, such as intensity, phase and polarization. In this chapter, we confine the transmission medium to the single mode fiber (SMF), and discuss the optical detection methods. The task of optical detection is to down-convert the passband signal at optical frequency to the baseband signal at radio frequency (RF). Based on the modulation format, the detector can selectively recover one or multiple dimensions information.

2.1 Intensity-only direct detection

The simplest optical detector contains a photodetector (PD) shown in Figure 2.1. An ideal PD performs a square-law function to the optical field. The relationship between the photocurrent I and the electric field of optical signal E is expressed as:

$$I = R|E|^2 \quad (2-1)$$

where R is the responsivity of the PD. To simplify the analysis, below we set $R = 1$ without generality. PD realizes a linear mapping between the photocurrent and optical power, instead of the field.

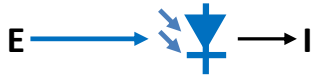


Figure 2.1 Intensity-only direct detection receiver.

2.2 Self-coherent differential-phase detection

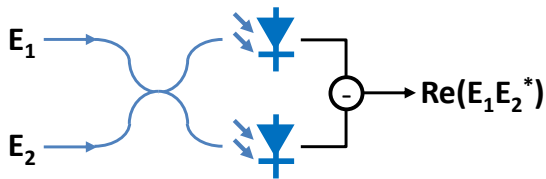


Figure 2.2 B-DPSK self-coherent receiver.

A self-coherent receiver [66-67] compares the optical signal $E(t)$ with its own delay $E(t - \tau)$, where τ is normally set as one symbol period T_s . The simplest self-coherent receiver contains a 2x2 optical coupler and a pair of PDs (namely, a balanced PD, B-PD), shown by Figure 2.2. $E(t)$ and $E(t - T_s)$ serves as the two inputs of coupler, results in the coupler outputs of $E(t) + E(t - T_s)$ and $E(t) - E(t - T_s)$. The corresponding B-PD output is:

$$I_i = \text{Re}\{E(t)E^*(t - T_s)\} \quad (2-2)$$

where Re represents the real part of a complex value, and the superscript $*$ represents the conjugate operation. When the modulation format is binary differential phase shift keying (B-DPSK), the sign of Eq. (2-2) determines the phase as 0 or π .

When the modulation order of differential phase increase to M (namely, M-DPSK), the self-coherent receiver requires the quadrature part, together with the in-phase signal acquired from Eq. (2-2). In this case, the 2×2 coupler needs to be upgraded to a 90° -degree optical hybrid. The hybrid contains a pair of 2×2 coupler and a 90° -degree phase shifter, as shown in Figure 2.3(a). When the two inputs of the hybrid are $E(t)$ and $E(t - T_s)$, respectively, the four outputs are:

$$\begin{aligned} H_1 &= E(t) + E(t - T_s) \\ H_2 &= E(t) - E(t - T_s) \\ H_3 &= E(t) - iE(t - T_s) \\ H_4 &= E(t) + iE(t - T_s) \end{aligned} \quad (2-3)$$

H_1 and H_2 are fed into a B-PD, resulting in the photocurrent expressed by Eq. (2-2). H_3 and H_4 are fed into another B-PD, resulting in the photocurrent of:

$$I_q = \text{Im}\{E(t)E^*(t - T_s)\} \quad (2-4)$$

where Im represents the imaginary part of a complex value. The differential phase between $E(t)$ and $E(t - T_s)$ can thus be expressed as

$$\varphi_{dif} = a \tan(I_i, I_q) \quad (2-5)$$

In fact, the inputs of Figure 2.3(b) can be generalized to two arbitrary optical signal, with electric field of E_1 and E_2 . The two outputs provide the full information of $E_1E_2^*$. This structure is named a standard coherent receiver, which can be applied to other more sophisticated optical detection structures.

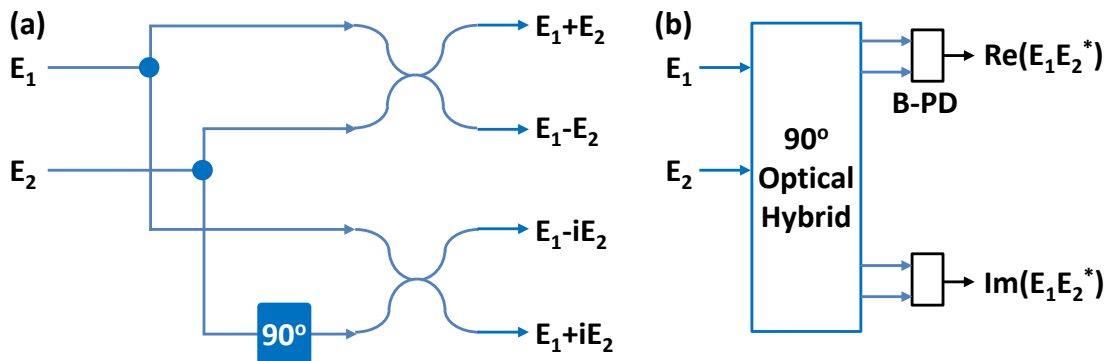


Figure 2.3 (a) 90° -degree optical hybrid; (b) M-DPSK self-coherent receiver.

2.3 3-dimension direct detection in Stokes space

The SMF naturally offers an extra degree of freedom for modulation – polarization [68], compared with the coax. When taking polarization into account, light transmitted along the SMF has capability to carry 3 or 4 dimensions information. This section introduces the signal representation in 3-D Stokes space.

Given the dual polarization signal in Jones space: $\mathbf{J} = [X, Y]^T$, where X/Y is the electric field of X/Y polarization, the Stokes vector (SV) $\mathbf{S} = (S_0, S_1, S_2, S_3)$ is defined as [68]:

$$\begin{bmatrix} S_0 \\ S_1 \\ S_2 \\ S_3 \end{bmatrix} = \begin{bmatrix} |X|^2 + |Y|^2 \\ |X|^2 - |Y|^2 \\ 2\text{Re}(X \cdot Y^*) \\ 2\text{Im}(X \cdot Y^*) \end{bmatrix} \quad (2-6)$$

As S_0 can be represented by: $S_0 = \sqrt{S_1^2 + S_2^2 + S_3^2}$, the SV is mapped in a 3-D space (S_1, S_2, S_3) , which can be directly detected by the SV receiver (SV-R) shown in Figure 2.4(a) [69-70]. The signal is first split with a polarization beam splitter (PBS) into two outputs of X and Y respectively. Both X and Y are split with 1×2 couplers, providing four output ports. Ports 1 and 4 are fed into a balanced PD directly, whose output is the 1st component of SV: $S_1 = |X|^2 - |Y|^2$. Ports 2 and 3 are fed into a coherent receiver, whose outputs are $\text{Re}(XY^*)$ and $\text{Im}(XY^*)$, as explained in Section 2.2. These are exactly the S_2 and S_3 . The SV-R can recover the signal in the Stokes space regardless of any transmitter structure or modulation format. For simplicity, the above analysis omits some simple scaling constants for couplers and PD outputs.

In fact, the SV-R can be generalized by any 3 or 4 detections of polarization states as long as they are non-singular superposition of the SV components (S_0, S_1, S_2, S_3) . Figure 2.4(b) provides an example [71]. After a PBS and couplers, ports 1 and 4 are launched into the PD directly, resulting in the outputs of $|X|^2$ and $|Y|^2$. Ports 2 and 3 are fed into the hybrid. Within the two pairs of outputs of hybrid, only two outputs are fed into the PDs, providing the outputs of $|X + Y|^2$ and $|X + iY|^2$ respectively. The 4 outputs provide a linear transformation to the SV expressed by:

$$\begin{bmatrix} S_0 \\ S_1 \\ S_2 \\ S_3 \end{bmatrix} = \begin{bmatrix} 1 & 0 & 0 & 1 \\ 1 & 0 & 0 & -1 \\ -1 & 1 & 0 & -1 \\ -1 & 0 & 1 & -1 \end{bmatrix} \begin{bmatrix} |X|^2 \\ |X + Y|^2 \\ |X + iY|^2 \\ |Y|^2 \end{bmatrix} \quad (2-7)$$

Another example in Figure 2.4(c) [72] uses polarizers to detect the power along different polarization axis. The linear transformation between the outputs and SV is:

$$\begin{bmatrix} S_0 \\ S_1 \\ S_2 \\ S_3 \end{bmatrix} = \begin{bmatrix} 1 & 0 & 0 & 0 \\ -1 & 2 & 0 & 0 \\ -1 & 0 & 2 & 0 \\ -1 & 0 & 0 & 2 \end{bmatrix} \begin{bmatrix} S_0 \\ I_x \\ I_{45^\circ} \\ I_R \end{bmatrix} \quad (2-8)$$

where I_x represents the power of X polarization; I_{45° is the power of 45° linearly polarized component; and I_R is the power of the right circularly polarized component.

For transmission distance <10 km, the optical link power budget is limited, and the PD noise becomes dominant. Figure 2.4(a) receives all the optical power, but it contains 6 PDs; Figure 2.4(b-c) reduces the PD amount to 4, but either the optical hybrid or the polarizers induce huge power loss. In this case, 3×3 120-degree optical hybrid can be applied to the SV-R, as shown in Figure 2.4(d). The linear transformation between the outputs and SV is:

$$\begin{bmatrix} S_0 \\ S_1 \\ S_2 \\ S_3 \end{bmatrix} = \begin{bmatrix} 1 & 1 & 1 & 1 \\ 3 & -1 & -1 & -1 \\ 0 & -\sqrt{2} & 2\sqrt{2} & -\sqrt{2} \\ 0 & -\sqrt{6} & 0 & \sqrt{6} \end{bmatrix} \begin{bmatrix} I_1 \\ I_2 \\ I_3 \\ I_4 \end{bmatrix} \quad (2-9)$$

SV-R can be regarded as a hybrid receiver of coherent and non-coherent detection. From S_0 and S_1 , the non-coherent information (intensity of X and Y) can be recovered; while from S_2 and S_3 , the coherent information between X and Y can be recovered.

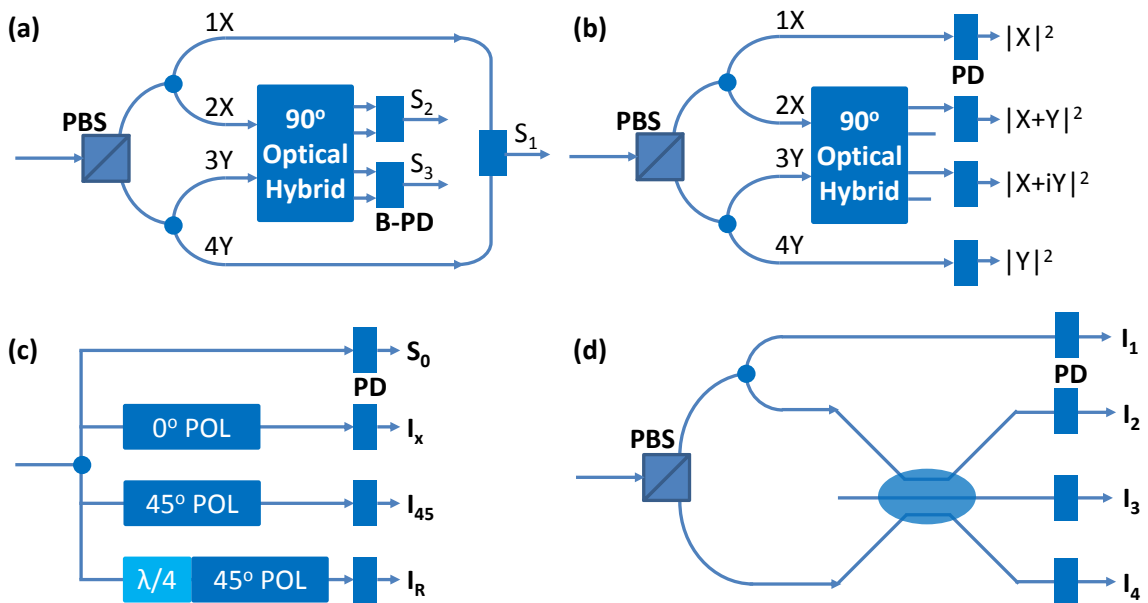


Figure 2.4 Stokes vector receiver.

2.4 4-dimension coherent detection in Jones space

The SV-R recovers 3-D information from the dual polarization signal: the intensity of X and Y polarizations, and the differential phase between X and Y polarizations. The only missing information is the absolute phase of the modulated signal. To characterize this, receiver requires a local oscillator (LO) to serve as an absolute phase reference. A single polarization coherent receiver has the structure introduced in Figure 2.3(b). The receiver output is $S \cdot C^*$, where S and C are the electric field of signal and LO, respectively. Coherent detection requires the carrier recovery, which retrieves the modulated phase from the phase of optical carrier (at transmitter) and LO (at receiver). Carrier recovery normally includes the LO frequency offset compensation and the phase noise estimation.

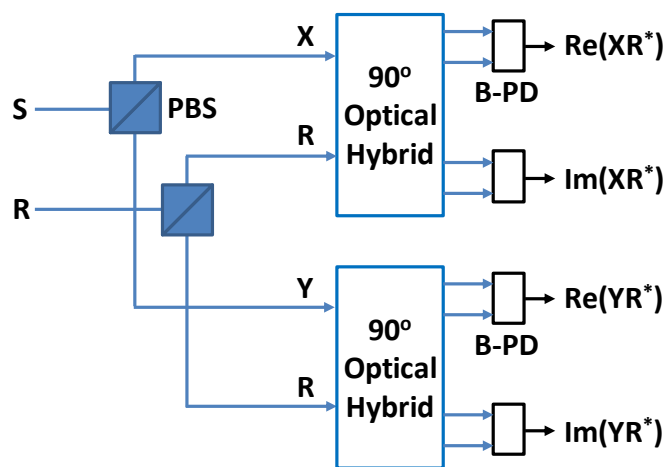


Figure 2.5 Dual-polarization coherent receiver. S : signal; R : light reference by the local oscillator.

To acquire full 4-D information in Jones space, coherent detection requires 2 sets of coherent receiver, as shown in Figure 2.5. The LO is polarized at 45° relative to the PBS, and the signal is separately demodulated by the coherent receiver, so that both the electric field of X and Y polarizations can be recovered. Polarization state changes randomly during fiber transmission due to the time-varying birefringence distributed along the fiber. One method to align the polarization between LO and signal is polarization controller [19-20]. However, the hardware enabled polarization tracking can be a huge challenge under large polarization variation speed. Moreover, the polarization mode dispersion (PMD) [68] induces the frequency dependent polarization variation, which is inevitable via a polarization controller. The state-of-the-art coherent detection uses DSP enabled 2×2 multi-input-multi-output (MIMO) polarization recovery, which digitally track the optical channel characteristics by the 2×2 Jones matrix.

2.5 Optical detection methods in this thesis

This thesis discusses a variety of coherent detection technologies for optical short-reach communications. The detection methods are not restricted to the narrow sense 4-dimension coherent detection introduced in Section 2.4, but extended to any detection

which makes use of the coherence between the optical signals. Remarkably, we will present in the following chapters that all the basic detection methods mentioned in this chapter can be applied to a generalized coherent-like system.

The coherent optical short-reach applications own advantages over the conventional optical intensity modulation – direct detection (IM-DD) system, for example:

- (1) Coherent detection linearly recovers optical field instead of intensity. DSP can thus be fully utilized to estimate the channel and compensate its impairments.
- (2) In IM-DD system, the fiber chromatic dispersion (CD) induces the frequency selective power fading, which results in irreversible information outage. As a result, single-carrier IM-DD system suffers from severe inter-symbol interference (ISI), which limit its transmission distance <10 km. Coherent detection fundamentally eliminates the problem. Much higher modulation format and longer distance can be undertaken.
- (3) In direct modulation IM-DD systems where frequency chirp used to be a dominant impairment, coherent detection converts this detrimental factor to a system benefit by recovering the expanded signal field spectrum.
- (4) By coherent technology, direct detection receiver can achieve multi-dimension detection, which doubles or even triples the optical spectral efficiency per wavelength. When using the double-sideband (DSB) modulation in RF domain, the RF bandwidth utilization ratio at receiver can reach 100%, which relieves the receiver bandwidth requirement.

3. SUBCARRIER RELIABILITY AWARE LDPC FOR CO-OFDM

Coherent detection is no doubt the ultimate solution for short-reach applications to breakthrough their bottlenecks in the future. In this chapter, we take the first step to reform the coherent technology for short-reach transmission by the forward error correction (FEC). The use of FEC avoids further resorting to the expensive optical devices or sophisticated digital signal processing (DSP) algorithms, making the system cost-efficient and reliable. The current optical coherent technology cannot live without the FEC [73-77]. In turn, the coherent detection provides much richer information to the soft decision (SD) FEC decoder, leading to more powerful and efficient FEC.

This chapter first introduces some basic concepts of FEC in optical communication, and then propose a novel SD-FEC scheme for a typical coherent system – coherent optical OFDM (CO-OFDM) [10,78], where OFDM subcarriers owns various signal-to-noise ratio (SNR). This information can be applied to the FEC decoder to obtain extra coding gain. Moreover, in coherent detection, subcarriers near the local oscillator (LO) have a severely degraded SNR caused by the so-called near-DC noise. While other subcarriers are error free, these subcarriers can still cause large amount of errors which greatly degrades the system performance. In wireless systems, near-DC subcarriers can be predicted by transmitter since LO has a stable frequency. Near-DC subcarriers are nullified to avoid near-DC noise [79]. Unfortunately, for the optical counterpart, LO could drift in a relatively wide frequency range [80-81] due to the uncertainty of laser wavelength; for low-cost short-reach applications, this problem is even more severe. We can still nullify all the subcarriers in the drifting range, but greatly sacrificing the optical spectrum efficiency (SE). Alternatively, precise wavelength control technology [80-81] can be applied. However, it is desirable to devise a scheme that is compatible with most of the commercial lasers which still have wide-range frequency drift when operated uncontrolled. We show below how the powerful FEC could be utilized to compensate the imperfect optical hardware.

3.1 Forward error correction codes in optical communication

FEC was initially introduced into optical fiber communications in 1990s for the ultra-long-haul transoceanic distance transmission [82-83]. FEC consists of an encoder at transmitter which adds redundant bits to the information bits; and a decoder at receiver which performs the error correction and extracts the redundancy to recover the original data. The first generation FEC in optical communication applied the Reed-Solomon (RS) code (e.g. RS (255,239)) to a broad range of long-haul systems as recommended by the International Telecommunication Union – Telecommunication Standardization Sector

(ITU-T). During this time frame, FEC decoders perform hard decision, which was based on single quantization level bit sampling. The wideband optical amplification supports the development of wavelength division multiplexing (WDM) in late 1990s, stimulating the desire of more powerful FEC. Concatenating orthogonal codes (e.g. RS (239,223) + RS (255,239)) were proposed for superior error correction. Interleaving and iterative decoding were combined with the concatenation, served as the second-generation FEC. The early 21st century witnessed the revival of coherent optical technology, which brings another round of optical channel capacity evolution. Coherent detection offers receiver much precise channel characteristics, supporting the powerful third generation soft-decision iterative FEC decoder. Nowadays, FEC has been adopted as a standard technique by the ITU-T G.975 (Forward error correction for submarine systems) and G.709 (Interfaces for the optical transport network).

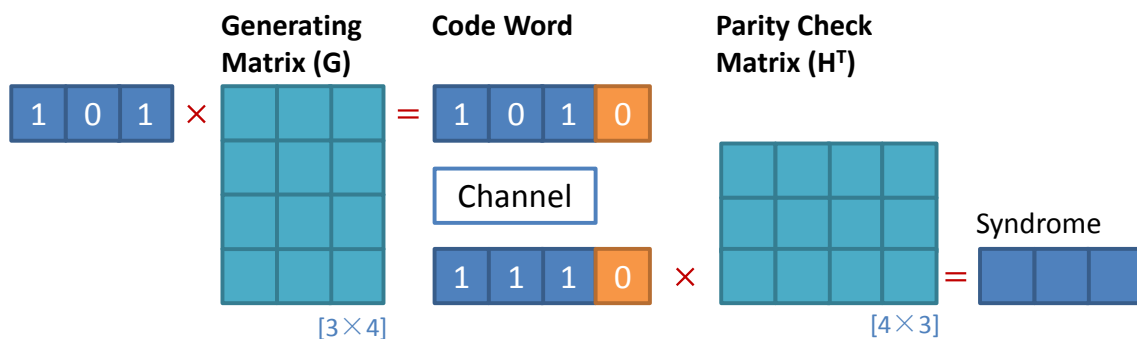


Figure 3.1 Encoding procedures for a linear block codes.

The HD decoder makes firm decision for every input and output bit as to whether the bit corresponds to 1 or 0. In contrast, the SD decoder [76] makes decision based on the probability of a bit of being 1 or 0. Currently, the most widely deployed SD FEC is the low-density parity check (LDPC) code [73,84-85]. LDPC code is a kind of linear block codes. An LDPC code with block length of n and check nodes number of $n - k$ can be expressed as LDPC (n,k) . An example of encoding procedure of linear block codes is shown in Figure 3.1. The input bit stream is first converted to the block form with block length of k . A block code (n,k) has its unique generating matrix $G_{k \times n}$. Multiplying each bit block to the G matrix generates the code word with length of n . The generating matrix of LDPC code is a sparse matrix. By properly design this sparse matrix, LDPC can become a capacity-approaching code. After the channel, the code word can be checked by a parity check matrix $H_{k \times n}$. The G matrix and H matrix satisfy the equation:

$$G \cdot H^T = 0 \quad (3-1)$$

Multiplying the code word to the H matrix generates the syndrome. A syndrome of $\vec{0}$ means the code word is correct.

The syndrome only tells the decoder whether the code word is right or not, but cannot correct the error when it is not a zero vector. To briefly explain the LDPC decoding

procedures, we illustrate the tanner graph of a simple LDPC (12,8) code in Figure 3.2. Within each block, there are 8 value nodes (v-node) and 4 check nodes (c-node). Each v-node has more than one c-node; and each c-node check more than one v-nodes.

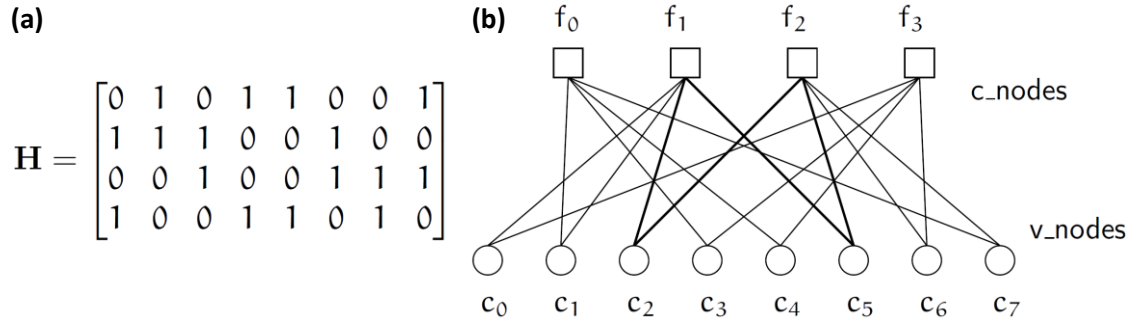


Figure 3.2 LDPC (12,8) code. (a) Generating matrix; (b) Tanner graph.

Below we compare the decoding between HD and SD methods. To simplify the explanation, we pick up a parity check group $\{f_0|c_1, c_3, c_4, c_7\}$. In practice, each step shown below needs to be performed to all the check groups.

Table III. LDPC decoding procedures

Step	HD	SD
1	Decoder performs hard-decision for each bit (f_{0-3}, c_{0-7} totally 12 bits) from the signal constellations	Decoder calculate the probability of each bit (f_{0-3}, c_{0-7} totally 12 bits) from the signal constellations
2	c_1, c_3, c_4, c_7 send their identity (1 or 0) to f_0	c_1, c_3, c_4, c_7 send their probability (of being 1 or 0) to f_0
3	Using the parity check equation, f_0 calculate the new identity to its value nodes. f_0 calculates c_1 from c_3, c_4, c_7 f_0 calculates c_3 from c_1, c_4, c_7 f_0 calculates c_4 from c_1, c_3, c_7 f_0 calculates c_7 from c_1, c_3, c_4 Calculations of f_{1-3} check groups Back to step 2 until the maximum iteration time	Using the parity check equation, f_0 calculate the new probability to its value nodes. f_0 calculates c_1 from c_3, c_4, c_7 f_0 calculates c_3 from c_1, c_4, c_7 f_0 calculates c_4 from c_1, c_3, c_7 f_0 calculates c_7 from c_1, c_3, c_4 Calculations of f_{1-3} check groups Back to step 2 until the maximum iteration time
4	Final hard decision	Final decision: if $P(1) > P(0)$ decided as 1; if $P(1) < P(0)$ decided as 0.

The above procedures are simplified for explanation. More detailed decoding can be found in Ref. [74]. As seen from the table, SD decoder cares about the bit probability, instead of its identity. A more reliable bit (with the probability close to 1 or 0) will contribute more during SD decoding. SD decoder takes more information of the signal constellation into account; thus provides much more coding gain compared with the HD decoder.

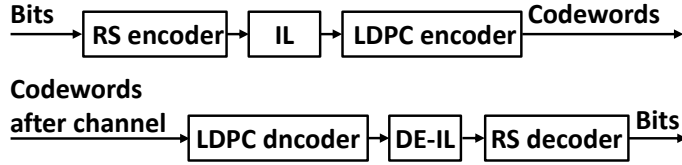


Figure 3.3 Concatenated LDPC and RS codes. IL: interleaver.

Although the LDPC code with SD iterative decoder shows superior error correction capability over the conventional HD decoder, it faces a tough problem: error-floor, often observed in the measured post-FEC BER. Like many iterative codes, the SNR vs post-FEC BER curve steepens with rising SNR, up to a point where it reaches a platform and the curve slope flattens. To solve the problem, the practical SD FEC scheme applies an LDPC as an inner code, concatenating it with an outer RS code to reduce the residual errors [74]. To avoid burst errors, an interleaver is inserted between the LDPC and RS code, as shown in Figure 3.3.

3.2 Subcarrier reliability aware (SRA) soft-decision LDPC codes

In this section, we propose a novel FEC coding scheme for the multi-carrier optical communication systems [86]. Conventional LDPC decoders assume that the noise variance of the bits is constant, and the probability density distribution of the bits (of being 0 or 1) is identical. However, for a typical multi-carrier system, SNR performance may differ among different subcarriers, due to the non-flat channel frequency response. The bits are mapped to different subcarriers and thus have differing noise variance. We term the varying SNR performance as varying degree of subcarrier reliability. By utilizing the subcarrier SNR information, the novel LDPC coding scheme becomes subcarrier reliability aware (SRA), which offers more decoding gain when applied to the multi-carrier system. Below we use OFDM as an example of multi-carrier modulation.

A. Decoding Mechanism

In soft-decision LDPC, log likelihood ratio (LLR) for each value node is computed to be later passed to the check node [74] (LLR plays the role of the “probability” shown in Table III). Assuming bits $\mathbf{b} = b_{m-1}b_{m-2} \cdots b_0$ are mapped to the complex constellation

point $c = c(\mathbf{b})$. We denote the received signal as $r = c + n$, where n represents additive white Gaussian noise. The LLR for the j -th bit of \mathbf{b} is defined as:

$$LLR_j = \log \left[\frac{P(b_j = 0 | r)}{P(b_j = 1 | r)} \right] = \log \left[\frac{p(r | b_j = 0)}{p(r | b_j = 1)} \right] \quad (3-2)$$

where P indicates a probability and p indicates a probability density function (PDF). We assumed the bits 0 and 1 are transmitted with equal probability. From the LLR definition, we know that when the absolute value of LLR is high, the probability difference between being 0 or 1 for variable nodes is large. Assuming the noise follows the 2-D Gaussian distribution with variance σ^2 , for $i \in \{0, 1\}$, p is expressed as:

$$p(r | b_j = i) = \sum_{\mathbf{b}: b_j = i} p(r | \mathbf{b}) = \sum_{\mathbf{b}: b_j = i} \frac{1}{2\pi\sigma^2} \exp \left(-\frac{\|r - c(\mathbf{b})\|^2}{2\sigma^2} \right) \quad (3-3)$$

In OFDM system, each constellation point c belongs to an OFDM subcarrier. By assuming that each subcarrier has a quasi-stationary SNR performance, we are able to use training symbols to estimate its noise variance σ^2 . Applying each σ^2 to corresponding constellation point, we reach the LLR for each value node. Then, the LLRs are sent to LDPC soft decoding iteration as the initialized value. Soft decoding exchanges the information between check nodes and variable nodes of LDPC codes and calculates new LLR at each iteration until the parity check is satisfied. In the following experiment, the soft-decoding uses sum-product algorithm [87]. The simplified min-sum algorithm [88] can also be applied due to its easy implementation.

B. Encoding Mechanism

Normally, only the LDPC decoder needs to be subcarrier reliability aware. Encoder adds the redundant check nodes to each subcarrier evenly.

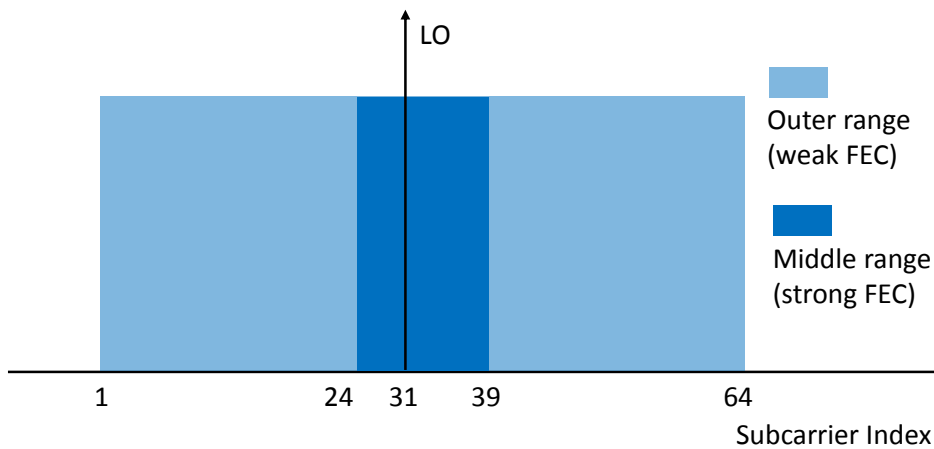


Figure 3.4 Subcarrier assignments for SRA-LDPC encoding.

However, subcarriers around the LO suffer from the near-DC noise and thus have an especially high BER. It is not efficient to spread this near-DC subcarrier error to all the subcarriers via interleaving, especially when other subcarriers are error-free. To solve this frequency-domain burst error problem, we categorize the OFDM subcarriers into two classes: (i) middle range: subcarriers located in the LO wavelength drift range, and (ii) outer range: subcarriers which are always free from near-DC noise no matter where the LO drifts. We assign strong FEC for subcarriers in middle range, and apply weak FEC to outer range subcarriers. Figure 3.4 shows one example of spectrum assignment. Since the transmitter cannot predict the exact location of the LO, we gauge the maximum drift range of the LO, which is assumed 1.25 GHz in this paper as can be reasonably achieved with commercially available lasers.

In the following experiment, for the strong FEC coding scheme, we use a 13% regular quasi-cyclic (QC) LDPC code concatenated with a 7% ITU standard RS code. RS (255,239) is used as the outer coding to compensate the error floor. QC-LDPC (2295, 2042) is adopted as the inner coding [89-90]. For the weak FEC coding scheme, we use the 7% RS code mentioned above. An interleaver is arranged between the two concatenated codes. Each RS symbol is consisted of 8 bits of information. As a result, the message and code lengths are 1912 and 2040, respectively. The LDPC code is designed for length compatibility to the RS output with 13% redundancy. A QC-LDPC (2295,2042) code can be contaminated with the above RS code by zero padding the output of the RS code for the remaining two bits (from length of 2040 to 2042).

In order to design QC-LDPC code of desired rate and message length, permutation block length and column and row weights of the parity check matrix should be determined [89]. The parity check matrix will have the following general form:

$$H = \begin{bmatrix} P^{c_{1,1}} & P^{c_{1,2}} & \dots & P^{c_{1,k}} \\ P^{c_{2,1}} & P^{c_{2,2}} & \dots & P^{c_{2,k}} \\ \vdots & \vdots & \ddots & \vdots \\ P^{c_{j,1}} & P^{c_{j,2}} & \dots & P^{c_{j,k}} \end{bmatrix} \quad (3-4)$$

where $c_{m,n}$ are determined through design to avoid short cycles and P is the permutation matrix given by:

$$P = \begin{bmatrix} 0 & 0 & \dots & 0 & 1 \\ 1 & 0 & \dots & 0 & 0 \\ 0 & 1 & \dots & 0 & 0 \\ \vdots & \vdots & \ddots & \vdots & \vdots \\ 0 & 0 & \dots & 1 & 0 \end{bmatrix} \quad (3-5)$$

It has been shown that the best column weight for regular LDPC codes is 3 [90]. Consequently, a QC-LDPC code of column weight 3 (and girth 6) is designed.

3.3 Experiment demonstration of SRA-LDPC codes

A 120-Gb/s CO-OFDM system is constructed to evaluate the performance of the SRA-LDPC coding [86]. The experimental setup is shown in Figure 3.5. The data stream is first divided into two parts to apply two different FEC schemes described in the last section. The two parts of data are separately encoded with the SRA-LDPC encoding mechanism and then modulated onto the 16-QAM constellation. These two parts need to be mapped into different ranges of OFDM subcarriers. To choose the size of middle range subcarriers, we assume that the frequency range of the LO drift is 1.25 GHz in this experiment. For OFDM modulation, FFT size of 128 is selected in which the center 64 subcarriers are filled with data. The OFDM signals are generated offline and then loaded to an arbitrary waveform generator (AWG) which is run at sampling rate of 10 GSa/s. This results in optical signal bandwidth of 5 GHz. The center 16 OFDM subcarriers (from 24th to 39th subcarrier as shown in Figure 3.4) are encoded with strong FEC. Twenty training symbols are used for channel estimation and subcarrier SNR estimation.

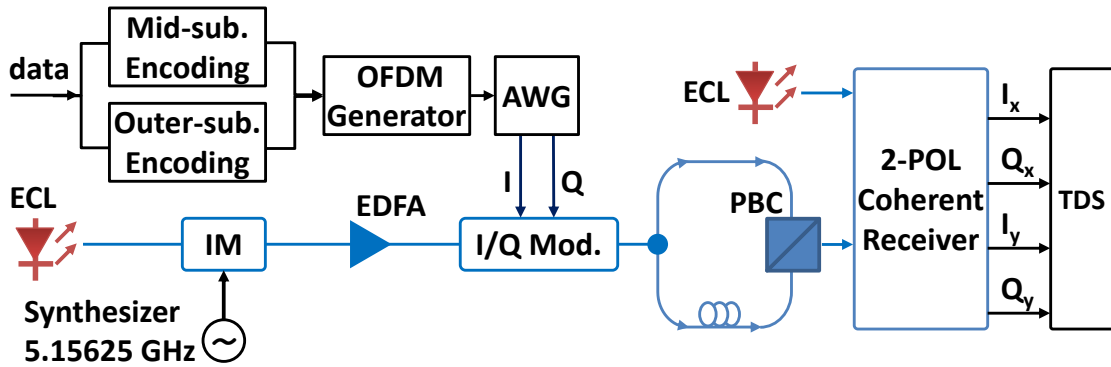


Figure 3.5 Experimental setup. AWG: Arbitrary waveform generator; IM: intensity modulator; PBC: Polarization beam combiner; LO: Local oscillator; ECL: External cavity laser; PD: Photodiode; TDS: Time-domain oscilloscope.

Due to the bandwidth limitation of the AWG, we employ optical band multiplexing using an optical tone generator. The optical tone generator consists of a CW laser and an intensity modulator, which produces three tones spaced at 5.15625 GHz. Such spacing is a multiple of the OFDM subcarrier spacing, which satisfies the orthogonal band multiplexing (OBM) condition [78]. To emulate 2x2 MIMO polarization multiplexing, the signal after the I/Q modulator is split by a polarization-maintaining coupler into two branches, with one branch delayed by one OFDM symbol. These two branches are combined with a polarization beam combiner (PBC), leading to the total raw data rate of 120 Gb/s. The polarization-multiplexed signal is subsequently coupled with an optical ASE noise loader using a 3-dB coupler, then fed into a coherent optical OFDM receiver, and sampled by a 50 GSa/s real time oscilloscope. The OFDM symbols are first recovered using standard 2x2 MIMO-OFDM procedures, and next sent to the FEC decoder which decodes data from different ranges of subcarrier separately. The number of bits used for BER computation is 7.35 million.

A. Influence of near-DC noise

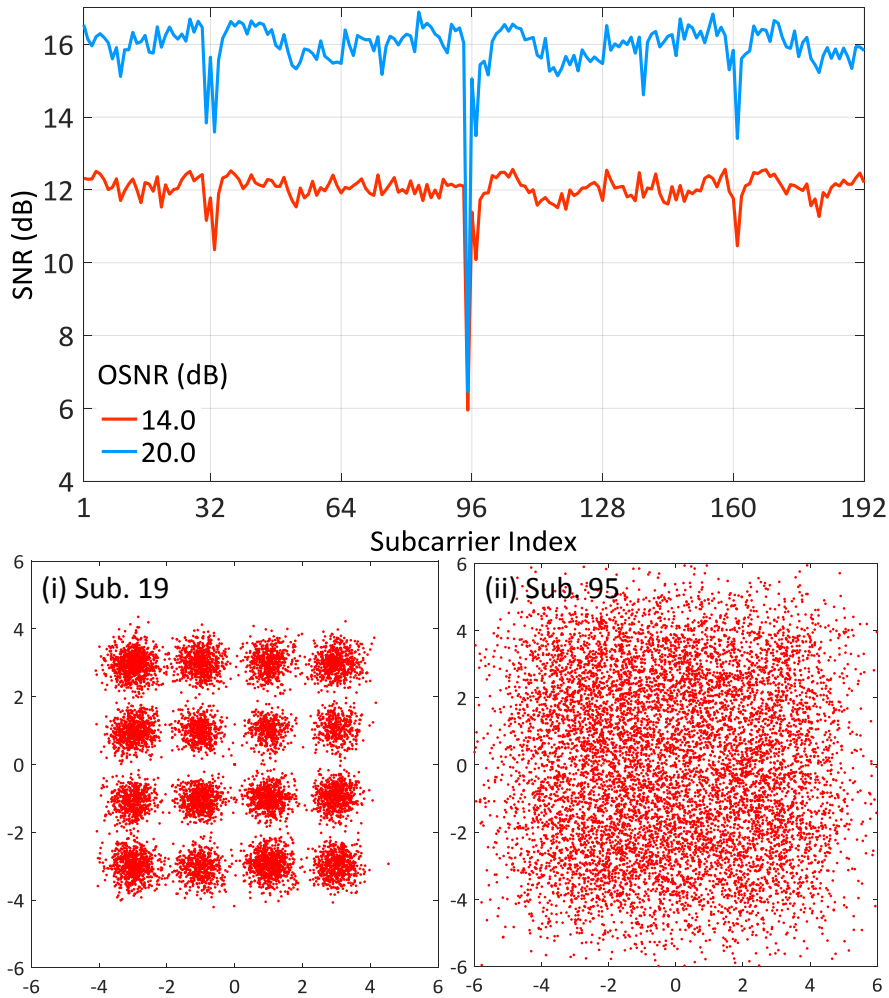


Figure 3.6 Subcarrier SNR distribution at OSNR of 14 and 20 dB. Inset (i) constellation of subcarrier 19; (ii) constellation of near-DC subcarrier 95.

We first confirm that the near-DC noise is detrimental to the overall system performance. To illustrate this, the distribution of subcarrier SNR under different OSNR is shown in Figure 3.6. The SNR is calculated from the variance of the signal constellation. For 3-band OFDM signal, the total number of filled subcarriers is 192. We can see that the SNR fluctuation is relatively small, except at those near-DC subcarriers which are represented by a deep ‘notch’. In this demonstration, the LO is located around the 95th subcarrier, where the SNR is much worse than the average level. We capture the constellations of the 19th subcarrier (far from LO) and the 95th subcarrier (near LO) in Figure 3.6 as insets. While the two insets are plotted with the same axis scale, constellation of the 95th subcarrier is obviously more scattered than the one for 19th subcarrier. In fact, as can be seen in Figure 3.7, while other subcarriers are almost error free at OSNR of 20, the BER for the 95th subcarrier exceeds 0.17. This means the near-DC noise does contribute most to the overall BER. There are three other subcarriers showing lower SNR (the 33rd, 97th, and 161th subcarrier), due to the contamination from the main carriers for the 3 bands added at the transmitter side. We do not apply special coding for them since the

transmitter knows the exact location of the main carriers, and thus can nullify those subcarriers.

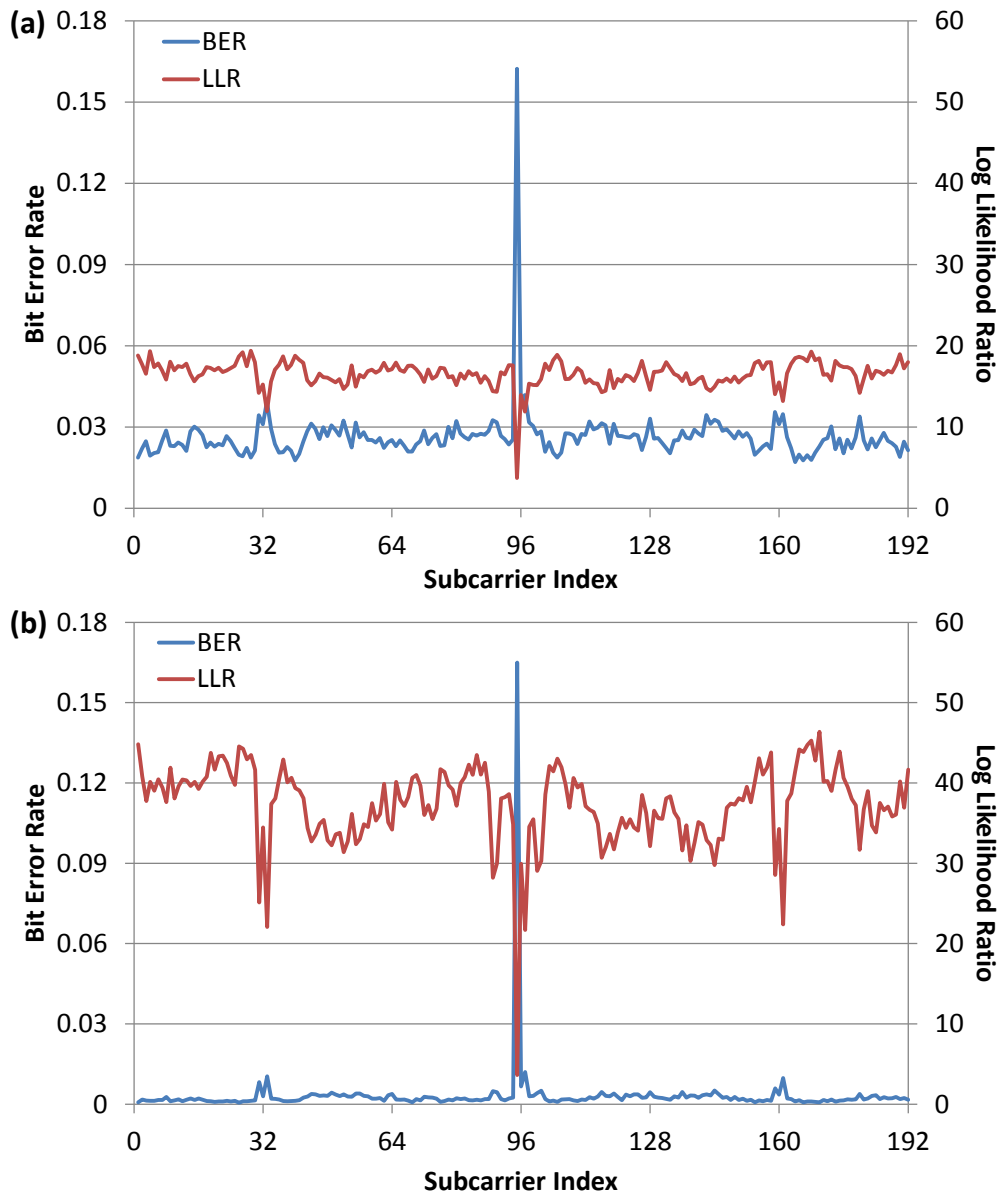


Figure 3.7 BER performance for all subcarriers (primary axis) and absolute value of LLR for LDPC value nodes within different subcarriers (secondary axis) at OSNR of 14 dB (a) and 20 dB (b). The LLR in this figure is the initial value (before LDPC iterative decoding) calculated from the constellation using Eq. (3-2) and (3-3).

Figure 3.7 further explains the decoding mechanism of SRA-LDPC code. When the absolute value of LLR is higher, the decoder makes the final decision for each variable node more reliably. Using the SNR illustrated in Figure 3.6, we calculate the initialized LLR for LDPC variable nodes from different subcarriers by Eq. (3-2). Since each subcarrier contains 4 coded bits in 16-QAM, we average the absolute value of LLR over these 4 nodes and reach the subcarrier LLR, which characterizes the subcarrier reliability. The mean value of subcarrier LLR over all the OFDM symbols is shown in Figure 3.7. Comparing the LLR curve at OSNR of 14 dB and 20 dB, we find that when the BER is low,

the absolute value of LLR becomes high. The phenomenon is more obvious if we compare the BER and LLR curves at OSNR of 20 dB. The LLR curve has totally opposite trend compared with the BER. At the 95th subcarrier, while BER is the largest, the LLR is closest to zero. Subcarrier with higher BER means lower reliability, while the absolute value of their LLR is much smaller than the average. Therefore, in soft-decision iteration, this LLR will have less weight in each step of calculation. This reliability awareness guarantees that the decoder limits the ‘error-propagation’ effect from those subcarriers with inferior SNR and contains their degrading impact on the decoding process.

B. Effectiveness of SRA-LDPC code

Figure 3.8 provides the BER performance measurement for our SRA-LDPC coding scheme. First from Figure 3.8(a), we find that the near-DC noise significantly degrades the decoding performance: when 7% FEC is applied across all the subcarriers, an error floor of 10^{-4} exists even when the OSNR is extremely high. When the same 7% FEC is applied to only outer subcarriers, neglecting the middle subcarriers, error-free performance can be achieved. This confirms that near-DC noise cannot be treated in the same way as the ordinary white Gaussian noise in decoding. Nevertheless, after applying our SRA-LDPC scheme, 20% FEC for the middle range and 7% for outer range, error-free performance is achieved, and the BER performance is almost identical to that of the outer range with 7% FEC. Moreover, our experimental results show that the decoding mechanism of SRA-LDPC code is not only effective, but also essential to achieve error-free performance. As shown in Figure 3.8(a), if we use constant noise variance of each subcarrier for decoding, there exists an error floor around 10^{-4} . The near-DC noise severely contaminates the LDPC decoding, thus even 20% FEC cannot compensate it if we do not keep track of noise variance. We note that in Figure 3.8(a) curves with FEC of “20% middle, 7% outer” have total data rate of 108.1 Gb/s while others have that of 107 Gb/s. This minor difference makes little impact to the comparisons.

We further study the effectiveness of SRA-LDPC decoding mechanism when 20% FEC is applied across all the subcarriers, without distinguishing the middle and outer ranges. Near-DC noise still significantly degrades the overall BER performance. When we neglect the near-DC subcarriers, the error-free OSNR sensitivity is about 15 dB. When we count near-DC subcarriers, the error-free OSNR sensitivity is larger than 16 dB, representing more than 1 dB degradation even if 20% FEC is used. In fact, no performance penalty caused by near-DC noise is observed when using SRA-LDPC code.

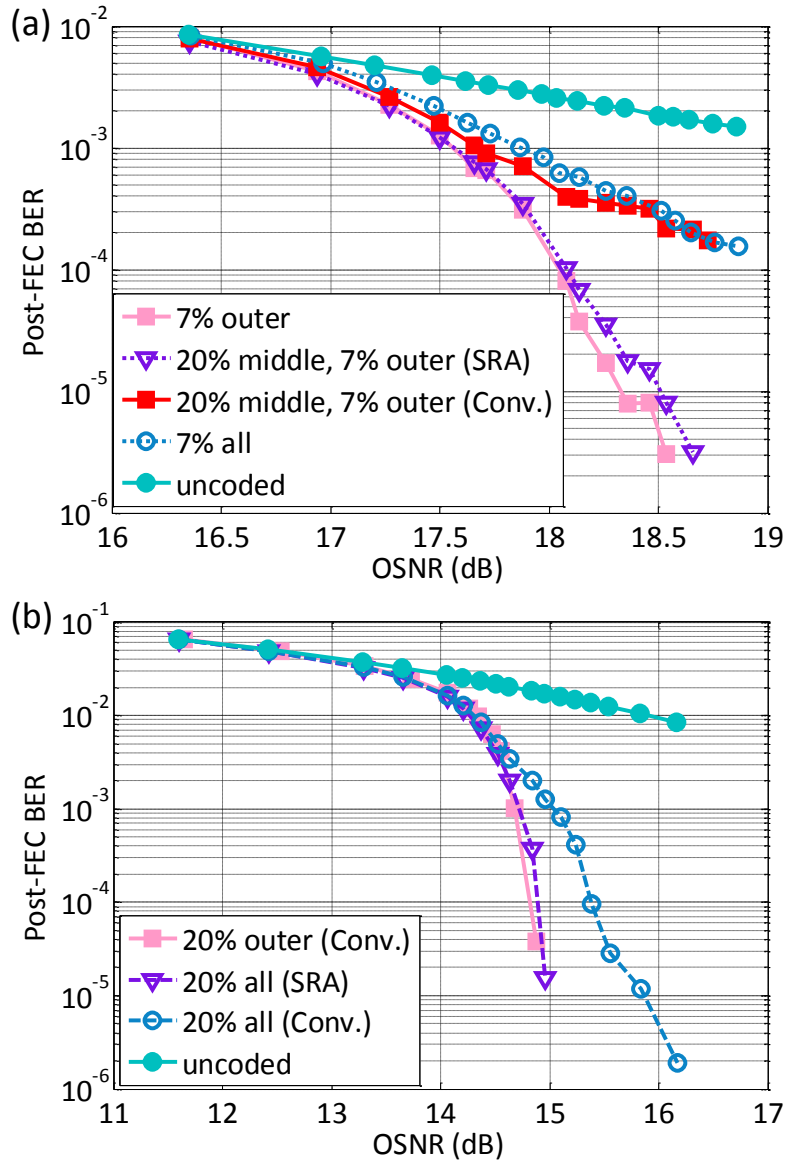


Figure 3.8 BER performance for 120-Gb/s 16-QAM CO-OFDM signal using (a) 7% FEC for the outer range, and (b) 20% FEC for the outer range. For both scenarios, 20% FEC is used for middle range subcarriers. SRA: LDPC that uses SRA decoding. Conv.: Conventional LDPC decoder which uses constant subcarrier noise variance when calculating LLR.

C. Performance Evaluation for SRA-LDPC code

The key issue of combating near-DC noise is that only a few subcarriers near the LO are affected by noise, whereas the LO drift range is relatively wide. Normally we can use bit-loading [91] to apply low order modulation format at subcarriers with low SNR. For example, we apply 4-QAM through middle range in the experiment. Since only the 95th subcarrier is strongly affected by the LO, we nearly sacrifice 50% spectral efficiency in the middle range. However, the 95th subcarrier still has a BER of over 0.02 for Q-factor of 6 dB with 4-QAM. Another method of handling “burst error” near LO is interleaving. Nevertheless, interleaving not only loses the SNR information for each variable node in

LDPC codes, but also requires more FEC overhead since bit error in one subcarrier spreads to the whole frequency band. In contrast, SRA-LDPC code only requires 20% overhead at middle range of 16 subcarriers. Averaging this value to the whole frequency band of 192 subcarriers, the mean overhead is just $16 \times 20\% / 192 = 1.67\%$. Moreover, by averaging the BER of 0.17 at LO subcarrier to 16 subcarriers in the middle range, the mean BER reduces to 0.01, far less than the threshold of 20% FEC. In fact, SRA-LDPC code converts the uncertain LO drift problem to an averaged BER problem which can be successfully handled by the state of the art FEC technology.

3.4 Conclusions

This chapter describe a novel scheme of utilizing the advanced forward error correction to enlarge the coding gain in the multi-carrier coherent system, meanwhile compensate the optical hardware imperfection (the local oscillator with large linewidth and wide frequency drift). Together with coherent detection, FEC will no doubt become an indispensable module for the future high-speed short-reach applications.

This chapter contains published contents from Ref. [86]. The thesis author is the primary author of the publication and has contributed more than 50 per cent of the work.

4. FREQUENCY CHIRP ENABLED COMPLEX MODULATION

In early 1990s, the commercialization of 2.5-Gb/s submarine optical fiber links using direct modulation (DM) and direct detection (DD) drove the development of internet as a global phenomenon. However, the detrimental frequency chirp [3,38-39] of directly modulated lasers (DML) impeded its application to the subsequent 10-Gb/s evolution.

In terms of transmission beyond Cat. II (in Table I) where chromatic dispersion becomes a dominant channel impairment, industry nowadays offers the 100 Gb/s per channel solution by external modulation (EM) and coherent detection (COHD), to avoid the DM chirp effect. EM-COHD transceivers employing the dual polarization (DP) QPSK [92] have already been commercialized. However, for medium-reach applications, there exists an incentive to find a compromise between the DM-DD and EM-COHD. Especially, EM faces the following shortcomings when applied to medium reach applications: (1) the price is 2 to 3 orders higher than DML, making it cost-inefficient; (2) the high insertion loss of EM reduces the power budget, which is not suitable for passive optical networks without extra amplification; (3) the bulky combination of laser and EM prevents them from integrating to the compact transmitter optical sub-assembly (TOSA). As a result, there emerged the revival of interest in DML as a replacement of EM transmitter in coherent system [34,93-98]. Ref. [93] offers a DML based I/Q transmitter, but it relies on the sophisticated optical injection locking, which requires a narrow linewidth master laser besides DMLs. Ref. [34] demonstrates the VCSEL based DP PAM-4 transmitter. Nevertheless, the coherent receiver makes decision only by optical intensity and discards the phase information, which leads to a large performance gap between PAM-4 and QPSK.

The DML frequency chirp has long been regarded as a performance barrier in optical transmission systems. However, when COHD is applied to DML based systems, the chirp induced laser frequency modulation (FM) can be detected at receiver by the local oscillator (LO), which provides a reference wavelength to characterize the shift. By time integral, frequency shift can be converted to phase variance. In essence, DML can realize the 2-dimensional (2-D) complex modulation, while coherent receiver recovers both the optical intensity and phase. We name this modulation concept as complex direct modulation (CDM). Normally, PAM has a large OSNR sensitivity gap with QAM systems, which strongly limits its achievable transmission distance. QAM naturally owns its superior tolerance to the channel additive white Gaussian noise (AWGN) over PAM, due to its 2-dimensional (2-D) modulation. Using CDM, the OSNR sensitivity of PAM system can be significantly improved, which offers a much-elongated transmission distance beyond 1000 km.

As mentioned in Section 1.4, the chirp-induced FM expands the optical spectrum. It is well known that FM can exchange the spectrum resources with the SNR by adjusting the modulation depth [99]. Coherent detection elongates the transmission distance of DM, because it not only enables the digital dispersion compensation, but also recovers an expanded optical field spectrum, which realizes the SNR advantage of FM by sacrificing the spectrum resources.

4.1 Discrete signal model for laser frequency chirp

A semiconductor laser can be directly modulated via the drive current. The drive current changes the carrier density inside the semiconductor medium, leading to the refractive index (RI) variation of the medium. The RI variation results in a frequency modulation (FM) [100] of the output optical field, together with the desired intensity modulation (IM). This parasitic FM, normally named as chirp, brings negative impact on the conventional DM-DD link. The most significant impairment of chirp is the spectrum expansion of the output optical field. Under chromatic dispersion (CD), wider spectrum leads to an increase in the spreading of optical pulses.

Derived from laser diode rate equations, the frequency chirp can be expressed directly by the laser output power $P(t)$ [3]

$$\Delta f = \frac{\alpha}{4\pi} \left(\frac{d}{dt} \ln P(t) + \kappa \cdot P(t) \right) \quad (4-1)$$

where $P(t)$ is the signal intensity, α is the laser linewidth enhancement factor, and κ is the adiabatic chirp coefficient.

In conventional EM based QAM system, the 2-D signal constellation is a prior knowledge for demodulation. For CDM, receiver knows the signal intensity constellation from PAM modulation, but misses a proper model for phase dimension. We then perform time integral to the frequency chirp in Eq. (4-1), and reach the phase variance $\varphi(t)$ expressed below:

$$\varphi(t) = \frac{\alpha}{2} (\ln P(t) + \int \kappa P(t) dt) + \varphi_0 + \varphi_N(t) \quad (4-2)$$

where φ_0 is the initial phase, and φ_N is the laser phase noise. Different from the conventional modulation, the constellation point of CDM at each sampling point is not identical independent distributed (i.i.d.); instead, $\varphi(t)$ is determined by all the past signals due to the integral operation, namely, the optical channel has a long memory. The maximum likelihood sequence estimation (MLSE) can be applied to such a channel, but the computational complexity will be extremely high. To simplify this channel model, we calculate the differential phase between the two consecutive symbols at time t_1 and t_2 :

$$\Delta\varphi = \frac{\alpha}{2} \left(\ln \frac{P(t_2)}{P(t_1)} + \int_{t_1}^{t_2} \kappa P(t) dt \right) + (\varphi_N(t_2) - \varphi_N(t_1)) \quad (4-3)$$

By assuming a quasi-constant laser phase noise during $[t_1, t_2]$, $\Delta\varphi$ is free from the phase noise contamination. Moreover, the equation removes the integral within $[0, t]$, while only retains the integral within a symbol period $[t_1, t_2]$. Using the integral mean value theorem, Eq. (4-3) can be further simplified:

$$\Delta\varphi = \frac{\alpha}{2} \left(\ln \frac{P(t_2)}{P(t_1)} + \kappa \frac{P(t_1) + P(t_2)}{2} \cdot T \right) \quad (4-4)$$

where $T = t_2 - t_1$ is one symbol period. Eq. (4-4) is the discrete signal approximation of laser frequency chirp.

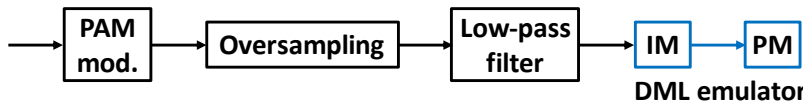
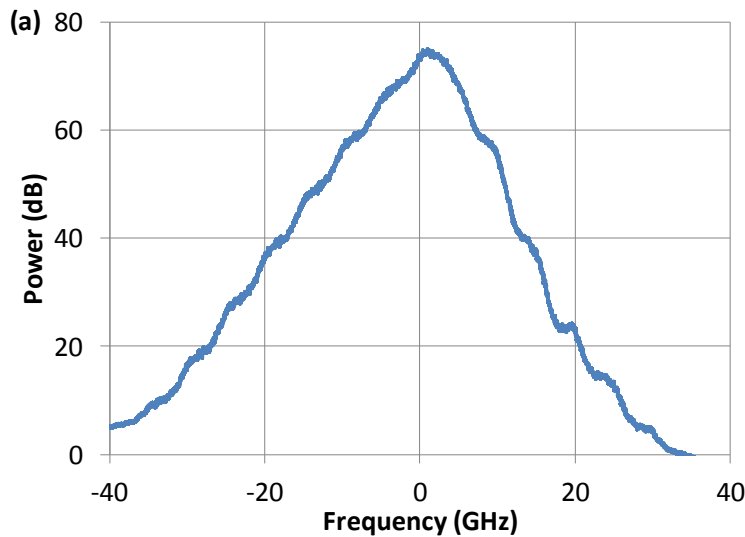


Figure 4.1 Simulation procedures for obtaining spectra after direct modulation with frequency chirp.

Obviously, there is no linear mapping between the baseband spectrum and optical spectrum. The optical bandwidth is determined not only by the baseband signal, but also by chirp parameters. Below we define $c_1 = \alpha/2$ and $c_2 = \alpha\kappa T/4$. Using Eq. (4-4), we can numerically simulate the optical spectrum and estimate the bandwidth [101], with the procedures shown in Figure 4.1. We take a 10-Gbaud PAM-4 signal as example. The DML in the simulation has $c_1 = 2$ and $c_2 = 1.5$ (normalizing the optical power to 1). It is noted that c_2 should be divided by the oversampling rate in the DML emulation.

Figure 4.2(a) shows the broadened spectrum at baseband. As a comparison, the measured spectra from the optical spectrum analyzer are shown in Figure 4.2(b). Figure 4.2(a) and (b) indicate that the simulation and experiment spectra coincide well, taking into account that 0.1 nm corresponds to 12.5 GHz around 1550 nm wavelength.



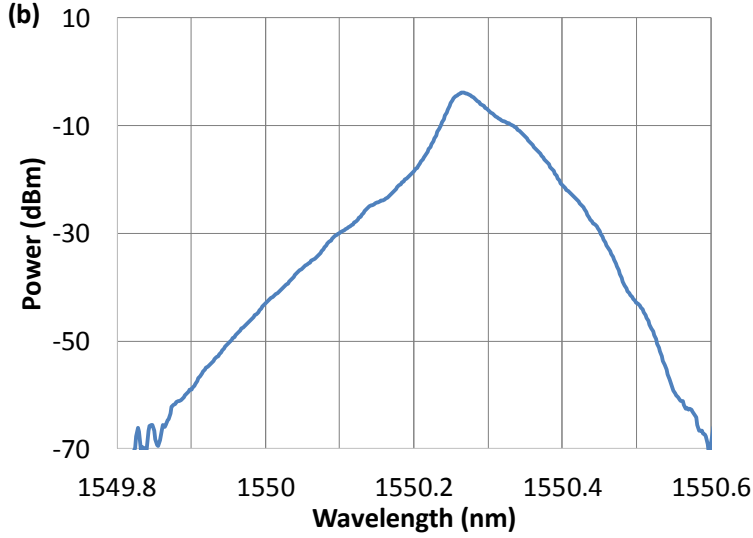


Figure 4.2 10-Gbaud PAM-4 signal spectra. (a) simulation spectra after direct modulation with frequency chirp; (b) measured spectra from the optical spectrum analyzer. Around 1550-nm wavelength, 0.1 nm corresponds to 12.5 GHz bandwidth. This offers a fair conversion of the horizontal axis unit between figure (a) and (b).

4.2 Chirp parameters characterization using coherent detection



Figure 4.3 Training patterns for laser frequency chirp coefficients.

Given the digital signal approximation of the frequency chirp in Eq. (4-4), a remaining task is to estimate the chirp parameters, in order to grasp the laser modulation characteristics. Chirp estimation has been widely investigated during the last few decades [102-104], mainly adopting a DD characterization system. DD cannot recover the signal phase, so previous systems have to apply sophisticated optical hardware structure, such as the Mach-Zehnder interferometer to estimate FM intermediately. When using COHD, chirp estimation becomes straightforward [97]. $\Delta\varphi(t)$ in Eq. (4-4) contains two parts: (i) the logarithmic part $\ln P(t_2) - \ln P(t_1)$ has a coefficient $c_1 = \alpha/2$; and (ii) the linear part $P(t_1) + P(t_2)$ has a coefficient $c_2 = \alpha\kappa T/4$. To estimate c_1 , we simply send a periodic PAM-2 pattern shown in Figure 4.3(a). The letter “L” stands for low power level while “H” is high level. By calculating the difference between $\Delta\varphi_{L\rightarrow H}$ and $\Delta\varphi_{H\rightarrow L}$, the linear part in Eq. (4-4) can be subtracted, and c_1 can be expressed as:

$$c_1 = \frac{\Delta\varphi_{L\rightarrow H} - \Delta\varphi_{H\rightarrow L}}{2(\ln P_H - \ln P_L)} \quad (4-5)$$

To estimate c_2 , we send a periodic PAM-2 pattern in Figure 4.3(b). By using two identical adjacent symbol, the logarithmic part can be cancelled, and c_2 can be express as:

$$\begin{aligned} c_2 &= \Delta\varphi_{L \rightarrow L} / 2P_L \\ c_2 &= \Delta\varphi_{H \rightarrow H} / 2P_H \end{aligned} \quad (4-6)$$

A differential operation can be applied between the two equations to improve the c_2 estimation accuracy:

$$c_2 = \frac{\Delta\varphi_{H \rightarrow H} - \Delta\varphi_{L \rightarrow L}}{2(P_H - P_L)} \quad (4-7)$$

It is noted that the chirp coefficients only need to be estimated initially at the acquisition stage and then can be regarded as a constant.

In fact, by the advanced digital COHD, the previously sophisticated DD characterization of semiconductor laser related to the phase can be efficiently simplified. For example, Ref. [105] presents a characterization method of thermal frequency modulation, which follows the similar idea we described in this Section.

4.3 Maximum likelihood sequence estimation (MLSE) for CDM

The coherent receiver recovers the signal intensity $P(t)$ and differential phase $\Delta\varphi(t)$ at each sampling point. Considering the channel has 2-tap memory, the MLSE [53] can be applied to demodulate the signal. Especially, we use Viterbi algorithm (VA) [106] to simplify the MLSE process [97]. We define two sets for the VA: (i) the state $\{x_t\}$ (each state corresponds to a constellation point); (ii) the transition $\{\chi_t | \chi_t \triangleq (x_t, x_{t-1})\}$. The transition is a state pair containing the states at the adjacent sampling points. As an example, when 4-PAM modulation is applied, there are 4 possible states in total (corresponding to 4 power levels) at each sampling point, and 16 possible transitions. The transition probability $P(\chi_t)$ characterizes the posterior possibility of each transition, which can finally determine the maximum likelihood sequence. MLSE decoder picks up the state pair (x_t, x_{t-1}) ; substituting (x_t, x_{t-1}) to Eq. (4-4), the estimated difference phase $\Delta\varphi_E(t)$ of the transition can be calculated. $P(\chi_t)$ thus can be characterized by the distance between the estimated values $\{x_{t-1}, x_t, \Delta\varphi_E(t)\}$ and measured values $\{P(t-1), P(t), \Delta\varphi(t)\}$. This distance can be defined by the pure phase information:

$$\lambda(\chi_t) = |\exp(i\Delta\varphi(t)) - \exp(i\Delta\varphi_E(t))|^2 \quad (4-8)$$

or based on both intensity and phase:

$$\lambda(\chi_t) = |P(t-1) - x_{t-1}| + |\sqrt{P(t)} \cdot \exp(i\Delta\varphi(t)) - \sqrt{x_t} \cdot \exp(i\Delta\varphi_E(t))|^2 \quad (4-9)$$

The smaller the $\lambda(\chi_t)$ is, the larger the possibility is for the transition.

We define two storages for VA. At each time t , we define (1) the survivors $\hat{\mathcal{S}}(x_t)$, which contain all the transitions from x_1 to x_k with the smallest sum of transition distance;

and (2) the survivor lengths $\Gamma(x_t)$, which store the sum of the transition distance. The VA procedures are shown below:

Initialization

- 1 $t = 1$
- 2 $\hat{s}(x_1) = x_1$;
- 3 $\Gamma(x_1) = 0$.

Operation at time t

- 1 Compute $\Gamma(x_{t+1}, x_t) = \Gamma(x_t) + \lambda(\chi_t)$
for all the $\chi_t = (x_{t+1}, x_t)$
- 2 Find $\Gamma(x_{t+1}) = \min_{x_t} \Gamma(x_{t+1}, x_t)$;
- 3 Update $\hat{s}(x_{t+1})$: add the x_t to it
Update $\Gamma(x_{t+1})$.

The survivor number is the same as the state number. These survivors would converge after the VA trace-back decoding depth. This convergent trace is the desired maximum likelihood sequence.

4.4 CDM PAM-4: approaching QPSK in terms of OSNR sensitivity

The PAM-4 modulated DML transmitter is now a promising candidate for the very short reach (<10 km) optical point-to-point connection, which has been extensively studied [107-108]. However, normally PAM has a large OSNR sensitivity gap with the QAM systems [34], preventing its application to the optical transmission where amplified spontaneous noise (ASE) is dominant. Using CDM, this gap can be greatly shrunk.

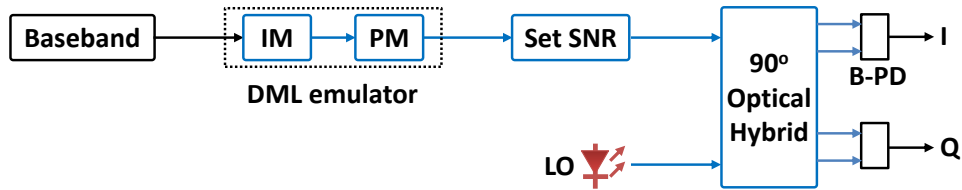


Figure 4.4 Simulation setup. IM: intensity modulation; PM: phase modulation; B-PD: balanced photo-detector; I/Q: in-phase/quadrature.

We conduct numerical simulation in Figure 4.4 to investigate the CDM performance. The DML emulator first maps the baseband signal to discrete intensity levels via intensity modulation; then adds phase modelled by Eq. (4-4) with the initial phase of 0. We ignore phase noise and other detrimental DML effects to reveal the optimal performance of CDM. The channel is modelled as additive white Gaussian noise (AWGN) channel, which adds ASE noise to signal field. The optical signal is launched into a standard coherent receiver.

We set $c_1 = 1.8$ and $c_2 = 0.5$ for PAM-4 signal (power level: [1 2 3 4]), which are the DML chirp parameters we measured from our previous experiment [98]. Figure 4.5 shows the BER as the function of channel SNR. The figure indicates two crucial facts: (i) both CDM schemes show more than 10-dB SNR sensitivity advantage over the conventional IM-DML with coherent detection; (ii) CDM PAM-4 has 6-dB SNR sensitivity penalty at 7% FEC threshold while only 5-dB at 20% FEC threshold compared to QPSK, which greatly shrinks the SNR sensitivity gap between PAM-4 and QPSK.

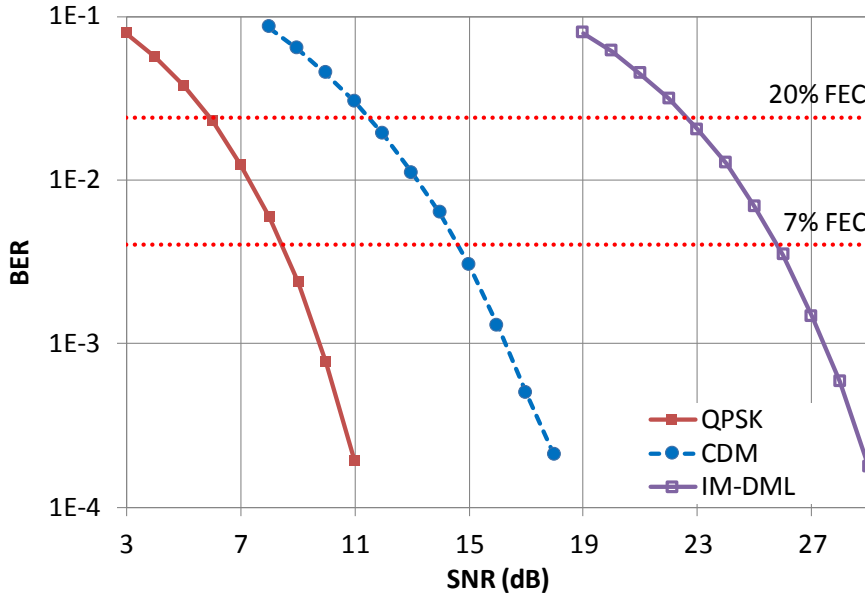


Figure 4.5 SNR sensitivity comparison among 4-level modulations. CM: complex modulation; IM: intensity modulation; 7% FEC: HD-FEC threshold of 3.8×10^{-3} ; 20% FEC: SD-FEC threshold of 2.4×10^{-2} . CDM in this figure utilizes Eq. (4-9) for MLSE.

The differential phase greatly enhances the capability of receiver to distinguish the 4 power levels. In fact, differential phase has long been utilized to improve system OSNR sensitivity. As one classic example, the differential QPSK (DQPSK) transceiver [109-110] now has been commercialized in market. QPSK with coherent detection no doubt gives the best SNR sensitivity for 4-level modulations. For DQPSK, when the receiver reconstructs the differential phase and conducts MLSE for symbol decision, the SNR sensitivity sacrifice by about 2 dB. This sets an achievable sensitivity limit for any 4-level modulation which uses differential phase aided MLSE for symbol decision.

In CDM, chirp coefficients c_1 and c_2 play significant roles in determining the discrete values of differential phases, which finally determines the system OSNR sensitivity. c_2 is related to the symbol period, which is hard to be determined for elastic transmitter configuration. Thus, to preliminarily investigate the impact chirp coefficients on SNR sensitivity, here we set $c_2 = 0$ to reveal the impact of c_1 . In this case, the maximum differential phase $\Delta\varphi_{max}$ is achieved when the adjacent power levels are 1 and 4: $\Delta\varphi_{max} = c_1 \ln 4$. Figure 4.6(a) shows the SNR sensitivity using various c_1 values. As the c_1 value increases, SNR sensitivity gradually improves. Opposite to the conventional

thinking which believes larger chirp would always results in worse performance, CDM requires a relatively large chirp to support its complex modulation. However, after c_1 becomes sufficiently large, OSNR sensitivity begins decreasing. The best sensitivity is achieved within the c_1 range of [3.40 4.53], corresponding to the $\Delta\varphi_{max}$ of $[1.5\pi 2\pi]$. This means the chirp coefficients have optimal values for the CDM PAM-4, instead of increasing monotonically.

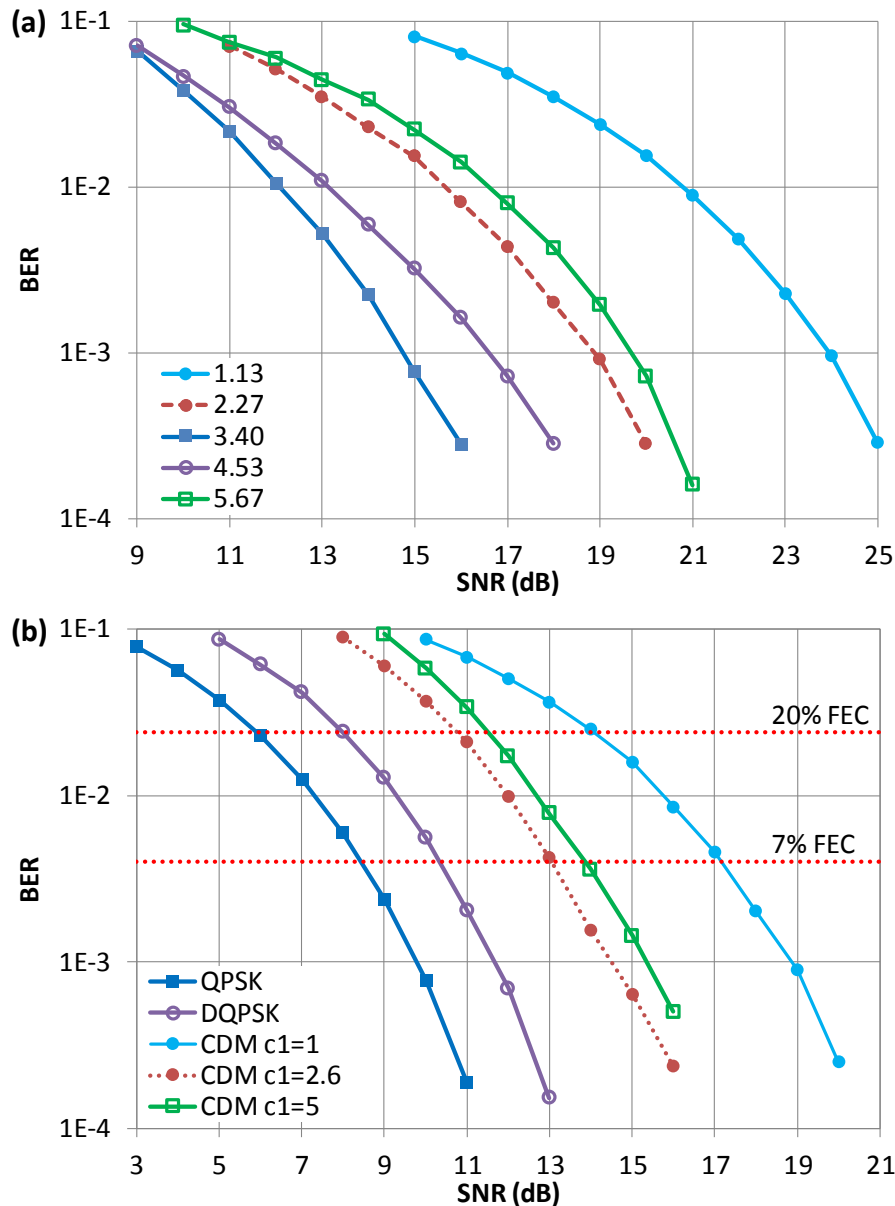


Figure 4.6 SNR sensitivity comparison using different frequency chirp parameters. (a) $c_2=0$, various c_1 ; (b) $c_2=0.5$, various c_1 ; 7% FEC: HD-FEC threshold of 3.8×10^{-3} ; 20% FEC: SD-FEC threshold of 2.4×10^{-2} .

We further add the value of c_2 as 0.5 in the simulation. When $c_1 = 1.8$, CDM achieves a sensitivity gap of 6 dB with QPSK at 7% FEC threshold in Figure 4.5. Some low chirp DMLs have c_1 of about 1 [102]; keeping c_2 as 0.5, the gap expands to 9 dB in Figure 4.6(b), as our expectation. Further increasing c_1 to 2.6, the gap shrinks to 5 dB, and a c_1 of 5 again expands the gap to 6 dB. The tendency follows the conclusions we reveal in the above

paragraph. In fact, for a specific DML with certain modulation parameters and working condition, the maximum achievable sensitivity is determined. Under the maximum achievable sensitivity set by DQPSK, there is an interesting pathway of CDM towards the performance limit, when various combinations of c_1 and c_2 are selected.

4.5 NRZ PAM-4 transmission experiment

We experimentally demonstrate the 10-Gbaud DP PAM-4 transmission using CDM and coherent detection [97]. Owing to its superior OSNR sensitivity improvement over IM-DML, CDM achieves a BER under 7% FEC threshold even after transmission over >1000 km standard single mode fiber (SSMF). The experimental setup is illustrated in Figure 4.7. The baseband PAM-4 signal is generated by an arbitrary waveform generator (AWG) sampling at 10 GSa/s. This RF signal drives a distributed feedback (DFB) laser working around the wavelength of 1550 nm, with linewidth of 10 MHz. The DFB is biased at the linear response range, leading to an intensity equally spaced optical signal. The output light is fed into a DP emulator, which splits the signal into two paths, with one path delayed by 600-meter SSMF to achieve phase de-correlation. After power balance, these 2 paths are combined with a polarization beam combiner (PBC) and then launched into a recirculating loop which consists of 1 span of 80-km SSMF and an EDFA to compensate the loop loss of 17 dB. The EDFA noise figure is 6 dB. The optical spectrum at the output of DP emulator is captured in Figure 4.8. The 10-dB optical bandwidth of this 10-Gbaud signal is about 0.2 nm, which is broadened by the frequency chirp.

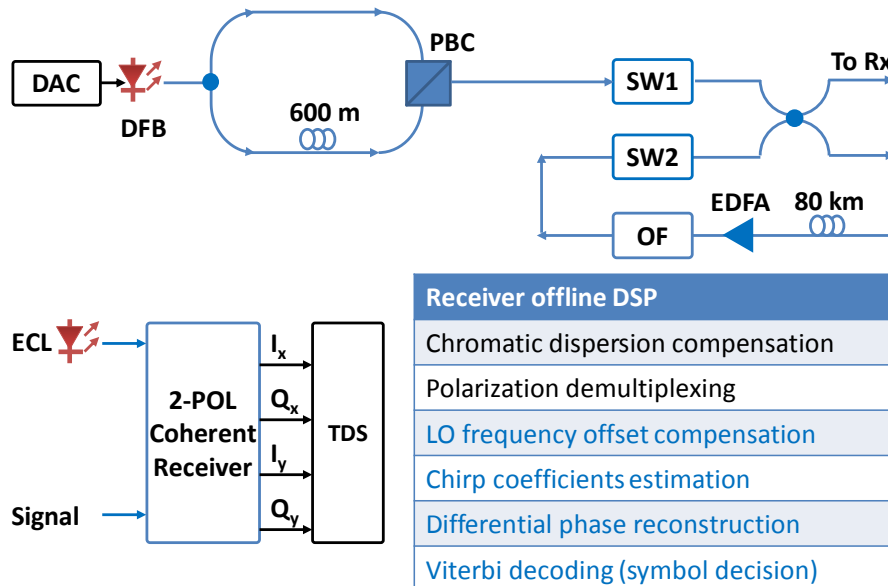


Figure 4.7 Experiment Setup. DAC: digital-to-analog converter; DFB: distributed feedback laser; PBC: polarization beam combiner; SW: optical switch; OF: optical filter; Rx: receiver; ECL: external cavity laser; I: in-phase; Q: quadrature; x/y: X/Y polarization; TDS: time-domain oscilloscope.

At receiver, an external cavity laser (ECL) with linewidth of 10 kHz serves as the local oscillator (LO). The signal and LO are fed into a DP coherent receiver, whose output is

sampled by a real-time oscilloscope at 50-GSa/s with 16-GHz bandwidth. The offline DSP includes: (1) chromatic dispersion compensation; (2) polarization demultiplexing by a 40-tap 2×2 adaptive equalizer; intensity-only decision is immediately made after this for performance comparison; (3) LO frequency offset compensation; (4) chirp coefficients estimation; (5) differential phase reconstruction; (6) MLSE and symbol decision.

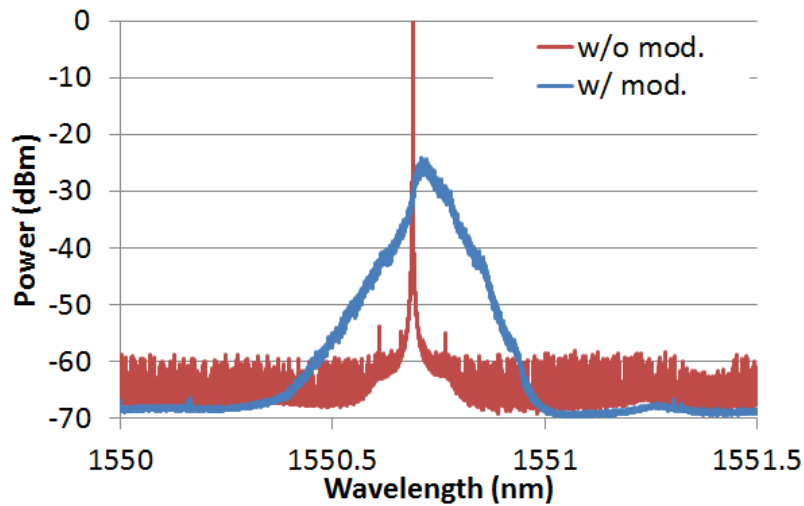


Figure 4.8 Optical spectrum of DP PAM-4 signal at transmitter end; w/o: without; w/: with; mod.: modulation.

A. DML Phase Model Verification

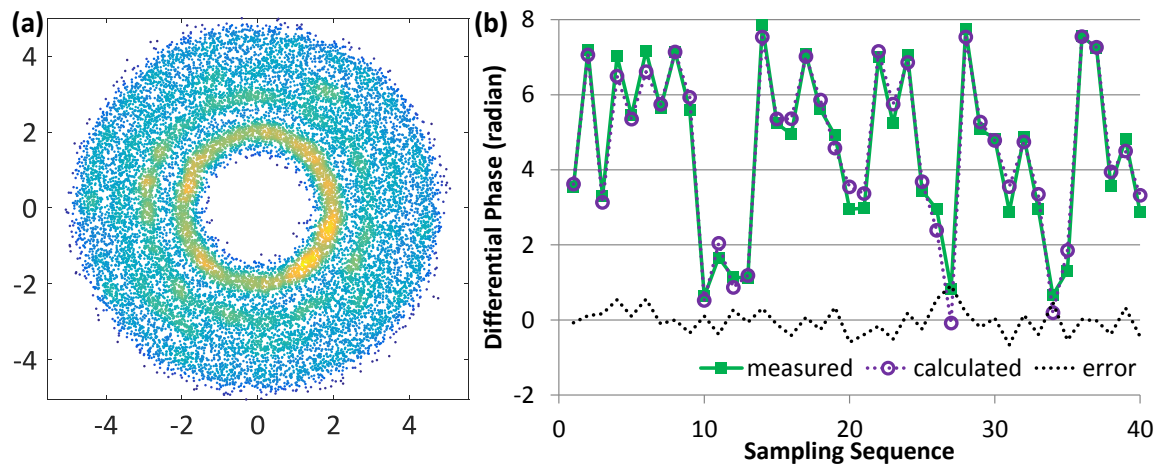


Figure 4.9 PAM-4 signal at OSNR of 24 dB: (a) constellation of X polarization; (b) Measured differential phase (Each sampling point shown at the horizontal axis corresponds to 0.1-ns).

We first verify the DML phase model to clearly reveal the feasibility of CDM. A PAM-4 constellation measured by experiment after 2×2 channel equalization is illustrated in Figure 4.9(a) at OSNR of 24 dB. We can hardly distinguish the boundaries among the 4 rings, which indicate a large BER (0.012 for this figure) for intensity-only decision. The phase of each sampling point is contaminated by laser phase noise, but the differential phase $\Delta\phi$ behaves regularly following Eq. (4-4). We compare the measured $\Delta\phi$ with the reconstructed $\Delta\phi$ using Eq. (4-4) in Figure 4.9(b) at an arbitrary time window. The two

curves coincide well, proving the validity of the theoretical phase model, which results in the decrease of BER to only 0.00014 after MLSE.

B. OSNR Sensitivity Measurement

We experimentally measure the OSNR sensitivity for DP PAM-4 system in Figure 4.10. CM achieves about 9-dB OSNR sensitivity improvement over IM for back-to-back measurement. To achieve the BER below 20% FEC threshold, CM only requires an OSNR of 12 dB for 40 Gb/s signal. Compared with previous DP PAM-4 DML-COHD experiment [34], this has about 8-dB OSNR sensitivity advantage normalized to the same data rate. The theoretical OSNR sensitivity for 10-Gbaud DP QPSK signal is about 5 dB for 10-Gbaud signal at 20% FEC threshold. CDM experiment achieves only 7 dB gap with the DP QPSK theoretical sensitivity, which coincides well with the simulation.

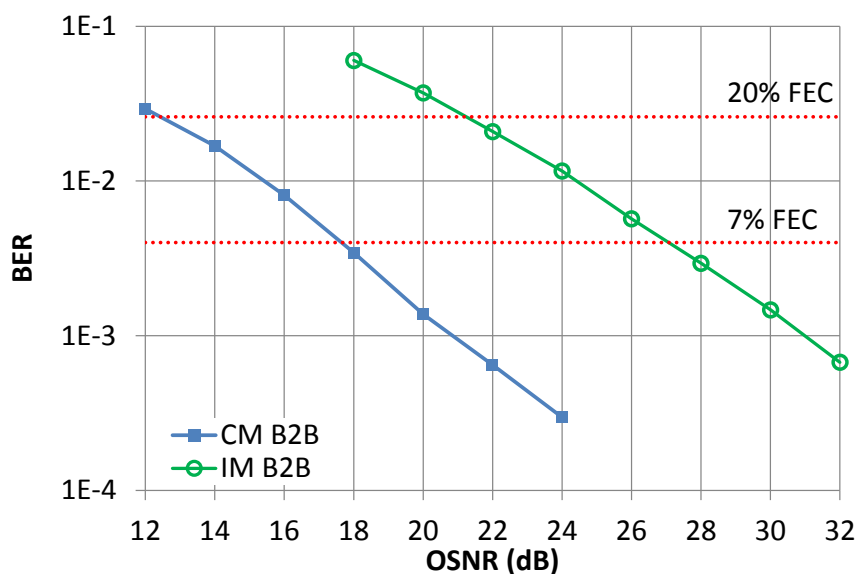


Figure 4.10 Experiment OSNR sensitivity for 40-Gb/s DP PAM-4 system. B2B: back-to-back measurement.

C. Transmission Results

Figure 4.11(a) shows the optimal fiber launch power of about -2 to 0 dBm for a 40-Gb/s CDM signal. The optimal launch power for 40-Gb/s DP QPSK signal is about -4 to -2 dB. Here, CDM shows better fiber nonlinearity tolerance compared to the standard coherent detection system. The DML frequency chirp will help improving the system resistance to fiber nonlinearity, which is an interesting topic to be further investigated in the future.

After 1200-km SSMF transmission, DP PAM-4 can still achieve a BER under 7% FEC threshold, as shown in Figure 4.11(b). The OSNR sensitivity at 7% FEC is about 3 dB worse than back-to-back measurement, due to other channel impairments such as the polarization mode dispersion and fiber nonlinearity. For distance beyond 1000 km,

which is the application range for long-haul communications, transmission performance normally becomes the dominant consideration instead of the transceiver cost-efficiency. Therefore, the distance of 1200 km is sufficient to reveal the great potentials for CDM to be applied to optical medium reach applications, to replace the commercialized QPSK transceivers. It is noted that due to the bandwidth limitation of our current DFB laser, we only use 10-Gbaud symbol rate. By using 20G or even 40G class DML [111-112], the system can readily achieve 100G per channel, and 400G or even Terabit transmission in combination with WDM.

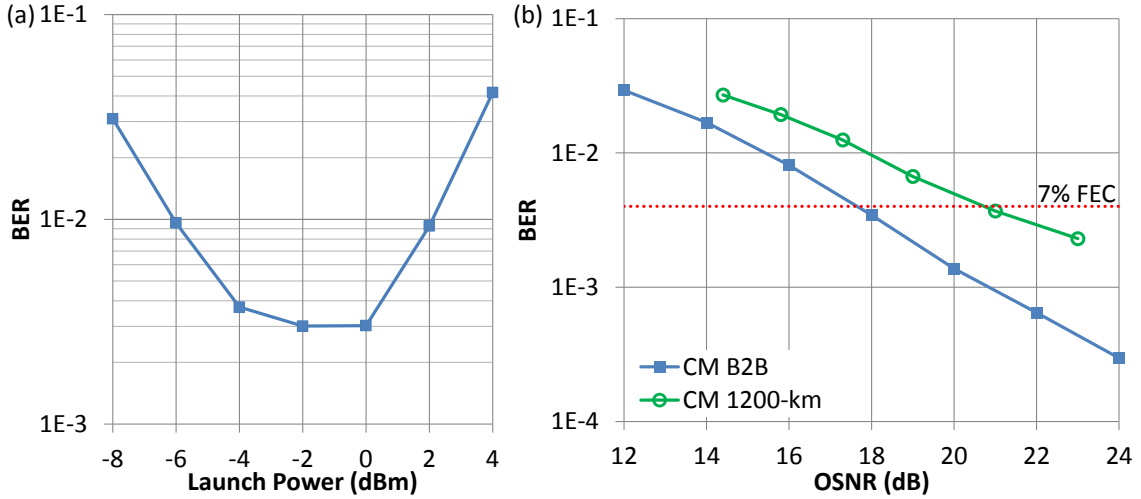


Figure 4.11 40-Gb/s DP PAM-4 transmission performance. (a) BER versus fiber launch power; (b) OSNR sensitivity. B2B: back-to-back measurement. The launch power for 1200-km transmission is 0 dBm.

4.6 Revisit MLSE: a probabilistic perspective

The CDM decoder performs 2-tap MLSE, taking the intensity I_t and differential phase $\Delta\varphi_t$ as inputs, where t is the discrete time sequences. We define two sets in section 4.3: (i) the state $\{S_t\}$ (each state corresponds to a PAM level); (ii) the transition $\{\chi_t | \chi_t \triangleq (S_t, S_{t-1})\}$. The crucial task for MLSE is to calculate the transition probability $P(I_t, \Delta\varphi_t | S_t, S_{t-1})$, in order to find the most reliable transitions. This was previously estimated by transition distance in Eq. (4-9), which is based on the discrete signal approximation of laser frequency chirp as Eq. (4-4). In fact, the adiabatic part of differential phase in Eq. (4-3) is a continuous time integral within one symbol period. To derive the $\Delta\varphi_t$ only related to the discrete states S_t and S_{t-1} , we apply the mean value theorem of integrals to Eq. (4-3) and reach Eq. (4-4). However, to use the mean values, the transmitted PAM should be rectangular pulse, so as to guarantee a flat intensity within one symbol period. This results in the conventional non-return-to-zero (NRZ) PAM pulses, which has been adopted in the PAM transmission experiment in section 4.5. Nevertheless, to realize high baud-rate within the limited laser modulation bandwidth, the PAM is preferred to be Nyquist pulses, for which the intensity cannot guarantee

itself as a constant within T . Moreover, at high baud rate, even Eq. (4-1) may become an unreliable chirp approximation.

The most reliable way of estimating $P(I_t, \Delta\varphi_t | S_t, S_{t-1})$ is to acquire the 2-D joint distribution $(I_t, \Delta\varphi_t | S_t, S_{t-1})$, so that the probability distributions can be stored in a look-up table [16,113]. To simplify the training process, we regard I_t and $\Delta\varphi_t$ as 2 independent random variables, to decompose the 2-D joint distribution into 2 1-D distributions:

$$P(I_t, \Delta\varphi_t | S_t, S_{t-1}) = P(I_t | S_t) \cdot P(\Delta\varphi_t | S_t, S_{t-1}) \quad (4-10)$$

It is assumed that the intensity channel has no ISI so that $P(I_t | S_t, S_{t-1}) = P(I_t | S_t)$. Eq. (4-10) can be calculated by logarithm to avoid multiplication. MLSE only requires 2 statistical tables for $\log P(I_t | S_t)$ and $\log P(\Delta\varphi_t | S_t, S_{t-1})$, which could be estimated and pre-stored in the memory. The sophisticated chirp model is hidden behind the statistics of $\log P(\Delta\varphi_t | S_t, S_{t-1})$. There is no need to measure any chirp related parameters, such as α , κ and transmitted PAM levels; and thus, no need to concern the inaccuracy of these coefficients, as well as the chirp model itself.

The MLSE based on the probabilistic transition estimation does require extra training processes for the statistics distributions, but it is simpler and more accurate than the digital signal approximation in Eq. (4-4); more importantly, it gets rid of the modulation limitation of NRZ pulses. This means the higher-electrical-efficiency pulse shaping can now be applied to the CDM PAM transmitter, as we revealed in the next section.

4.7 Nyquist-pulse-shaped PAM-4 transmission experiment

We demonstrate the first 100 Gb/s polarization-multiplexed PAM-4 CDM system as shown in Figure 4.12 [113]. The baseband PAM-4 signal is Nyquist-pulse shaped by a raised cosine filter with roll-off factor of 0.01. The 25-GBaud signal is resampled to the arbitrary waveform generator (AWG) sampling-rate of 92 GSa/s (In practice the oversampling rate can be less than 1.5). Two independent 1549.44-nm distributed feedback (DFB) lasers serve as the light sources of dual polarizations. Their frequency offset is less than 0.02 nm by adjusting the temperature. The 3-dB laser bandwidth is 16 GHz (12.5-GHz bandwidth would be sufficient). Their output spectra are illustrated in the Figure 4.13. The 2 outputs are polarization combined and then launched into a recirculating loop consisting of 1 span of 80-km standard single mode fiber (SSMF) and an EDFA to compensate the loop loss of 17 dB. The EDFA noise figure is 6 dB. At receiver, an external cavity laser (ECL) is applied as local oscillator (LO). The signal and LO are fed into a dual-polarization coherent receiver, whose output is sampled by a real-time oscilloscope at 80-GSa/s with 33-GHz bandwidth. The receiver offline DSP is shown by the inset (right) of Figure 4.12. The polarization demultiplexing is performed by a 40-tap

2×2 adaptive equalizer using multi-modulus algorithm (MMA); intensity-only decision is immediately made after this for performance comparison. Signal is down-sampled to the symbol rate before probabilistic transition estimation.

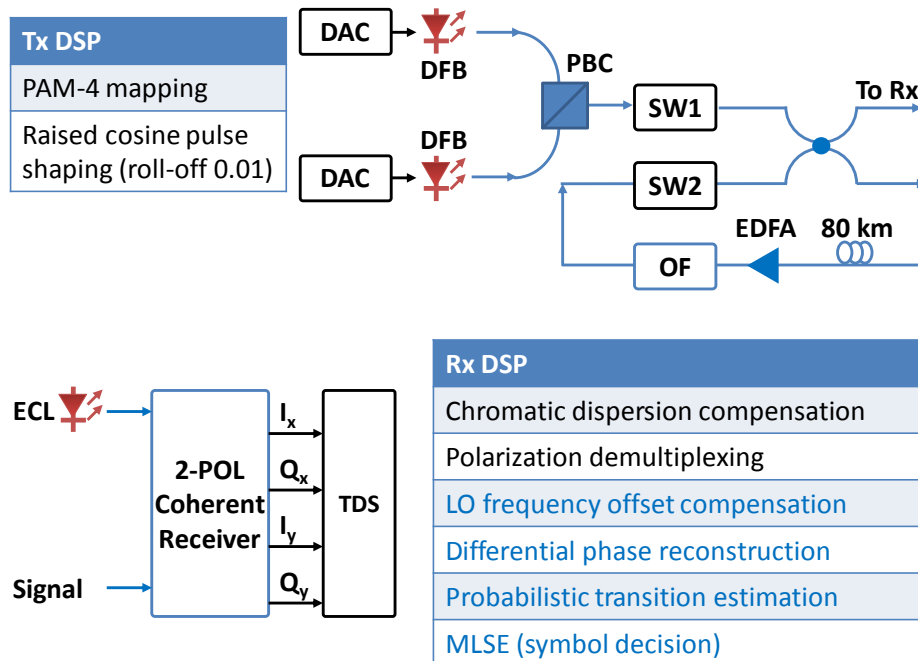


Figure 4.12 Experiment setup. DAC: digital-to-analog converter; DFB: distributed feedback laser; PBC: polarization beam combiner; SW: optical switch; OF: optical filter; ECL: external cavity laser; I/Q: in-phase/quadrature; x/y: X/Y polarization; TDS: time-domain oscilloscope.

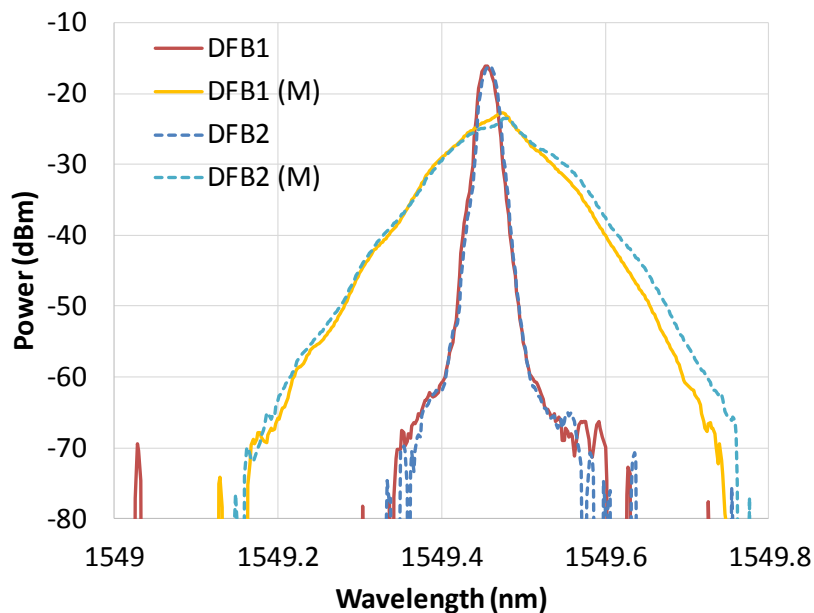


Figure 4.13 Optical spectra of the two lasers (“M” means modulation in the legend).

We first observe the measured distributions (using OSNR of 24 dB as an example). The 4 intensity distributions ($I_t|S_t$) in Figure 4.14(a) present Gaussian shapes. Because the optical signal is modulated with equal-intensity spacing while the ASE noise is added to signal field, PAM level with high intensity suffers from larger noise after the square-law

detection. Figure 4.14(b) illustrates 16 differential phase distributions ($\Delta\varphi_t|S_t, S_{t-1}$). Each curve cluster represents the statistics of the current state S_t ; within each cluster, the 4 curves stand for 4 previous states, respectively.

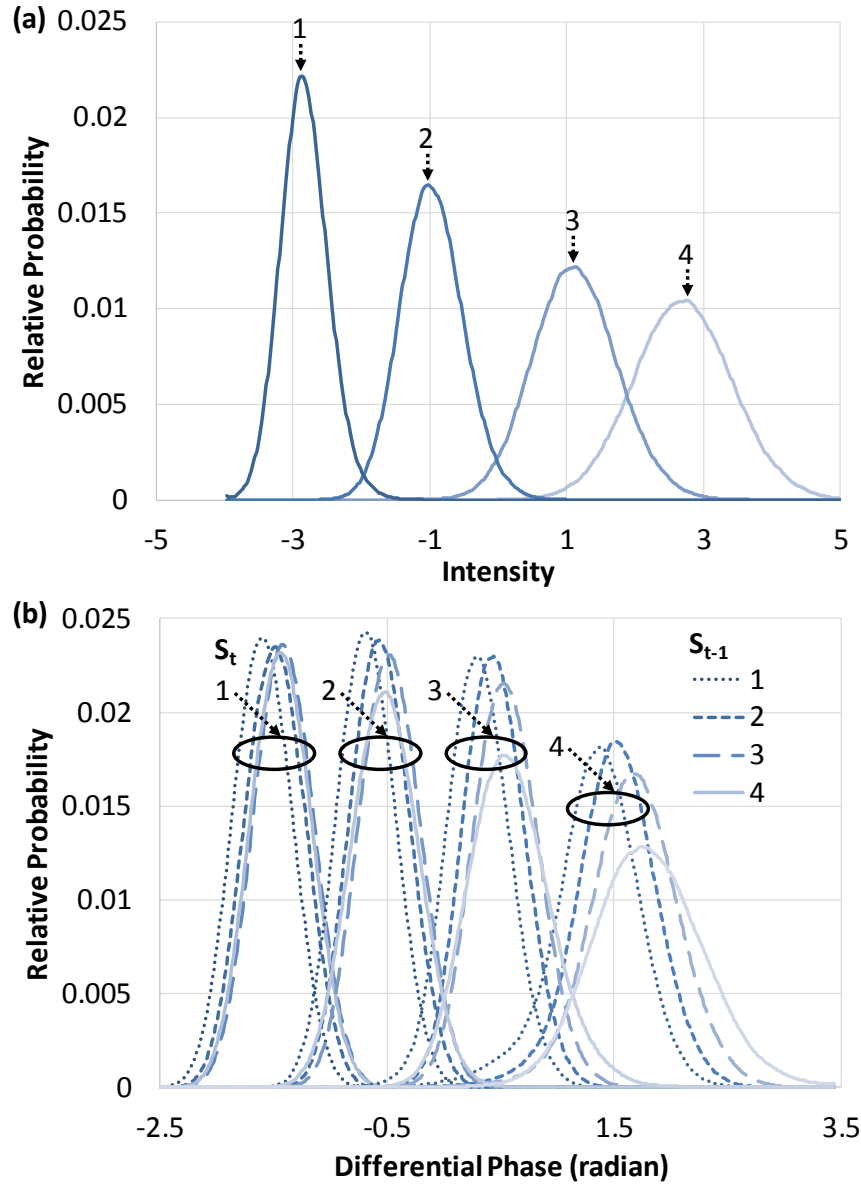


Figure 4.14 Measured probability density function of the PAM-4 (X polarization) at OSNR of 24 dB: (a) intensity and (b) differential phase.

We then evaluate the system performance. The back-to-back OSNR sensitivity is illustrated in Figure 4.15. This 100-Gb/s CDM signal requires 24-dB OSNR at 7% hard-decision FEC (HD-FEC) and 19-dB OSNR at 20% soft-decision FEC (SD-FEC) using the MLSE with probabilistic transition estimation. MLSE decoding achieves about 7 dB OSNR gain over the intensity-only hard decoding, a bit less than our previous 40-Gb/s system (9 dB). For high-baud-rate signal, the adiabatic chirp induced $\Delta\varphi$ would decrease, as indicated via Eq. (4-4), leading to the shrink of the dynamic range of differential phase. In Figure 4.14(b), the two $\Delta\varphi$ extrema have less than 3.5-radians gap (only considering the peak values). This severely degrades the MLSE decoding gain. As this is the first 100-Gb/s CDM

demonstration, we could only use the off-the-shelf lasers, which normally minimize the chirp. In the future, using the lasers with customized chirp, CDM could achieve even better OSNR sensitivity gain.

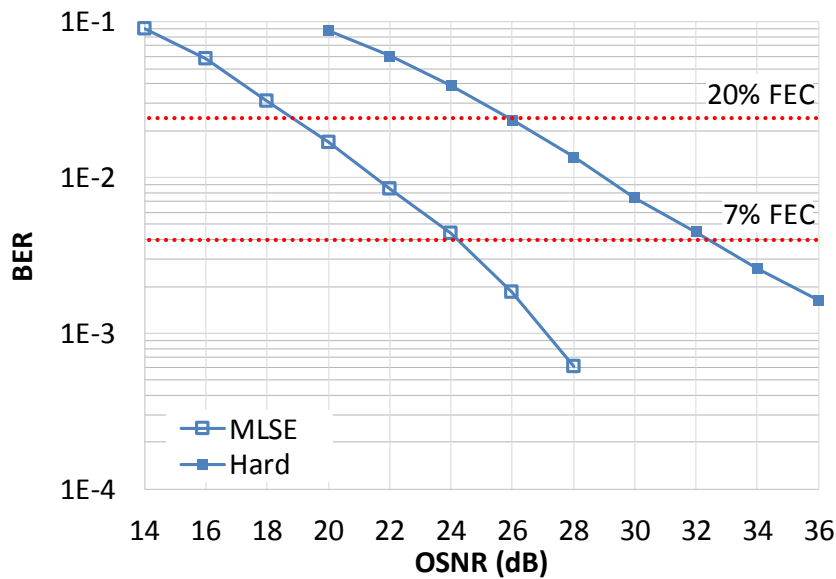


Figure 4.15 100 Gb/s polarization-multiplexed PAM-4 system OSNR sensitivity. 7%-HD/20%-SD FEC threshold: $4e-3/2.4e-2$; Hard: Intensity-only decision.

We measure the BER versus launch power after 640-km SSMF in Figure 4.16(a). The optimum launch power is 2 dBm. Figure 4.16(b) shows the BER versus SSMF distance. The hard decoding achieves <400-km reachable distance for 20% SD-FEC, like the early 100-Gb/s PAM-4 DM-COHD experiment [34]. In contrast, using MLSE, the CDM 100-Gb/s signal is error free at 0 km; the BER reaches 7% HD-FEC threshold ($4e-3$) after 640 km SSMF, 20% HD-FEC ($1.5e-2$) after 1280 km, and 20% SD-FEC ($2.4e-2$) after 1600 km.

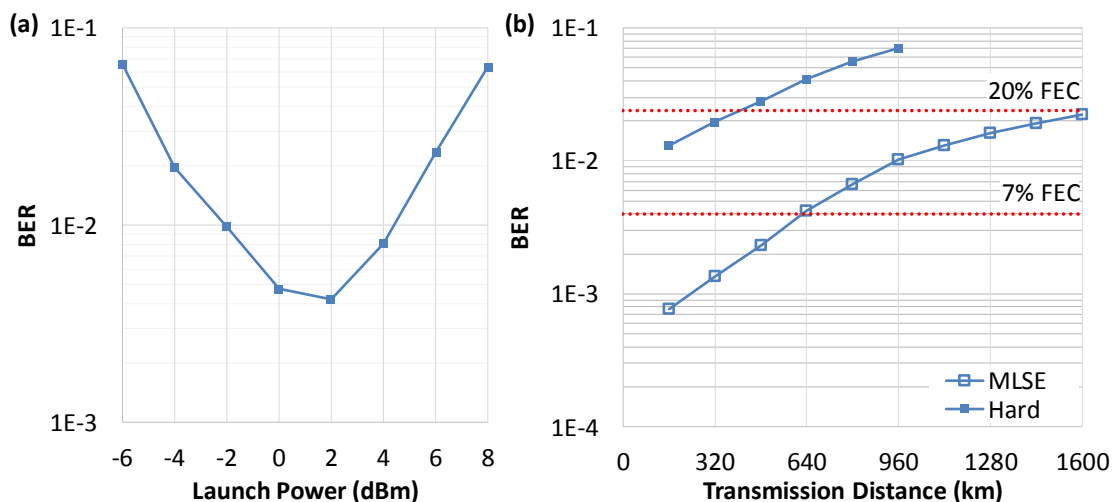


Figure 4.16 100 Gb/s polarization-multiplexed PAM-4 system: (a) BER versus fiber launch power after 640-km SSMF; (b) BER versus SSMF transmission distance. 7%-HD/20%-SD FEC threshold: $4e-3/2.4e-2$; Hard: Intensity-only decision.

4.8 Towards high order PAM utilizing large frequency chirp

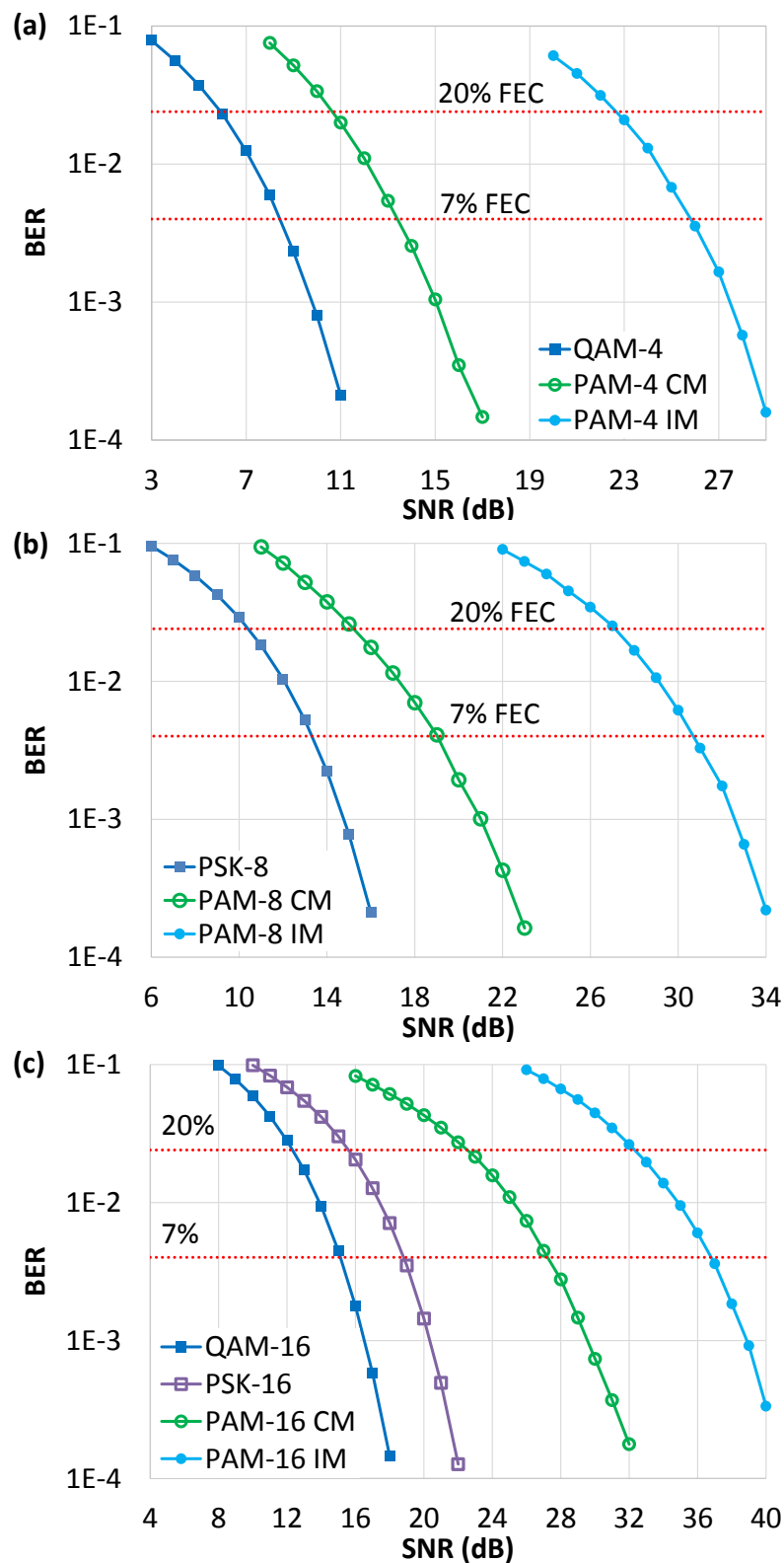


Figure 4.17 System SNR sensitivity. (a) PAM-4; (b) PAM-8; (c) PAM-16. CM: complex modulation; IM: intensity modulation.

In this section, we investigate the CDM capability of supporting higher-order modulation [98]. In contrast to the conventional IM-DML, larger frequency chirp is required to enhance the system performance. We will present by simulation the potential of CDM

to support PAM-8 or even PAM-16 modulation. The simulation setup is the same as Figure 4.4. A PAM- m signal is modelled as $[1 \ 2 \ \dots \ m]$, with a normalized power of 1. Chirp parameters are set as common values for commercial DMLs, $c_1 = 2$ and $c_2 = 1.5$. Figure 4.17(a) shows the PAM-4 system SNR sensitivity. We adopt 3.8×10^{-3} as 7% hard-decision FEC threshold; while 2.4×10^{-2} as soft-decision FEC threshold. CDM achieves more than 10-dB sensitivity gain over the conventional IM-DML. Furthermore, the sensitivity gap between CDM PAM-4 and QAM-4 shrinks to only 5-dB, converting PAM-4 to a suitable format for optical transmissions with large ASE noise, namely, longer distance with more optical amplifiers.

Maintaining the same chirp coefficients, we move to PAM-8 in Figure 4.17(b) and PAM-16 in Figure 4.17(c). For higher order modulation, the sensitivity difference gradually reduces between CDM and IM-DML. More vitally, from PAM-4 to PAM-16, CDM requires 16-dB more SNR at 7% FEC threshold; in contrast, from QAM-4 to PSK-16, the SNR increment at 7% FEC threshold is 10 dB; while from QAM-4 to QAM-16, the increment is only 6 dB.

QAM has the best SNR sensitivity, because of its better conditioned constellation distribution on the 2-D plane. In contrast, CDM suffers large sensitivity degradation when modulation order increases. Considering the CDM performance has a close relationship to the differential phase $\Delta\varphi(t)$, we inspect the $\Delta\varphi(t)$ distribution in Figure 4.18 by Eq. (4-4). Each circle in Figure 4.18 represents a power level $P(t)$ of the current sampling point, and each point represents a value of $\sqrt{P(t)} \cdot \exp(i \cdot \Delta\varphi(t))$. Figure 4.19 provides the system SNR sensitivity corresponding to the $\Delta\varphi(t)$ distribution in Figure 4.18. For PAM-4 in Figure 4.18(a), when $c_1 = 2$ and $c_2 = 1.5$, the 4 $\Delta\varphi$ values on each circle approximately distribute uniformly at $[0, 2\pi)$. The system sensitivity decreases when chirp parameters decrease, because $\Delta\varphi$ distribution does not fully utilize the 2-D space. For example, when c_1 reduces by half in Figure 4.18(b), the range of $\Delta\varphi$ shrinks to $[0, 0.5071 \cdot 2\pi)$, which corresponds to a SNR sensitivity penalty of 2 dB in Figure 4.19(a). Further increase of chirp parameters in Figure 4.19(a) does not benefit the sensitivity of PAM-4, because the $\Delta\varphi$ distribution is already close to optimum.

Maintaining $c_1 = 2$ and $c_2 = 1.5$, 8 $\Delta\varphi$ values falls within $[0, 1.0333 \cdot 2\pi)$ in Figure 4.18(c); while 16 $\Delta\varphi$ values within $[0, 1.3039 \cdot 2\pi)$ in Figure 4.18(e). MLSE decoder faces more difficult tasks to distinguish the discrete $\Delta\varphi$ values, resulting in a bad decoding performance. For high-order modulation formats beyond PAM-4, CDM requires larger chirp parameters to achieve more SNR sensitivity gain over IM-DML. In Figure 4.18(d), we double c_1 as 4 to expand the $\Delta\varphi$ range to $[0, 1.6952 \cdot 2\pi)$. As a result, the SNR sensitivity of PAM-8 system increases about 2.5 dB at 7% FEC threshold in Figure 4.19(b). The sensitivity increment is more dramatic for PAM-16. When $c_1 = 4$, $\Delta\varphi$ is expanded to $[0, 2.1864 \cdot 2\pi)$ in Figure 4.18(f). Correspondingly, the SNR sensitivity of PAM-16

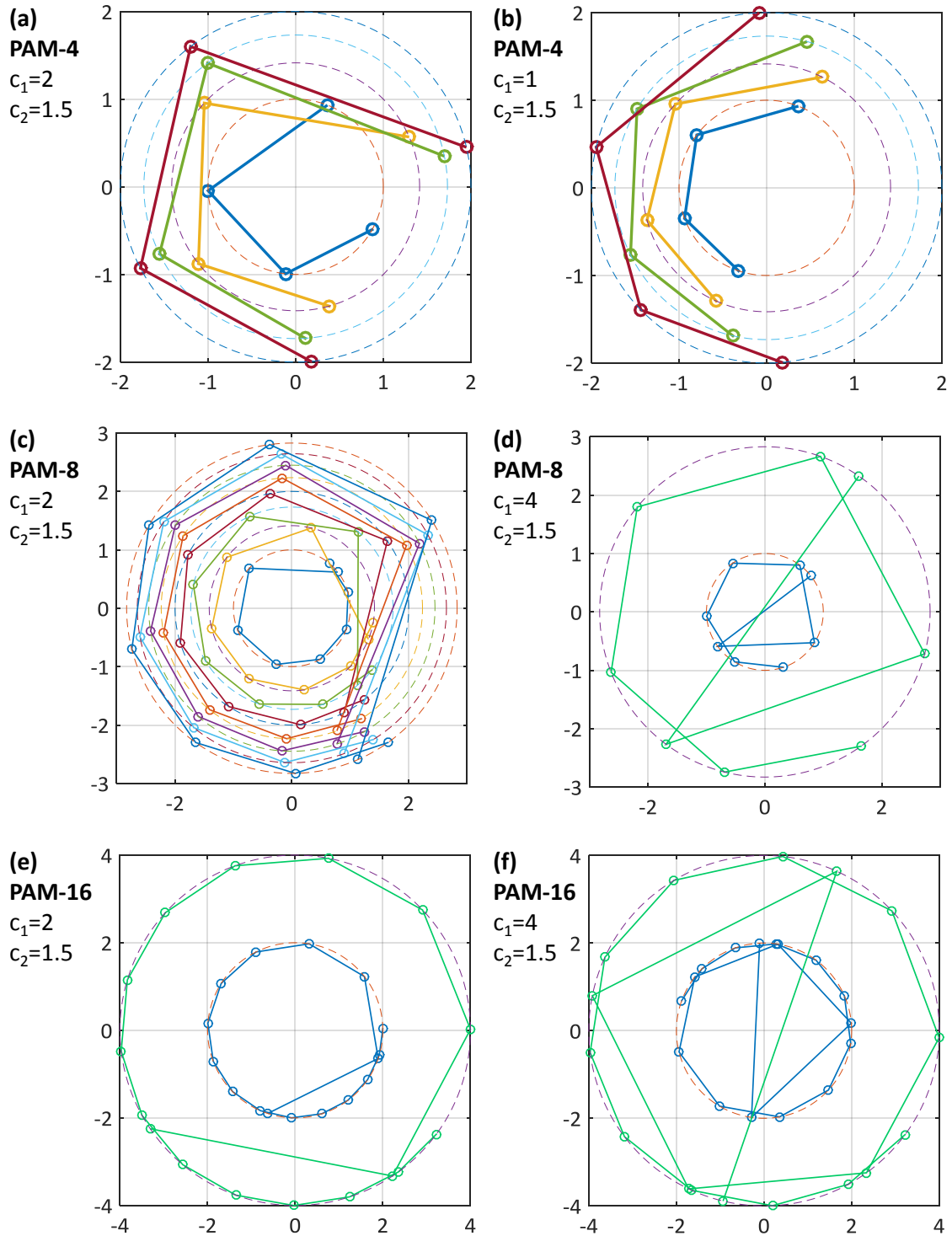


Figure 4.18 Chirp parameters impact on the differential phase distribution. Each figure shows a 2-D complex plane. Inside figures, each circle represents a power level $P(t)$ of the current sampling point, and each point represents a value of $\sqrt{P(t)} \cdot \exp(i \cdot \Delta\varphi(t))$, where $\Delta\varphi(t)$ is the differential phase between the adjacent sampling points. From (d-f), only 2 power levels are illustrated instead of 8 or 16 levels to simplify the figures.

system increases 6 dB at 7% FEC threshold in Figure 4.19(c). Similar trends exist when c_2 increases. In Figure 4.19(b), doubling c_2 results in 3 dB SNR sensitivity increment for PAM-8; while in Figure 4.19(c), doubling c_2 results in 6 dB increment for PAM-16. In practice, $c_2 = \alpha\kappa T/4$ is related to the symbol period T . Thus, for high baud-rate, c_2

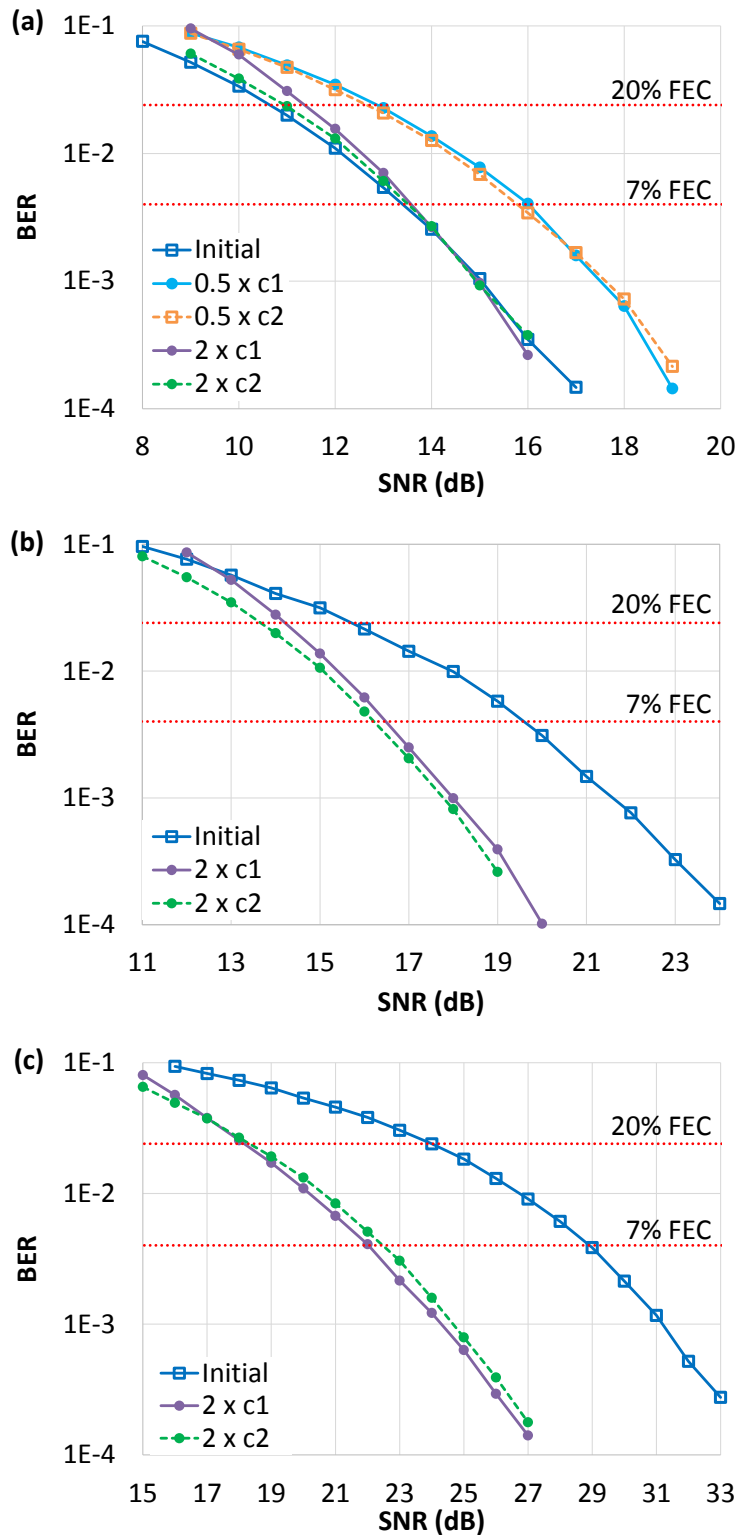


Figure 4.19 Chirp parameters impact on the system SNR sensitivity. (a) PAM-4; (b) PAM-8; (c) PAM-16. Initial (chirp coefficients): c_1 is 2 and c_2 is 1.5.

decreases, which may degrade the SNR sensitivity. However, c_1 is independent to the modulation parameters, and previous literatures [103,111] have reported some types of DML with high c_1 , which can be applied to the CDM system in the future.

It is intriguing to find that after doubling the chirp parameters, the gap between CDM enabled PAM-16 and QAM-16 has the potential to shrink to only 6 dB. This sensitivity

gap is similar to what we have achieved in PAM-4 system (compared to QAM-4). After doubling the chirp, the CDM enabled high-order PAM is promising to compete with the commercial EM based QAM transmitter in cost-sensitive medium-reach transmissions.

4.9 NRZ PAM-8 transmission experiment

We demonstrate the first CDM enabled high-order modulation beyond PAM-4, using dual polarization (DP) PAM-8 [98]. Experiment uses the same setup as that illustrated in Figure 4.7, and the same DML in NRZ PAM-4 system in Section 4.5.

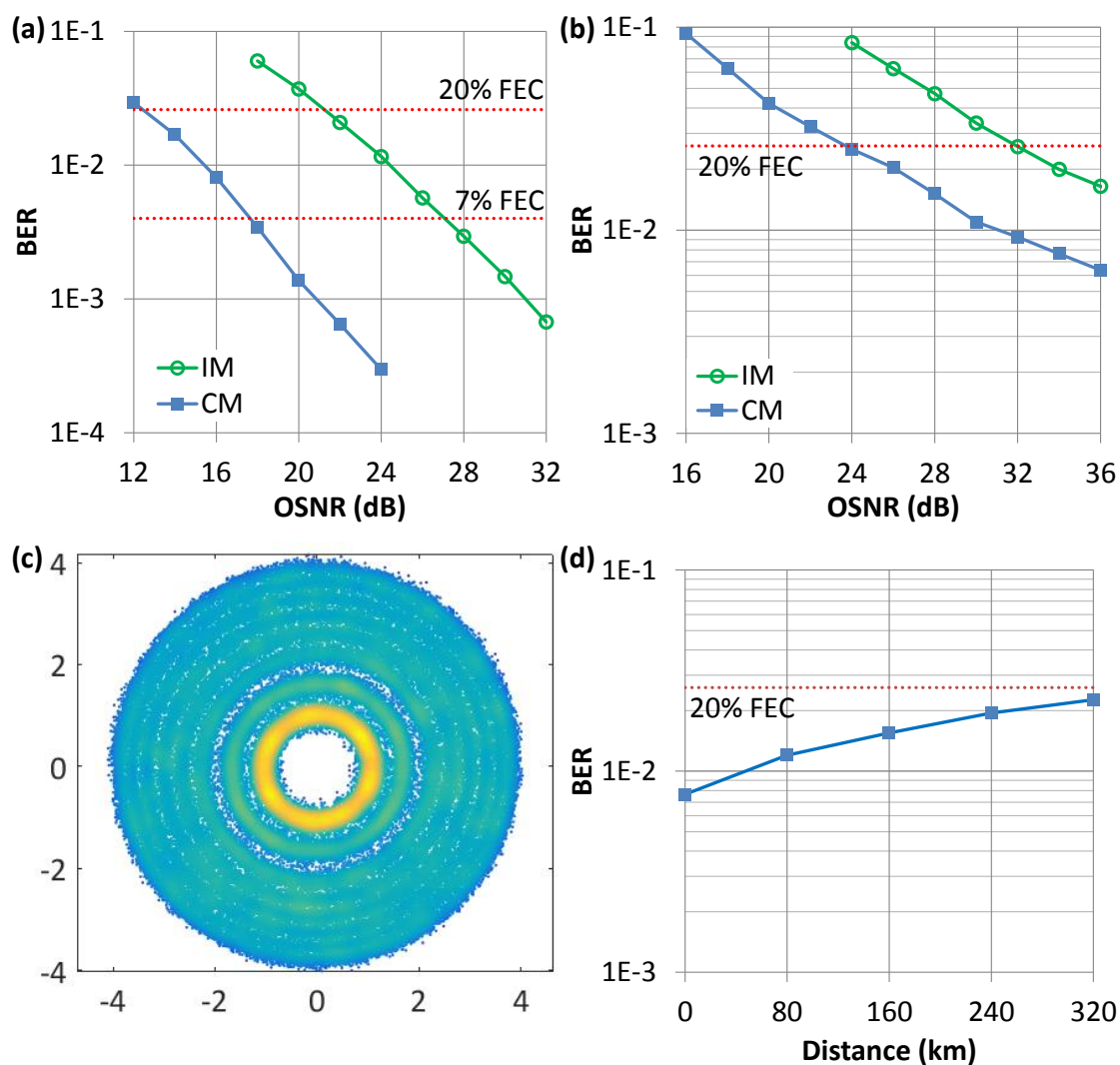


Figure 4.20 Experiment results. (a) 40-Gb/s DP PAM-4 system OSNR sensitivity. 60-Gb/s DP PAM-8 system: (b) OSNR sensitivity; (c) PAM-8 constellation after polarization demultiplexing; (d) BER versus transmission distance.

Figure 4.20(a) illustrates the optical SNR (OSNR) sensitivity for DP PAM-4 system. CDM achieves about 9-dB OSNR sensitivity improvement over IM for back-to-back measurement. To achieve bit-error-rate (BER) below 20% FEC threshold, CM only requires an OSNR of 12 dB for 40 Gb/s signal, which coincides well with the simulation results above. Figure 4.20(b) illustrates the performance of DP PAM-8 system. The gap

between CM and IM at 20% FEC is 8 dB, which is shrunk compared to PAM-4, predicted by the simulation. The required OSNR sensitivity at 20% FEC increases to 24 dB, which is because: (1) the PAM-8 intensity-only decision exhibits a BER floor, caused by the DML modulation performance limitation, and the imperfect square operation in digital domain after coherent detection; (2) the DML chirp is not sufficiently large for PAM-8; (3) the phase model is not as accurate as PAM-4 when the modulation order increases. It is noted that even when the PAM-8 constellation cannot distinguish any boundaries among the 8 rings at 36-dB OSNR in Figure 4.20(c), CM can still achieve a BER of 0.006. In Figure 4.20(d), after 320-km SSMF transmission, DP PAM-8 system can achieve a BER under 20% FEC threshold.

4.10 Conclusions

This chapter rejuvenates the classic “direct modulation” concept to the complex direct modulation (CDM), by treating the laser frequency chirp as the second modulation dimension along with the intensity. CDM significantly enhances the OSNR sensitivity of the PAM coherent system, elongates the achievable transmission distance of PAM-4 beyond 1000 km. CDM offers the cheapest 100G optical transmitter for metro transport.

This chapter contains published contents from Ref. [97] [98] [101] and [113]. The thesis author is the primary author of the publications and has contributed more than 50 per cent of the work.

5. OPTICAL SELF-COHERENT SUBSYSTEMS

Optical intensity modulation and direct detection (IM-DD) has played a major role in long-haul optical communication since 1980s. The capacity of long-haul optical transmission has increased dramatically over the ensuing decades. In early 21st century, there emerged a crucial bottleneck of the network capacity – the available optical bandwidth resource was being exhausted. It became urgent to upgrade the channel capacity per wavelength. However, the conventional IM-DD modulates the information on the optical intensity instead of the field. The fiber chromatic dispersion (CD), a linear impairment of optical field, is converted to a nonlinear effect after the intensity-only DD, which severely degrades the transmission performance [61].

The revival of coherent optical systems made a significant breakthrough [9-14,17-18,21-29,114-123] within the last decade. Instead of intensity-only modulation, coherent systems map the complex baseband signal to optical field using the external modulators. The coherent receiver linearly recovers the signal with phase diversity, and compensates the fiber impairments by the digital signal processing (DSP). The coherent technology enables the polarization multiplexing [9-10], high-order modulation format [11-12], superchannel [13-14] and space division multiplexing (SDM) [120-123] leading the long-haul transmission to a capacity leap beyond multi-Terabit/s.

In the meantime, short reach optical networks within distance of several hundred kilometers need to upgrade their capacity per wavelength beyond 40 or even 100 Gb/s to meet the ever-increasing traffic demand. Considering the commercial short-reach optical networks is dominated by the IM-DD, it faces the similar bottleneck which has emerged decades before on the long-haul transmission – the nonlinear channel response. Nevertheless, it is not practical to directly upgrade the short and medium reach applications to coherent systems, due to its cost-sensitive nature. Short and medium reach applications still favors DD as we have mentioned in section 1.5: (i) No receiver-side laser further decrease the expense; especially, it may be crucial to have a low-cost receiver without lasers for optical access applications, where the end-user is extremely cost-sensitive. (ii) The transmitter laser can be uncooled (namely, without the temperature control), because there is no need to align the wavelength between the transmitter and receiver. (iii) DD has larger linewidth tolerance for transmitter laser, while the carrier phase recovery is normally avoidable at receiver. (iv) DD is compatible with single polarization configuration, where the MIMO polarization demultiplexing is not an essential task at receiver.

A variety of DD solutions have been proposed [124-134] to extend the transmission reach of short and medium reach applications while realize high order modulation. For example, dispersion pre-compensation [54-55] alleviates the performance degradation

from CD, but the transmitter needs the I/Q modulation and much higher sampling rate than the signal baud rate. The discrete multi-tone (DMT) [124] is capable of bit and power loading depending on the channel frequency response, but is much complicated in need of feedback, and becomes inefficient when the product of baud rate and distance is large (>1000 Gbaud·km). More importantly, none of the above solutions touch the fundamental barrier – the nonlinear direct detection channel, namely, they cannot achieve a substantial improvement for the optical DD subsystems. In this chapter, we first elucidate how self-coherent (SCOH) [62,67,69-71,125-134] subsystems linearize the DD channel, and then presents a variety of SCOH schemes. The basic concept of SCOH is that the transmitter sends a carrier (C) along with the signal (S); the receiver recovers the product $S \cdot C^*$ which is a linear term of signal field, instead of the $|S|^2$ in conventional IM-DD. The chapter follows the logic frame in Ref. [62].

5.1 Why channel linearization?

We assume a baseband signal of $S_0(t)$. The complex modulation (CM) maps $S_0(t)$ linearly to the optical field $S_1^{CM}(t) = \alpha S_0(t)$; while the intensity modulation (IM) maps $S_0(t)$ to optical intensity, leading to a field signal as:

$$S_1^{IM}(t) = \sqrt{S_0(t)} \cdot \exp(i\varphi(t)) \quad (5-1)$$

where $\varphi(t)$ is the phase appended during modulation. Supposing the fiber channel impulse response is $h(t)$, the field signal after fiber transmission will be:

$$S_2(t) = S_1(t) \otimes h(t) \quad (5-2)$$

where \otimes stands for the convolution. The coherent receiver recovers an optical field, which is a linear replica of $S_2(t)$:

$$S_3^{CM} = \beta \cdot (\alpha S_0(t) \otimes h(t)) \quad (5-3)$$

where α and β are the linear coefficients. Therefore, a linear equalizer can be applied to estimate $h(t)$ and rewind the channel distortion, which ideally recover the information contained in $S_0(t)$. However, direct detection receiver recovers an optical intensity signal $S_3(t)$:

$$S_3^{IM}(t) = \left| \left(\sqrt{S_0(t)} \cdot \exp(i\varphi(t)) \right) \otimes h(t) \right|^2 \quad (5-4)$$

If $h(t) = \delta(t)$, where $\delta(t)$ is the delta function, $S_3^{IM}(t)$ can ideally represents the information encoded in $S_0(t)$. However, the impulse response of fiber channel is not a delta function, because it is always frequency dependent. Direct detection receiver never knows what fiber channel has done to the original baseband signal, namely, it cannot estimate $h(t)$; thus, it can only recover a baseband signal with distortion.

5.2 Self-Coherent Modulation and Detection

Coherent detection provides a perfect solution to the above limitation: linearization of the channel via reconstruction of the phase diverse signal at receiver, followed by DSP enabled channel equalization. The coherent receiver (Figure 2.3(b)) takes two inputs: the optical signal (S) and the optical carrier (C) from the local oscillator (LO). The output is the product of $S \cdot C^*$. Since C is a constant, the receiver recovers the linear replica of field signal.

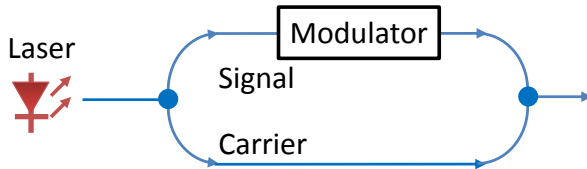


Figure 5.1 Structure of a typical self-coherent transmitter.

Direct detection (DD) subsystems do not have the LO. To imitate a channel model like the coherent detection, the carrier can be added at transmitter, shown by Figure 5.1. The transmitted signal then becomes $S + C$. The photo-detection at receiver performs a square-law function

$$I = |S + C|^2 = |S|^2 + 2\text{Re}(SC^*) + |C|^2 \quad (5-5)$$

Instead of recovering the signal power $|S|^2$, we extract the linear term of the signal $S \cdot C^*$ for the signal de-modulation. In this case, the DD channel becomes linear to the optical field. We name this category of detection scheme as self-coherent (SCOH) because the receiver utilizes a “coherent” carrier to recover the signal and the carrier comes with the signal itself before the fiber transmission. SCOH always utilizes field modulation instead of intensity modulation, because the receiver recovers the field.

SCOH avoids the carrier recovery in DSP, which is essential for the coherent system. By using the same laser to generate signal and carrier, the frequency offset between them is zero. By keeping the length of signal and carrier paths as the same, S and C contains the same laser phase noise at the transmitted end. When multiplying the S and the conjugate of C at receiver, phase noise can be fully cancelled (despite the channel impact on phase noise). The DSP of SCOH is thus greatly simplified.

The main limitations of the SCOH are depicted from Eq. (5-5): (1) SCOH can only recover the in-phase part of the signal, which leads to a low spectral efficiency. (This is also the limitation of conventional IM-DD.) (2) The linear signal is mixed with the 2nd order term $|S|^2$, namely, the signal-to-signal beat noise (SSBN) [127,130,134]. While SCOH avoids the CD induced channel nonlinearity presented in IM-DD, it brings another kind of nonlinear distortion – SSBN. The simplest method to decrease the SSBN is to enlarge the carrier to signal power ratio (CSPR) at transmitter to guarantee the power of $S \cdot C^*$ is

much stronger than that of $|S|^2$. We will show in the sections below how the SCOH schemes alleviate or even eliminate these problems.

It is noted here that the term SCOH is also used for DD schemes with differential phase shift-keying modulation (DPSK-SCOH) [66]. We briefly introduce their principle here to reveal the difference. DPSK-SCOH has a standard coherent receiver as Figure 2.3(b), which have two inputs: the signal $s(t)$ and the signal delayed by one symbol period $s(t - 1)$. The output is $s(t) \cdot s(t - 1)^*$, namely, the signal is self-coherent with its own delay. The receiver thus can reconstruct the differential phase. Considering the DPSK-SCOH has been studied in the pioneer literature [66] and has a nonlinear channel response, in this chapter we only focus on the SCOH with linearized channel.

5.3 Intensity Only 1-Dimension Direct Detection

The SCOH receiver only recovers the real part of the signal. Nevertheless, we can follow the “heterodyne detection” idea in coherent detection to send and receive a complex signal. We rewrite Eq. (5-5), and replace the C with $A_0 e^{i\omega_0 t}$ (ω_0 is the frequency of LO), S by the $A_k e^{i\omega_k t}$ (this is a single frequency signal and $f = \omega_k$).

$$I = |S + C|^2 = |A_0|^2 + |A_k|^2 + A_0 A_k (e^{i(\omega_0 - \omega_k)t} + e^{i(\omega_k - \omega_0)t}) \quad (5-6)$$

The 3rd term of Eq. (5-6) indicates that a single frequency signal would generate a pair of mirror signals after the SCOH receiver. If we send a signal which guarantees that any frequency component $\omega_k - \omega_0 > 0$ (or < 0), namely, a single sideband (SSB) signal, the mirror signals would not overlap with each other in spectrum. Meanwhile, the receiver recovers the signal with phase diversity after filtering out the mirror frequency band.

A. Generation of Single sideband (SSB) optical signal

We review two methods to generate an optical SSB signal. In Figure 5.2(a) [125], the baseband signal is first up-converted with an electrical IQ mixer; the output drives a Mach-Zehnder modulator (MZM) which is biased off the null point to provide an optical carrier. The subsequent optical filter selects one sideband. A frequency gap between the signal (S) and the carrier (C) should be reserved for the filter roll-off. In Figure 5.2(b) [127], an RF tone is inserted at the edge of the baseband spectrum; then the baseband signal is transmitted along with the RF tone to a complex signal by the IFFT; the real and imaginary parts of the signal drive an optical I/Q modulator biased at the null point. The original optical carrier is thus suppressed, and the new optical carrier is provided by the RF tone located at the edge of signal spectrum. This method was named virtual SSB [127],

because in fact the I/Q modulator generates a double sideband (DSB) modulation, but in optical spectrum the signal locates at one side of the carrier (the RF tone).

SSB signal wastes half of the electrical spectral efficiency. In cost-sensitive short and medium reach applications, RF components with much narrow bandwidth requirement are preferred. In early literatures, the above SSB approaches were applied to OFDM system only, because OFDM signal has a “rectangular” spectrum, which occupies narrower frequency span compared with the single-carrier signal with the same baud rate. Using the Nyquist pulse shaping, single-carrier transmitter can also generate a tight spectrum [117]. Therefore, these approaches can be easily extended to single-carrier modulation [134].

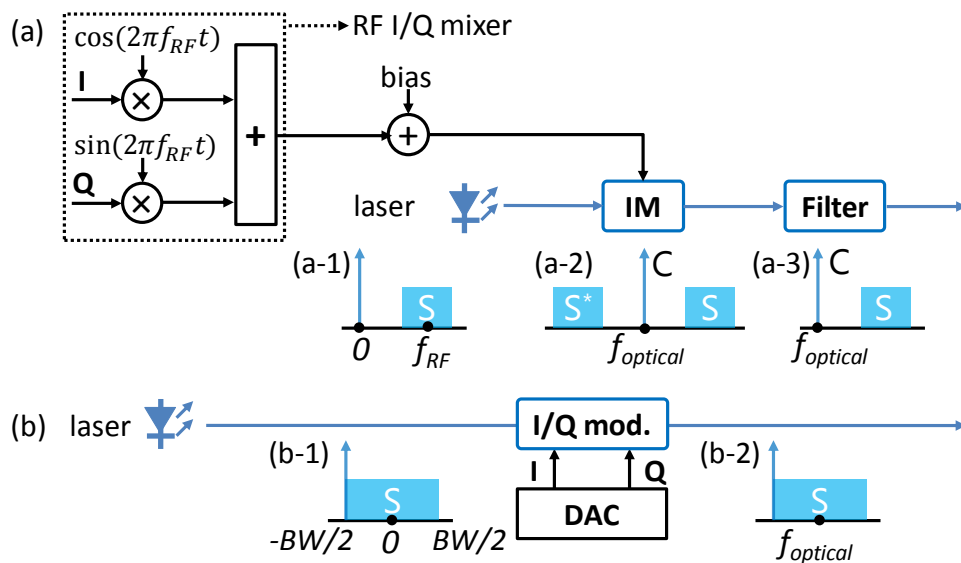


Figure 5.2 Transmitter structure for the optical single sideband (SSB) signal generation. (a) Offset SSB; spectrum (a-1) after RF I/Q mixer, (a-2) after optical intensity modulator, (a-3) after optical filter; (b) Virtual SSB; spectrum (b-1) RF domain, (b-2) optical domain. S: signal; C: carrier.

B. SSBN cancellation

The SCOH receiver recovers the pair of mirror signals, converts it into frequency domain by FFT, and digitally filters out one sideband. Then, the challenge is to distinguish the linear signal term $S \cdot C^*$ from the SSBN. One approach is to separate the signal and the SSBN in the frequency domain [125] (Figure 5.3(a)) by leaving a frequency gap between the optical carrier and the signal spectrum. The beat component of the frequency ω_i and ω_j is located at the frequency $\pm(\omega_i - \omega_j)$. Therefore, as long as the gap bandwidth is larger than the signal, the signal is free from the SSBN in frequency domain, which can be purely filtered digitally. The frequency gap further decreases the spectral efficiency. To avoid this, virtual SSB allocate the carrier close to the signal spectrum without frequency gap. To subtract the SSBN from signal, an iterative SSBN estimation and cancellation technique is introduced at receiver via DSP [127]. The algorithm (Figure

5.3(b)) first conducts symbol decision with the interference of SSBN; then uses the symbols to reconstruct SSBN, and subtracts it from the received signal. The symbol decision can be accurate after several iterations. This SSBN cancellation algorithm only fits for the OFDM modulation, and the computational complexity is much increased because it contains several FFT/IFFT pairs. However, this algorithm still indicates the great capability of the DSP enabled SCOH receiver to compensate the optical hardware imperfection.

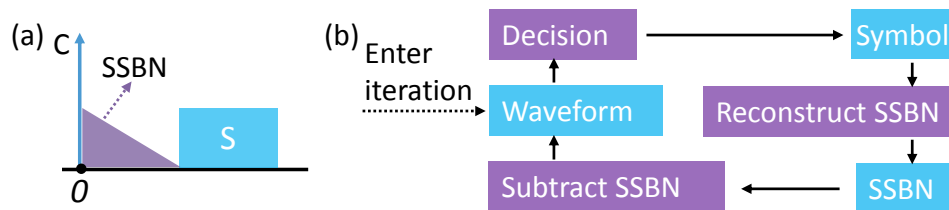


Figure 5.3 SSBN cancellation schemes. (a) Leaving frequency gap between the signal (S) and carrier (C); (b) iterative SSBN cancellation algorithm.

C. Virtual 2-D detection with time redundancy

By using the time domain redundancy, the SCOH receiver with single-ended photo-detector can also recover a DSB signal with both the in-phase and quadrature parts (2-dimension detection) [130]. The scheme was named block-wise phase switching (BPS). The BPS transmitter sends two consecutive time-domain complex signal blocks: S and iS , where i stands for a 90-degree phase shift. The carrier (C) beat with these two blocks following the Eq. (5-5) and

$$I = |S + iC|^2 = |S|^2 + 2\text{Im}(SC^*) + |C|^2 \quad (5-7)$$

By combining the real and imaginary part of $S \cdot C^*$, a complex signal is fully reconstructed. BPS needs the similar SSBN cancellation algorithm as the VSSB.

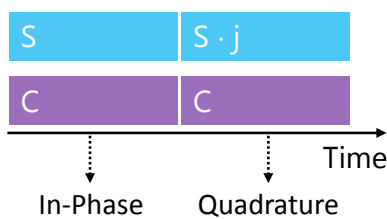


Figure 5.4 Principle of block-wise phase switching transmitter.

5.4 Phase Diverse 2-Dimension Direct Detection

The BPS recovers both the in-phase and quadrature parts of the signal, but follows the idea like time-division multiplexing (TDM). This sacrifices 50% spectral efficiency (SE). In order to recover the I and Q components simultaneously (namely, the receiver conducts 2-dimension detection), SCOH should be equipped with the coherent receiver (Figure

2.3(b)). Coherent receiver based SCOH provides the following advantages at the cost of system hardware complexity: (i) phase diverse signals can be recovered; (ii) the SSBN can be eliminated spontaneously by the balanced photo-detector (PD); (iii) the signal can be DSB modulated which greatly increases the electrical spectral efficiency. The fundamental principle of SCOH enabling coherent-like detection without an LO is straightforward: (i) transmitter sends the carrier (C) along with the signal (S); (ii) the receiver should have its unique method to separate the signal and carrier, which serve as the two inputs of the standard coherent receiver.

The crucial technical challenge is how to separate the signal and carrier. Here we introduce two typical methods which separate them in frequency and time domain, respectively.

A. Separating signal and carrier in frequency domain

The conventional I/Q modulation generates a DSB signal without the carrier (because the modulator is biased at null point). The SCOH transmitter adds a carrier at the center of the signal spectrum. The receiver separates the S and C using a narrow bandwidth optical filter [131]. A frequency gap needs to be reserved between the S and C for the filter passband. In practice, the laser for short reach applications may have a frequency drift of the order of 10 GHz. As the result, the filter should satisfy the following requirements: (i) a narrow passband to maximize SE; (ii) a wide tunable range to adapt the wavelength drift at transmitter. These greatly increase the filter expense. More importantly, the tunable filter changes the SCOH receiver from a colorless one to a colored one, which becomes sensitive to the transmitter wavelength drift. Therefore, the scheme has a huge system cost while still wastes SE conspicuously. This system can be easily extended to a polarization multiplexing version by sending a polarization diversity S and C . Both the transmitter and receiver expense approach the coherent detection, except the local oscillator.

B. Separating signal and carrier in time domain

The signal carrier interleaved (SCI) direct detection [67,132] avoid the above problem by separating the S and C in time domain. Each signal block is followed by one carrier block at transmitter (Figure 5.5(a)) [67]. The receiver structure is the same as we mentioned in section 2.2 for the DPSK-SCOH. The coherent receiver takes two inputs: the signal $s(t)$ and the signal delayed by one symbol period $s(t - 1)$. The output is $s(t) \cdot s(t - 1)^*$. Different from the previous DPSK-SCOH, $s(t - 1)$ is a constant carrier instead of the signal, therefore, the coherent receiver recovers the linear replica of the signal, instead of only the differential phase information.

This scheme also sacrifices half of the SE. To improve it, the transmitter can send a carrier block following by two consecutive signal blocks (Figure 5.5(b)) [132]. After the one-block delay at receiver, each carrier block can be used twice. The SE sacrifice decreases to one third.

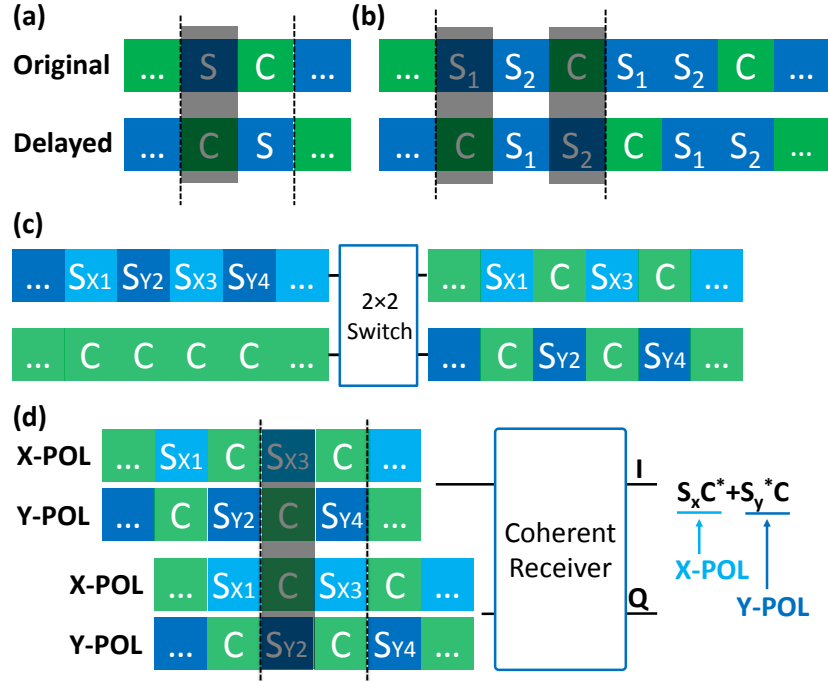


Figure 5.5 Time-domain blocks illustration for SCI-DD. (a) 1/2 spectral efficiency; (b) 2/3 spectral efficiency; 100% spectral efficiency: (c) transmitter structure; (d) receiver structure. The spectral efficiency is referred to the single-polarization coherent detection system.

We also propose here a novel SCI method to fully utilize the time domain efficiency [133], by using the polarization diverse transmitter. We first continuously modulate a DSB signal by the I/Q modulator in Figure 5.5(c). To insert the carrier blocks into the signal stream, a 2×2 optical switch is applied whose switch period is set to be one block length. The signal and the continuous laser output serve as the two inputs of the switch. The signal blocks are distributed to the two outputs of the switch periodically, during which the carrier blocks are interleaved with them, as shown by the right side in Figure 5.5(c). Then a polarization beam combiner (PBC) combines these two output streams to dual polarization (DP) SCI signal. Since the photo-detectors only allow the light in the same polarization state beating with each other, the output of the balance receiver is the sum of beat results from the two polarizations. We take the shaded time slot in Figure 5.5(d) as an example. For X-POL, signal block S_x and carrier block C enter the balance receiver. The output is $S_x C^*$. Meanwhile, for Y-POL, the output is $S_y^* C$ because S and C exchange their entrances into the receiver. Therefore, the combined output becomes $S_x C^* + S_y^* C$. Maximum likelihood sequence estimation (MLSE) can be applied to this channel with 2-tap memory to recover the signal stream [53,106]. This subsystem achieves 100% SE compared with single-polarization coherent detection.

5.5 Discrete-time Gaussian Channel with Conjugate Intersymbol Interference

We further analyze the channel characteristics of the DP-SCI-DD channel in this section. Considering the received signal in the n -th time block, the current signal S_n is mixed with the signal in the last time block S_{n-1} after the DP-SCI-DD receiver. Assuming the signal before entering the receiver goes through the additive white Gaussian noise (AWGN) optical channel, the signal after the receiver goes through a discrete-time Gaussian channel with intersymbol interference (DTGC-ISI) [135]. DTGC-ISI can be modeled as:

$$y_k = \sum_{i=0}^M h_i x_{k-i} + w_k, \quad -\infty < k < \infty \quad (5-8)$$

where $\{x_k\}$ and $\{y_k\}$ are the input and output sequences respectively, the finite-length sequence $\{h_i\}$ with $h_0 \neq 0$ and $h_M \neq 0$ is the unit-sample response of the equivalent channel filter. The noise samples w_k are independent identically distributed (i.i.d) Gaussian random variables with mean zero and variance $N_0/2$.

Nevertheless, the channel model of the DP-SCI-DD is slightly different from the general DTGC-ISI with the below two unique characteristics: (i) the ISI is derived from the conjugate of the signal in the last time block (S_{n-1}^*) instead of the S_{n-1} itself; and (ii) the additive noise comes from both the last and the current time block, which is $w_k + w_{k-1}^*$ instead of w_k . Therefore, we name this channel as DTGC with conjugate ISI (DTGC-CISI) [133]. The channel model is modified as:

$$y_k = h_0 x_k + h_1^* x_{k-1}^* + w_k + w_{k-1}^*, \quad -\infty < k < \infty \quad (5-9)$$

We define the noise at time k as n_k ($n_k = w_k + w_{k-1}^*$). The correlation between n_{k+1} and n_k can be calculated by:

$$\begin{aligned} \text{Corr}(n_{k+1}, n_k) &= \frac{4}{N_0^2} E[n_{k+1}^* n_k] \\ &= \frac{4}{N_0^2} E[(w_{k+1} + w_k^*)^* (w_k + w_{k-1}^*)] = \frac{4}{N_0^2} E[w_k \cdot w_k] = 0 \end{aligned} \quad (5-10)$$

Therefore, different noise samples n_k , are independent and identically distributed Gaussian random variables with mean of zero and variance of $\sigma_n^2 = 2\sigma_w^2 = N_0$. The channel model is further simplified as:

$$y_k = h_0 x_k + h_1^* x_{k-1}^* + n_k, \quad -\infty < k < \infty \quad (5-11)$$

Even though DTGC-CISI has channel memory, the noise is memory-less. Noting that x_{k-1} and x_k come from different sampling time, there is a phase difference φ between them induced by the laser phase noise. For large linewidth laser, the channel of the DP-SCI-DD can be expressed as:

$$y_k = h_0 x_k + h_1^* x_{k-1}^* e^{i\varphi} + n_k, \quad -\infty < k < \infty \quad (5-12)$$

Eq. (5-11) reveals that the discrete received signals follow the Markov process, in the sense that the probability of being in state x_{k+1} at time $k + 1$, given all states up to time k , depends only on the state x_k at time k :

$$P(x_{k+1} | x_0, x_1, \dots, x_k) = P(x_{k+1} | x_k) \quad (5-13)$$

Therefore, we implement the Viterbi algorithm (VA) [106] for the channel described by Eq. (5-11). We define two sets for the VA model in DTGC-CISI: (i) the state $\{x_k\}$; (ii) the transition $\{\chi_k | \chi_k \triangleq (x_{k+1}, x_k)\}$. Each state corresponds to a constellation point of the modulation. The transition is a state pair containing the states at the adjacent sampling points. The transition probability $P(x_{k+1} | x_k)$ characterizes the possibility of the transition, while in our implementation we substitute it by the transition distance:

$$\lambda(\chi_k) = y_{k+1} - (h_0 x_{k+1} + h_1^* x_k^*) \quad (5-14)$$

The larger the distance is, the smaller the probability $P(x_{k+1} | x_k)$ is, namely, the transition has less possibility to be existed. For each time k , we define the survivor $\hat{\mathbf{s}}(x_k)$, which contains all the transitions from x_1 to x_k with the smallest sum of transition distance; and define the survivor length $\mathbf{\Gamma}(x_k)$, which stores the sum of the transition distance. The following algorithm describes the VA procedure:

Storage

The following variables need to be stored and updated at every step of decoding:

k : time index;

$\hat{\mathbf{s}}(x_k), 1 \leq x_k \leq M$: Survivor terminating at y_k ;

$\mathbf{\Gamma}(x_k), 1 \leq x_k \leq M$: Survivor length.

Initialization

$k = 0$;

$\hat{\mathbf{s}}(x_1) = x_1$;

$\mathbf{\Gamma}(x_1) = 0$.

Iteration

For each state at time $k + 1$, compute $\mathbf{\Gamma}(x_{k+1}, x_k) = \mathbf{\Gamma}(x_k) + \lambda(\chi_k)$ for all the $\chi_k = (x_{k+1}, x_k)$ and find $\mathbf{\Gamma}(x_{k+1}) = \min_{x_k} \mathbf{\Gamma}(x_{k+1}, x_k)$; add the x_k to the survivor and update the survivor length.

Assuming the final sampling point is x_N with a known state, the survivor sequence that terminates at x_N is the decoded sequence.

A 100-Gb/s DP-SCI-DD simulation is performed to evaluate DTGC-ISI model [132]. The parameters are: RF signal is modulated by 16-QAM OFDM. FFT size for OFDM is 128 with 80 subcarriers filled with data. The DAC sampling rate is 40 GSa/s, corresponding to an

optical bandwidth of 25 GHz. The ADC sampling rate is 80 GSa/s. The BER as the function of OSNR is shown in Figure 5.6. We use the polarization multiplexed coherent detection (POL-MUX-CO) as a benchmark for comparison with the same data rate of 100 Gb/s. At the 7% FEC threshold, DP-SCI-DD exhibits an OSNR penalty of about 8.4 dB compared with coherent detection in terms of back-to-back measurement, which can be explained as follows: (i) the carrier in DP-SCI-DD shares half of the power at the transmitter end when the CSNR is 0 dB, providing 3 dB sensitivity penalty; (ii) not only the signal, the carrier in DD also suffers from the channel noise, providing another 3 dB degradation; (iii) DTGC-CISI with the VA provides 2.4 dB penalty from the presence of conjugate interference. DP-SCI-DD with 100 km transmission is also simulated. The results indicate less than 0.5 dB penalty for 100 km transmission compared to the back-to-back system, which signifies the tolerance of the proposed DD scheme to chromatic dispersion, nonlinear channel impairments in short reach applications.

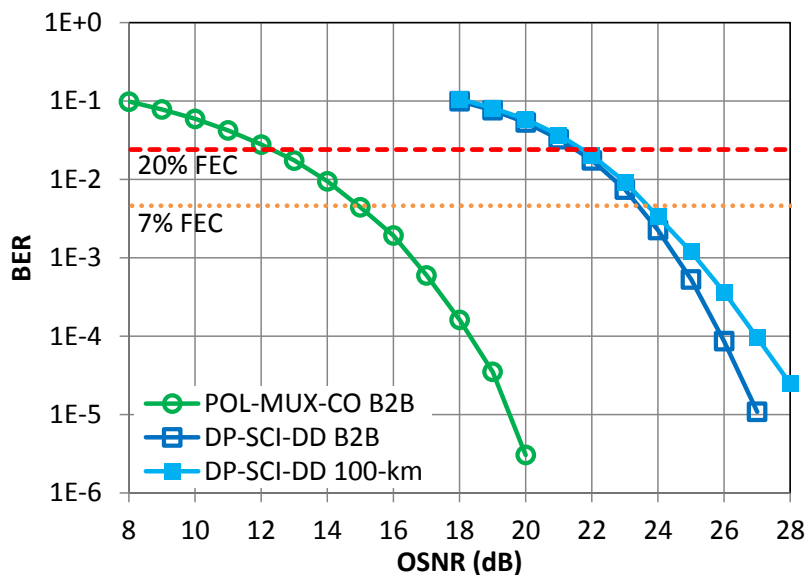


Figure 5.6 OSNR sensitivity for 100-Gb/s DP-SCI-DD systems. B2B: back-to-back measurement.

5.6 102.4-Gb/s single-polarization signal carrier interleaved direct detection

We experimentally demonstrate the SCI-DD of 2/3 SE and achieve 102.4-Gb/s direct detection optical OFDM (DDO-OFDM) reception over 80-km SSMF using single polarization [132]. Single-carrier SCI-DD system would have similar performance, as discussed by Ref. [136]. Figure 5.7 illustrates the experimental setup. The continuous wave (CW) signal of a laser is first split into two branches respectively for the signal and carrier generation. For the upper branch, the light is fed into an intensity modulator (IM) to generate 5 tones spaced at frequency of 7.34375 GHz, which satisfies the orthogonal band multiplexing (OBM) condition [78]. Then the light is fed into an I/Q modulator which is driven by an arbitrary waveform generator (AWG). RF OFDM signal generated offline with a 32-QAM modulation format is then loaded into the AWG. FFT size of the

OFDM signal is 128 in which 92 subcarriers are filled. The cyclic prefix (CP) is 22 points in order to match the length of delay line at receiver. In fact, only 4 points CP is needed in practical SCI implementation of 80-km transmission. Zero paddings with length of one OFDM symbol are inserted into time domain OFDM waveform after every two signal blocks which are reserved for carrier blocks. The AWG operates at a sampling rate of 10 GSa/s, resulting in the optical bandwidth of 7.2 GHz for one band. Total optical bandwidth is 36 GHz for five multi-bands. For the lower branch, the CW light is fed into an intensity modulator driven by a switched on/off signal of (1, 0, -1, 0) with the switched period of one OFDM symbol length. Fiber length of these two branches is carefully matched to guarantee that the signal and carrier blocks are properly interleaved without gap or overlap. The raw data rate is $36 \times 5 = 180$ Gb/s. Counting the $2/3$ spectral efficiency and OFDM overhead, the data rate is decreased to 102.4 Gb/s before 20 % FEC and 86 Gb/s after FEC. This corresponds to pre-FEC optical (electrical) spectral efficiency of 2.84 (5.68) bits/s/Hz. We note that for practical SCI application, there is no need to split the signal and carrier generation into two branches when DACs have high bandwidth and single-band OFDM can be generated (for instance, this 36-GHz OFDM signal can be generated electrically with DACs at a sampling rate of 50 GSa/s and an electrical bandwidth of 20 GHz). Carrier blocks are added at location of zero padding of signal streams digitally in this case. These two branches are combined with a coupler.

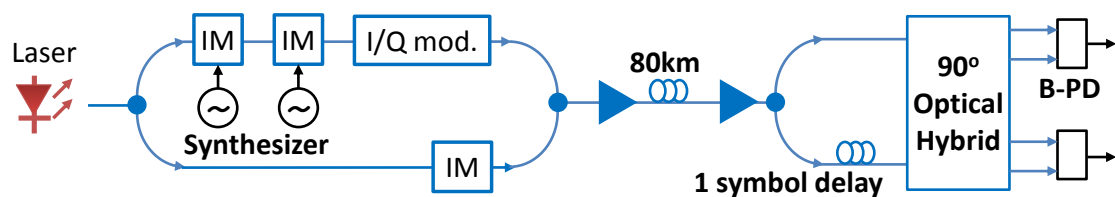


Figure 5.7 Experimental setup for SCI-DD transmission. ECL: External cavity laser; IM: Intensity modulator; I/Q mod.: I/Q modulator; AWG: Arbitrary waveform generator; TDS: Time domain sampling scope; PD: Photo-detector.

After optical amplification, the signal is launched into an 80-km SSMF link. At reception, the original signal is split into two paths with one path delayed by one symbol length. Then the two paths are launched into an optical hybrid whose output is down-converted by a pair of balanced photo-detectors. The electrical signal is sampled by a time-domain oscilloscope at a sampling rate of 50 GSa/s. Digital signal processing of the received signal includes: (1) Timing synchronization; (2) time domain signal block collection: as shown in Figure 5.5(b), for every three blocks, only two of them are collected; (3) cyclic prefix removal and FFT; (4) channel equalization; (5) phase estimation using decision-feedback method; (6) constellation reconstruction and BER calculation. Totally 3.45 million bits are collected for BER calculation.

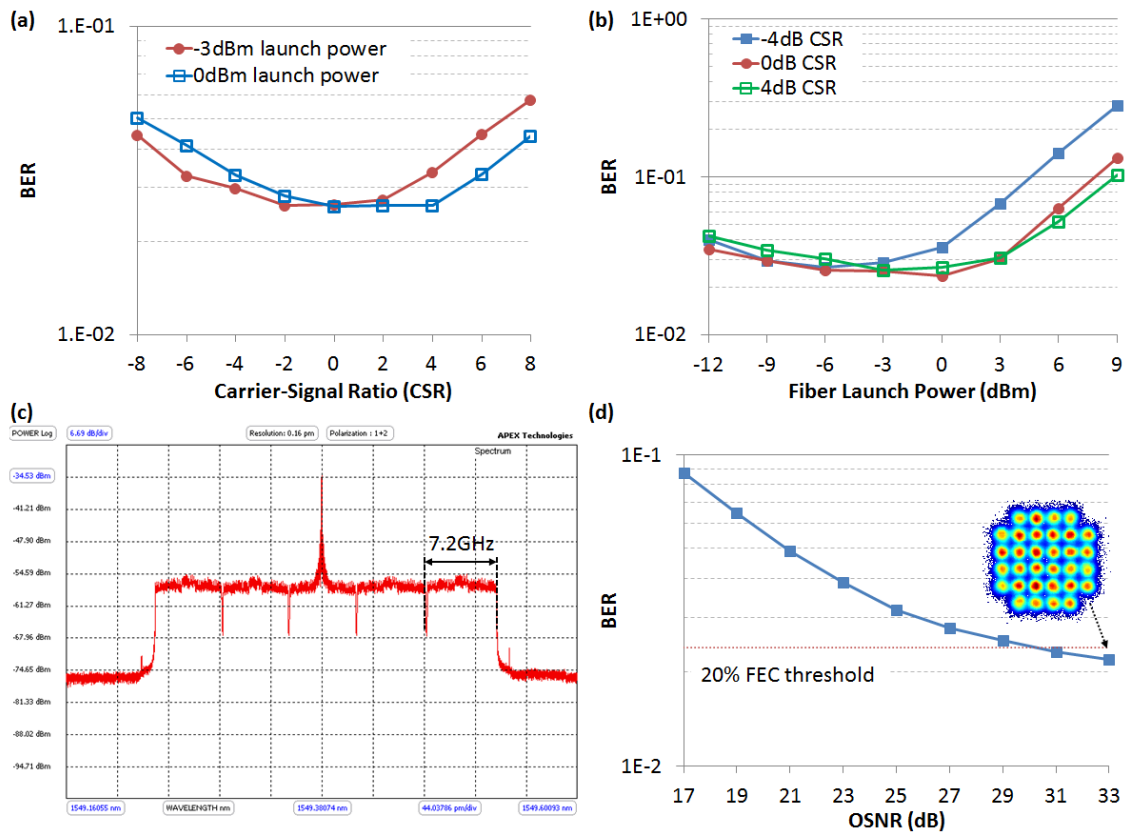


Figure 5.8 Experiment results for SCI-DD transmission over 80-km SSMF. (a) BER as a function of Carrier-Signal Ratio; (b) BER as a function of fiber launch power; (c) optical spectrum after transmission; (d) system OSNR sensitivity.

Figure 5.8(c) shows the received optical spectrum obtained from an optical spectrum analyzer (OSA). The spectrum shows five multi-bands with a total optical bandwidth of 36 GHz. The frequency component for the carrier is located at the center of the spectrum without any gap from the signal, as the consequence of our DSB modulation. We first measure the bit error rate (BER) as a function of carrier-to-signal power ratio (CSPR) as shown in Figure 5.8(a). For fiber launch power of -3 dBm, the optimal CSPR is around 0 dB. Either too high or too low CSPR will degrade the BER performance. At high input power of 0 dBm, the increased nonlinearity favors a bit high CSPR due to enhanced subcarrier-to-subcarrier four-wave-mixing (FWM). Then, we measure the BER as the function of fiber launch power as shown in Figure 5.8(b). At the CSPR of 0 dB, the optimal launch power is about 0 dBm. When the launch power is below 0 dBm, BER increases slowly when SNR decreases; when the launch power is above 0 dBm, BER performance degrades rapidly, which indicates that the system is quite sensitive to nonlinearity. Of course, high CSPR will lead to better nonlinearity tolerance, which can be observed at higher launch power of 9 dBm in Figure 5.8 (b). However, by considering both linear and nonlinear performance of varying CSPRs, the performance of 0 dB CSR is slightly better than 4 dB and -4 dB CSR as shown in Figure 5.8(b). At last, we use the CSR of 0 dB and fiber launch power of -2 dBm to measure the OSNR sensitivity of the system in Figure 5.8(d). When system OSNR is above 31dB, we successfully achieved the

100 Gb/s SCI-DD reception over 80-km fiber with BER below 0.024 (20% soft-decision FEC threshold). The inset constellation is measured at OSNR of 33 dB with a BER of 0.022. The BER floor of 2×10^{-2} can be much improved by using a wider bandwidth real-time sampling scope.

5.7 Conclusions

This chapter investigates the optical self-coherent detection subsystems. Instead of beating the signal with its own delay (the conventional self-coherent concept), the self-coherent receiver in this chapter beats the signal with a constant carrier which is sent at transmitter simultaneously with the signal. Therefore, the receiver recovers the optical field containing both the intensity and phase. The direct detection channel is linearized without need of the local oscillator in coherent detection. Digital post compensation of chromatic dispersion can be performed at receiver, which greatly elongate the achievable transmission distance of a direct detection system.

This chapter contains published contents from Ref. [62] [132] [133]. The thesis author is the primary author of the publications and has contributed more than 50 per cent of the work.

6. STOKES VECTOR DETECTION SUBSYSTEMS

In all the self-coherent schemes mentioned in chapter 5, the signal and carrier are aligned with the same polarization at transmitter. Because the photo-detectors only allow the light in the same polarization state beating with each other, the polarization alignment between the signal and carrier provides the best performance. In fact, the polarization diversity of the fiber channel can be utilized to increase the system spectral efficiency. The situation becomes more complicated because receiver needs to track the state of polarization (SOP). SOP change randomly during transmission due to the time-varying birefringence distributed along the fiber. Coherent detection brings the SOP recovery solution via 2×2 multiple-input multiple-output (MIMO) in Jones space. For direct detection, the natural way to recover the SOP is in the 3-dimension Stokes space [68], because the Stokes vector only contains the optical intensity information of orthogonal polarizations. Section 2.3 has introduced the 3-D direct detection Stokes vector receiver (SV-R). This chapter starts to introduce the other two key technologies of Stokes vector direct detection (SV-DD) [69-72,137-140]: the Stokes space modulation, and the polarization demultiplexing in Stokes space. SV-DD was first proposed for the self-coherent detection [69-71], with target transmission Cat. II and III in Table I. Soon after that, SV-R was discovered as a powerful tool for multi-dimension intensity modulation [138-140], which doubles or even triples the direct detection channel capacity per wavelength. This chapter will focus only on the self-coherent SV-DD to realize a linear complex optical channel similar to coherent detection. The multi-dimension intensity modulation in Stokes space will be presented in chapter 7.

6.1 Self-coherent Stokes space modulation

Conventionally, coherent systems exploit the fiber polarization diversity by polarization multiplexing, represented in Jones space as $\mathbf{J} = [X, Y]^T$, where X/Y is the electric field of X/Y polarization. Using Eq. (2-6), this Jones vector can be converted to Stokes space. However, SV-R is not generally regarded as a suitable receiver for the transmission of the 4-D polarization multiplexed signal: (i) Stokes vector loses 1-D information compared with the corresponding Jones vector, namely, the absolute phase of one polarization; (ii) all the elements inside the Stokes vector are the second order term of X/Y signal, leading to a nonlinear channel response. Under chromatic dispersion, the transmission distance would be significantly restricted by the power fading of the spectrum, as illustrated in Figure 1.2.

To linearize the channel, we send Y polarization as a constant carrier (C) while only the X polarization is modulated with the signal (S). The Jones vector now becomes $\mathbf{J} = [S, C]^T$, and the corresponding Stokes vector is:

$$\mathbb{S} = \begin{bmatrix} |S|^2 - |C|^2 \\ 2 \operatorname{Re}(S \cdot C^*) \\ 2 \operatorname{Im}(S \cdot C^*) \end{bmatrix} \quad (6-1)$$

The modulation dimension now becomes two for this Stokes space signal, namely, the in-phase and quadrature parts of X polarization. The 3-D SV-R is sufficient to recover this 2-D signal. The principle of the self-coherent SV-DD is fully revealed:

- (i) Combining the second and third elements of Stokes vector, we arrive at the final output of $S \cdot C^*$ that has full phase diversity of signal, from which the X-POL can be fully recovered without being affected by the dispersion induced fading.
- (ii) The nonlinearity term is completely lumped into the first element without affecting the recovered signal derived from second and third elements.

In essence, the optical fiber channel becomes a linear complex optical channel similar to coherent detection. For the first time, SV-DD achieves 100% nominal (both electrical and optical) spectral efficiency compared with the single polarization coherent detection.

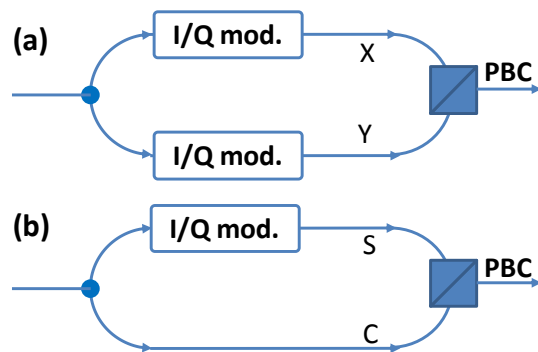


Figure 6.1 Transmitter structure for (a) POL-MUX complex modulation; (b) self-coherent Stokes-space modulation. PBC: polarization beam combiner; mod.: modulator.

6.2 Polarization demultiplexing in Stokes space

To recover the signal, the receiver needs to track the polarization rotation during the fiber transmission. In the Stokes space, this rotation can be represented by a 3×3 rotation matrix (RM). In this section, we present 3 polarization demultiplexing technics.

A. Polarization De-multiplexing using the Basis Vectors in Stokes Space

The simplest method to acquire the RM is to send three basis vectors in Stokes space [70]. As shown in Figure 6.2, each training period is divided into three time slots. Three

orthogonal training symbols with the Jones space representation of (0, 1), (1, 1) and (i, 1) are sent at the transmitter. The corresponding Stokes vectors (SV) are (-1, 0, 0), (0, 1, 0) and (0, 0, 1). The first column of the RM can be acquired by the received SV as:

$$\begin{bmatrix} S_1 \\ S_2 \\ S_3 \end{bmatrix} = \begin{bmatrix} r_{11} & \times & \times \\ r_{21} & \times & \times \\ r_{31} & \times & \times \end{bmatrix} \begin{bmatrix} -1 \\ 0 \\ 0 \end{bmatrix} \quad (6-2)$$

where r_{ij} is the matrix element of the i -th row and j -th column of the RM. Similar equations can be applied to the 2nd and 3rd columns of RM. After acquiring the RM, we multiply the received SV with the inverse of RM to obtain the transmitter SV:

$$\begin{bmatrix} |X_T|^2 - |Y_T|^2 \\ 2 \operatorname{Re}(X_T \cdot Y_T^*) \\ 2 \operatorname{Im}(X_T \cdot Y_T^*) \end{bmatrix} = \begin{bmatrix} r_{11} & r_{12} & r_{13} \\ r_{21} & r_{22} & r_{23} \\ r_{31} & r_{32} & r_{33} \end{bmatrix}^{-1} \cdot \begin{bmatrix} |X_R|^2 - |Y_R|^2 \\ 2 \operatorname{Re}(X_R \cdot Y_R^*) \\ 2 \operatorname{Im}(X_R \cdot Y_R^*) \end{bmatrix} \quad (6-3)$$

where the subscripts “T” and “R” represent for the transmitter and receiver, respectively; and superscript “-1” represents for matrix inverse.

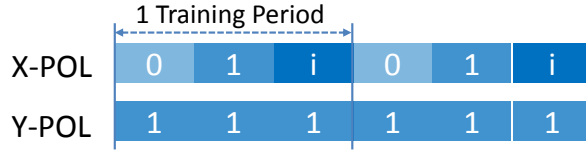


Figure 6.2 Training symbols structure for SV rotation matrix.

B. Polarization De-multiplexing using the Signal Distribution in Stoke Space

In fact, an ideal polarization rotation ignoring the polarization mode dispersion (PMD) and the polarization dependence loss (PDL) can be determined by only 2 parameters [141]: the rotation angle θ , and the phase difference $\Delta\phi$ between the two polarization modes. By investigating the distribution of the received Stokes vectors (SV), we can acquire the θ and $\Delta\phi$, from which the 3x3 rotation matrix can be reconstructed [137].

We first analyze the simplest case when the modulation format is 4-QAM. The signal maintains a constant module. By setting the carrier to signal power ratio (CSPP) as 0 dB, the transmitted SVs are simplified as: $\mathbf{S}_T = [0, 2\operatorname{Re}(S \cdot C^*), 2\operatorname{Im}(S \cdot C^*)]^T$. In Poincare sphere, all these SVs locate at the plane $X = 0$ whose normal is (1,0,0), shown by Figure 6.3(a-b). After fiber transmission, the plane experiences a 3-D rotation in Stokes space, which can be divided into two stages:

(i) the polarization rotation with angle θ , which can be expressed in Jones space as:

$$\begin{bmatrix} \cos(\theta/2) & -\sin(\theta/2) \\ \sin(\theta/2) & \cos(\theta/2) \end{bmatrix} \quad (6-4)$$

or in Stokes space as:

$$\begin{bmatrix} \cos(\theta) & -\sin(\theta) & 0 \\ \sin(\theta) & \cos(\theta) & 0 \\ 0 & 0 & 1 \end{bmatrix} \quad (6-5)$$

(ii) the phase delay $\Delta\phi$ between the two polarizations, expressed in Jones space as:

$$\begin{bmatrix} e^{-i\Delta\phi/2} & 0 \\ 0 & e^{i\Delta\phi/2} \end{bmatrix} \quad (6-6)$$

or in Stokes space as:

$$\begin{bmatrix} 1 & 0 & 0 \\ 0 & \cos(\Delta\phi) & -\sin(\Delta\phi) \\ 0 & \sin(\Delta\phi) & \cos(\Delta\phi) \end{bmatrix} \quad (6-7)$$

This plane, together with its normal vector, characterizes the states of polarization (SOP) of the received signal. Since the received SVs mix with the noise, they cannot perfectly fall into one plane. Nevertheless, we can find the least squares plane (LSP) for all the SVs [141], defined as the plane which minimizes the value $\sum_i (d_i)^2$, where d_i represents for the distance between the plane and the i -th SV. Assuming the LSP equation is $Ax + By + Cz = 0$, the normal vector of LSP should be (A, B, C) , and the distance d_i between the Stokes vectors $SV_i = [S_{i,1}, S_{i,2}, S_{i,3}]$ (i is the sequences of SV) and LSP can be expressed as:

$$\begin{bmatrix} S_{1,1} & S_{1,2} & S_{1,3} \\ S_{2,1} & S_{2,2} & S_{2,3} \\ \vdots & \vdots & \vdots \\ S_{n,1} & S_{n,2} & S_{n,3} \end{bmatrix} \cdot \begin{bmatrix} A \\ B \\ C \end{bmatrix} = \begin{bmatrix} d_1 \\ d_2 \\ \vdots \\ d_n \end{bmatrix} \quad (6-8)$$

This optimization problem can be solved by the singular value decomposition (SVD) [142] algorithm. After finding the normal of the LSP as $\mathbf{N} = (n_1, n_2, n_3)$, the rotation angle can be calculated as:

$$\theta = a \tan(\sqrt{n_2^2 + n_3^2}, n_1) \quad (6-9)$$

while the phase delay as:

$$\Delta\phi = a \tan(n_3, n_2) \quad (6-10)$$

Therefore, the 3×3 RM can be acquired by multiplying the polarization rotation matrix and the phase delay matrix

$$RM = \begin{bmatrix} 1 & 0 & 0 \\ 0 & \cos(\Delta\phi) & -\sin(\Delta\phi) \\ 0 & \sin(\Delta\phi) & \cos(\Delta\phi) \end{bmatrix} \begin{bmatrix} \cos(\theta) & -\sin(\theta) & 0 \\ \sin(\theta) & \cos(\theta) & 0 \\ 0 & 0 & 1 \end{bmatrix} \quad (6-11)$$

We extend the analysis to 16-QAM, which has 3 modules shown by Figure 6.3(c), dividing the SVs into 3 groups. By setting the CSPR as 0 dB, each group of SVs forms a plane in Stokes space at the transmitter, shown by Figure 6.3(d). We can select any group of points at the receiver to calculate the LSP and then the RM, following the procedures as 4-QAM. It is worth noting that within each plane, the power of SV (namely, S_0) maintains the same.

Now we focus on a more general case including OFDM. Different from the single-carrier modulation, where the signal modules are always discrete values, the time-domain OFDM signal has arbitrary modules. In this case, it is impossible to divide the SVs at the receiver into finite groups by the signal modules. We should investigate the distribution of SVs from a different perspective. At the transmitter, the SVs form the distribution of $[|S|^2 - |C|^2, 2\text{Re}(S \cdot C^*), 2\text{Im}(S \cdot C^*)]^T$. The carrier (C) maintains constant with a normalized power (namely $C = 1$). The distribution can be simplified as

$$\begin{bmatrix} S_1 \\ S_2 \\ S_3 \end{bmatrix} = \begin{bmatrix} |S|^2 - 1 \\ 2\text{Re}(S) \\ 2\text{Im}(S) \end{bmatrix} \quad (6-12)$$

In Stokes space, the SVs in Eq. (6-12) distribute on a surface with the curve equation

$$S_1 = (S_2^2 + S_3^2) / 4 - 1 \quad (6-13)$$

This curve has a symmetric axis $(1,0,0)$, as illustrated in Figure 6.3(e). At the receiver, by estimating the distribution of the SVs, we are able to perform the curve fitting to find out the symmetric axis. This axis, like the normal vector of the LSP in 4-QAM, contains the information of 3-D rotation. Therefore, Eq. (6-11) can be applied to estimate the RM.

To acquire the symmetric axis of the surface, we select a group of SVs whose power S_0 locates in the range $[a_1, a_2]$. When the difference between a_1 and a_2 is small, this subset of SVs approximately forms a plane. This plane is a cross section of the surface, which is perpendicular to the symmetric axis. Therefore, the normal of this plane can be regarded as the symmetric axis.

We have fully illustrated the algorithm to blind estimate the RM using the distribution of the SVs at the receiver, regardless of any modulation format. By multiplying the received SV with the inverse of the RM, we finally recover the signal in Stokes space as $[|S|^2 - |C|^2, 2\text{Re}(S \cdot C^*), 2\text{Im}(S \cdot C^*)]^T$.

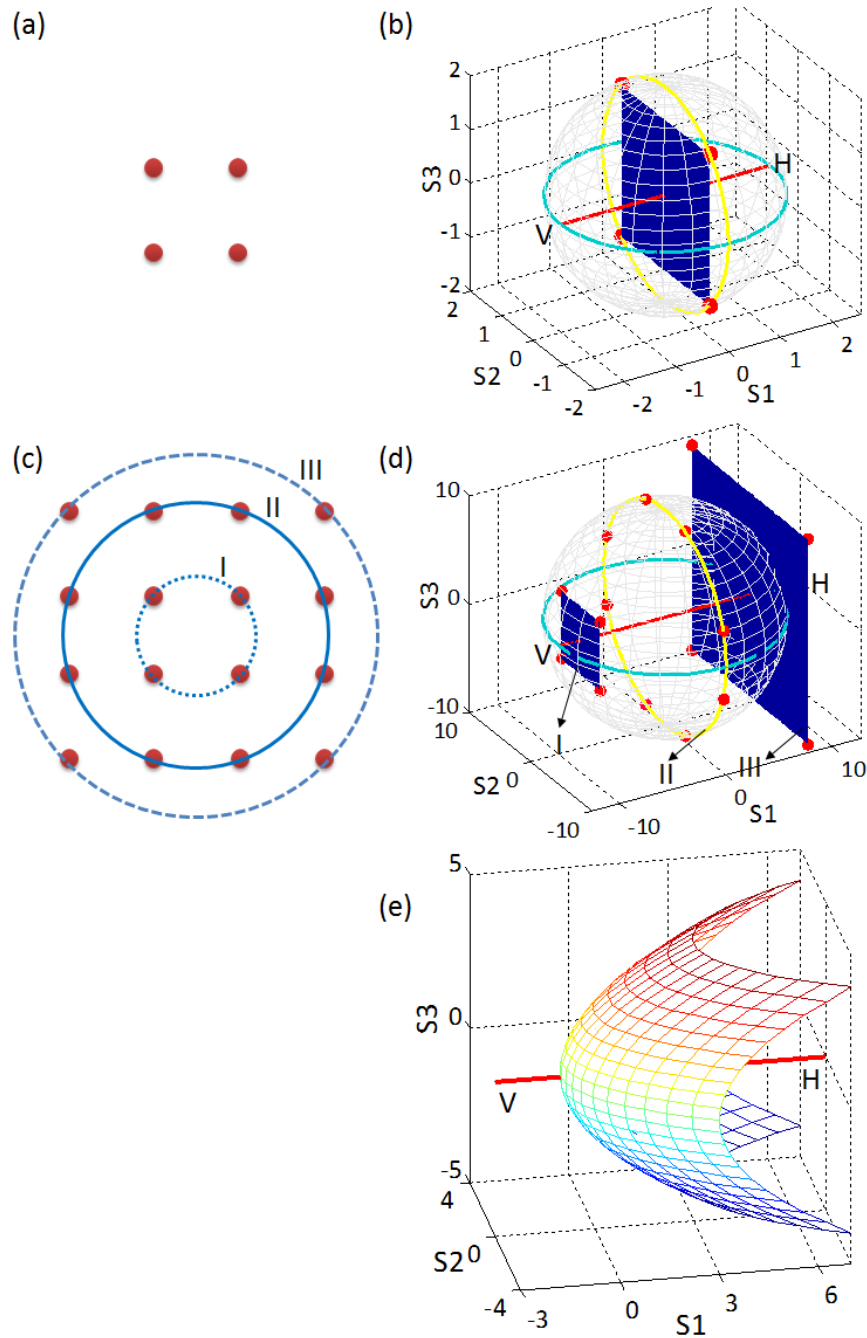


Figure 6.3 4-QAM constellation in (a) Jones space; (b) Stokes space. 16-QAM constellation in (c) Jones space; (d) Stokes space. (e) Surface of Eq. (6-13) in Stokes space (time-domain OFDM signal distribution).

C. Polarization De-multiplexing using the Blind Adaptive Algorithm

The signal after the Stokes vector receiver goes through a 3×2 real-value multiple-input multiple-output (MIMO) channel. The channel takes 3 inputs as the 3 elements of Stokes vector, and offers 2 outputs which can then be combined to a complex signal. The MIMO technique can be applied to the SV-DD to perform the polarization de-multiplexing in 3-D Stokes space [138-140,143-146].

As an example, we propose an adaptive equalizer using the least-mean square (LMS) algorithm [143] as Figure 6.4. The equalizer has 3 real-value inputs, corresponding to the 3 elements of the SV; 1 complex value output, corresponding to the complex modulated signal $s(k)$ after polarization rotation, where k is a time index. The relationship between the equalizer coefficients (c_1 , c_2 and c_3) and the inversion of RM are:

$$c_n = h_{2n} + jh_{3n} \quad (n = 1, 2, 3) \quad (6-14)$$

where h_{mn} denotes the matrix element of m -th row and n -th column in RM^{-1} . The adaptive algorithm contains the following procedures: (i) initialize the filter coefficients; (ii) equalize the received SV by

$$s(k) = [c_1, c_2, c_3] \cdot [S_1, S_2, S_3]^T \quad (6-15)$$

(iii) calculate the instantaneous error $e(k) = d(k) - s(k)$, where $d(k)$ is the constellation point closest to the $s(k)$; (iv) update the filter coefficients by

$$c_n(k+1) = c_n(k) + \mu \cdot e(k) \cdot S_n^*(k) / \|\mathbf{S}(k)\|^2 \quad (6-16)$$

where μ is the step size of the filter, $\|\cdot\|^2$ denotes the L₂ norm of braced vector, and $\mathbf{S}(k) = [S_1(k), S_2(k), S_3(k)]$ represents the received SV at the k -th sampling point.

More generally, the LMS algorithm can be replaced by any other adaptive algorithm such as the constant module algorithm (CMA) and recursive least square algorithm (RLS), depending on different channel conditions.

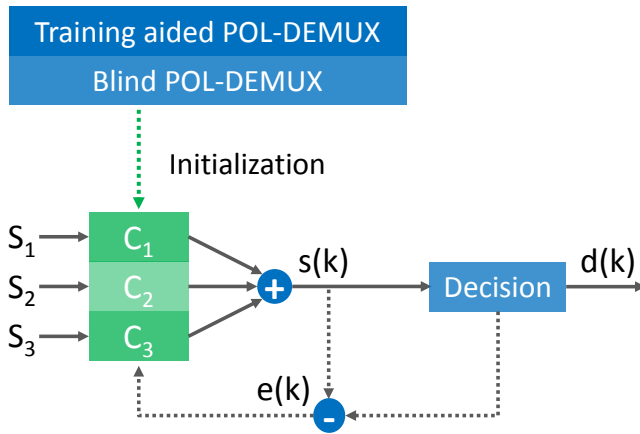


Figure 6.4 Structure of the blind adaptive equalizer for SV-DD.

When using the blind adaptive algorithm, either the training assisted RM estimation (TA-E) in Section 6.2.A or blind RM estimation (B-E) in Section 6.2.B can provide an initialization tool for the 3×2 equalizer to accelerate its convergence speed. After convergence, the equalizer can be switched to the decision direct mode, with any adaptive algorithm to update the equalizer coefficients. The polarization demultiplexing DSP becomes much more compact and simpler.

6.3 Transmission experiments of Stokes vector direct detection

A. 13.3-Gbaud 64-QAM (80 Gb/s) OFDM signal over 160-km SSMF

We demonstrate the SV-DD in OFDM systems to prove the effectiveness of the scheme [147]. Figure 6.5 illustrates the experimental setup. The CW signal of a laser is first split into two branches respectively for the signal and carrier. For the signal branch, the optical signal is fed into an I/Q modulator driven by an arbitrary waveform generator (AWG), resulting in a double sideband modulation. The RF OFDM signal with a 64-QAM modulation is loaded into the AWG. The FFT size of the OFDM signal is 4096 in which 2184 subcarriers are filled. The cyclic prefix (CP) is 128 points. The SV training symbols are added before one OFDM frame with period length of 384 points (Each period includes three time slots shown in Figure 6.2). The AWG operates at a sampling rate of 25 GSa/s, leading to an optical bandwidth of 13.33 GHz. The raw data rate is $13.33 \times 6 = 80$ Gb/s. Counting the OFDM overhead, the data rate is decreased to 77.6 Gb/s before 20% FEC and 64.7 Gb/s after FEC. This corresponds to pre-FEC electrical spectral efficiency (SE) of 11.64 bits/s/Hz and post-FEC SE of 9.71 bits/s/Hz. The lower branch is a delay line whose fiber length is matched with the upper line to cancel the phase noise between signal and carrier. Signal carrier power ratio (CSPR) is maintained to be 0 dB. These two branches are combined with a polarization beam combiner (PBC) and then launched into 2-span 80-km SSMF link. Signal carrier power ratio (CSPR) is maintained to be 0 dB. These two branches are combined with a polarization beam combiner (PBC) and then launched into 2-span 80-km SSMF link.

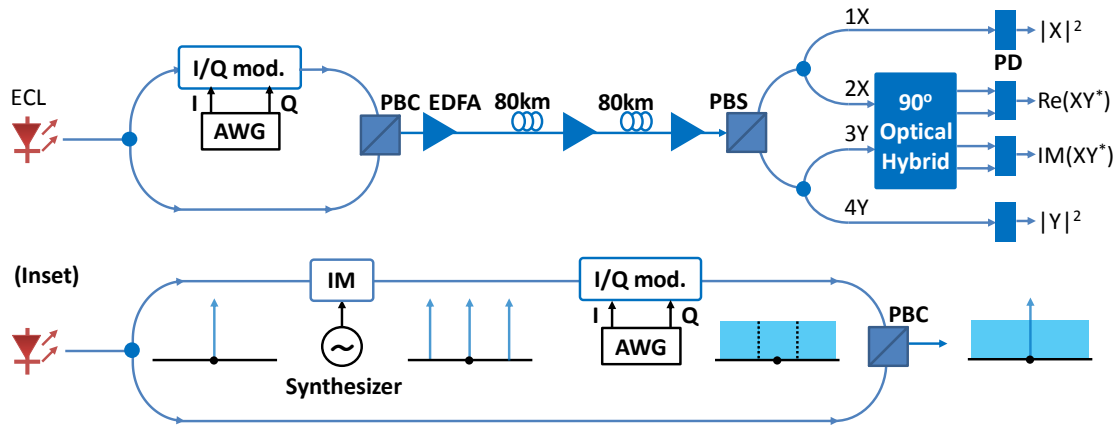


Figure 6.5 Experimental setup for SV-DD. Inset: SV transmitter with the orthogonal multi-band generator. ECL: External cavity laser; I/Q: in-phase/quadrature; I/Q mod.: I/Q modulator; IM: intensity modulator; AWG: Arbitrary waveform generator; PBC: Polarization beam combiner; EDFA: Erbium Doped Fiber Amplifier; PBS: Polarization beam Splitter; PD: Photo-detector.

At reception, the optical signal is split using a polarization beam splitter (PBS). We adopt the SV receiver in Figure 2.4(a) to measure the SV. Polarization X and Y are equally split into two branches with two 3-dB couplers. Ports 2 and 3 are fed into a standard balanced receiver. Ports 1 and 4 should be fed into a balanced PD, while in the experiment we send them to two single-ended PDs and balance them in digital signal processing (DSP).

The electrical signal is sampled by a real-time oscilloscope at 50 GSa/s. DSP of the received signal includes: (i) OFDM window synchronization; (ii) SV rotation matrix estimation using basis vectors in Stokes space and polarization inversion; (iii) cyclic prefix removal and FFT; (iv) channel equalization; (v) constellation reconstruction and BER calculation. 2.62 million bits are collected for BER calculation.

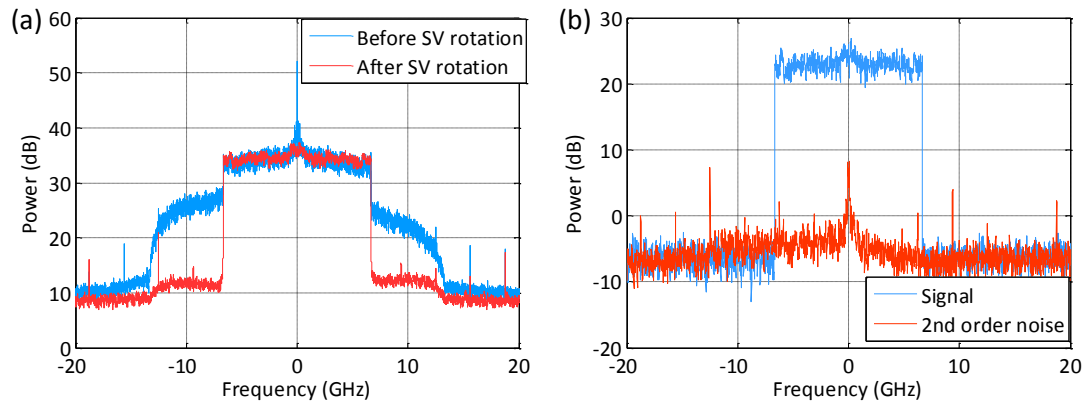


Figure 6.6 (a) Electrical spectra of received signals before and after the SV rotation; (b) Electrical spectra of received signal and 2nd order nonlinearity after SV rotation.

We first compare the electrical spectra before and after the SV rotation in Figure 6.6(a) to comprehend the effect of the SV rotation. The blue line in the figure represents the spectrum for $X \cdot Y^*$. As we mentioned before, both X and Y contains signal components. As a result, their product generates the 2nd order frequency component within the frequency range from -13.3 to 13.3 GHz. However, the transmitted signal only has an optical bandwidth of 13.3 GHz, corresponding to an electrical range from -6.7 to 6.7 GHz. Therefore, we can observe the noise pedestal in the range of $[6.7, 13.3]$ GHz and $[-13.3, -6.7]$ GHz. In contrast, after the SV rotation, $X \cdot Y^*$ is converted back to $S \cdot C^*$, leading to the suppression of the 2nd order product. This can be verified by the disappearance of nonlinearity noise in the same frequency range of $[6.7, 13.3]$ GHz and $[-13.3, -6.7]$ GHz. In order to measure the 2nd nonlinearity after SV rotation, in OFDM training symbols, we only fill in the odd subcarriers and leave the frequency gaps at the even subcarriers. Therefore, the even subcarriers would contain all the 2nd nonlinearity noise while odd subcarriers only contain pure signal [126]. Figure 6.6(b) shows the spectra for the 2nd nonlinearity at even subcarriers as well as the signal at odd subcarriers. After SV rotation, the spectrum of the 2nd nonlinearity has the power level nearly the same as the noise level of the signal spectrum. The SV rotation successfully removes the 2nd nonlinearity and image subcarrier interference, and subsequently no fading is observed.

We then measure the OSNR sensitivity of the system as shown in Figure 6.7. For 160 km SSFM transmission, SV-DD requires an OSNR of about 25 dB for 13.34 GHz 64-QAM signal to achieve the BER below 20% FEC threshold. Considering the highest system OSNR of 33.5 dB in the experiment, there is a large system margin between 25 dB and

this value, revealing the potential for SV-DD to achieve higher data rate and longer transmission distance.

One may question whether in SV-DD additional receiver bandwidth is needed to detect the 2nd components in the frequency range of $[\pm 6.7, \pm 13.3]$ GHz. To resolve the question, we add an ideal rectangular digital band-pass filter to the three components of the SV at the beginning of the DSP, whose bandwidth is just the same as that of the transmitted signal. The BER vs. OSNR curve with the filter nearly coincides with the one without filter as shown in Figure 6.7. Therefore, we conclude that SV-DD does not require any bandwidth wider than that of the signal, which guarantees its high electrical spectrum efficiency.

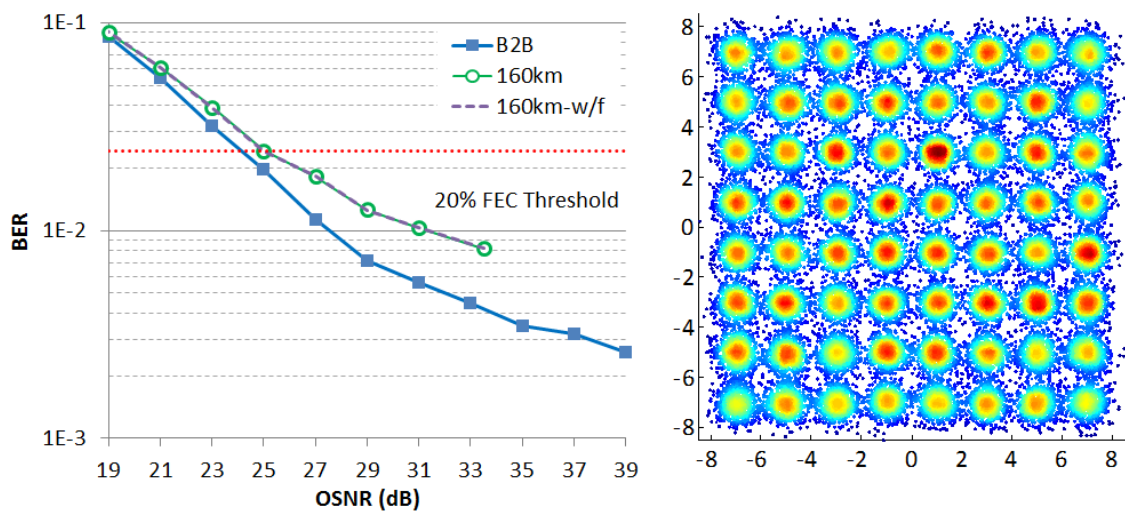


Figure 6.7 System OSNR sensitivity in an 80 Gb/s SV-DD experiment. Inset to the right: 64-QAM constellation. B2B: back-to-back measurement; w/f: with filter.

B. 40-Gbaud 16-QAM (160 Gb/s) OFDM signal over 160-km SSMF

To generate a wider optical bandwidth, the orthogonal band multiplexing (OBM [78]) is applied to the optical transmitter. Using almost the identical setup illustrated in Figure 6.5, we add a multi-band generator before the I/Q modulator to generate three orthogonal bands which have a total optical bandwidth of 40 GHz, as shown by the inset of Figure 6.5. Using the 16-QAM modulation, the raw data rate is $40 \times 4 = 160$ Gb/s [69]. Counting all the OFDM overhead, the data rate is decreased to 155.2 Gb/s before 20 % FEC and 129.3 Gb/s after FEC. This corresponds to pre-FEC electrical spectral efficiency (SE) of 7.76 bits/s/Hz and post-FEC SE of 6.46 bits/s/Hz. Totally 6.55 million bits are collected for BER calculation.

To determine the optimum fiber launch power for 160-km SSMF transmission, we measure the bit error rate (BER) as the function of fiber launch power as shown in Figure 6.8(a). For 1-band 64-QAM (80-Gb/s data rate) transmission, the optimum launch power is between 0 and 2 dBm; while for 3-band 16-QAM (160-Gb/s data rate), the optimum

value is 4 dBm. While the data rate doubles, optimum launch power correspondingly increases 3dB. The optimum launch power for both data rate is nearly 3 dB higher compared with coherent detection. This is because half of the launch power is taken by the carrier in SV-DD. Using the optimum launch power, we measure the OSNR sensitivity of the system as shown in Figure 6.8(b). To achieve BER below 20% FEC threshold, SV-DD only requires an OSNR of 24 dB for 160 Gb/s signal. The inset is a constellation measured for 3-band signal at an OSNR of 35 dB with a BER of 0.002.

The SV-DD system has more than 10 dB system margin of OSNR, considering the difference between the highest OSNR achieved in the experiment and the 20% FEC threshold, SV-DD possesses a great potential to support higher data rate transmission over short to medium distance. Terabit transmission for SV-DD is possible with the use of WDM.

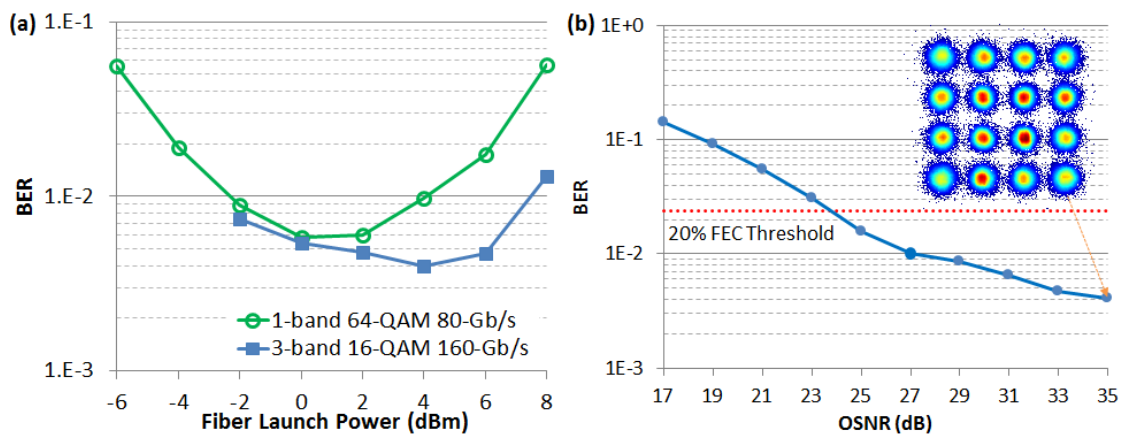


Figure 6.8 160-Gb/s SV-DD system performance. (a) BER as a function of fiber launch power; (b) OSNR sensitivity.

C. 10 wavelength 25-Gbaud 16-QAM (1-Tb/s) signal over 480-km SSMF

We experimentally demonstrate the 1-Tb/s (10×100 Gb/s) direct detection with 480-km SSMF transmission using SV-DD [148]. Figure 6.9 illustrates the experimental setup. At the transmitter, 10 CW lasers are multiplexed by the coupler with the channel spacing of 50 GHz. The combined light is first split into two branches respectively for the signal and carrier. For the signal branch, the optical signal is fed into a 3-tone generator [78] to achieve wider optical bandwidth, then fed into an I/Q modulator driven by an arbitrary waveform generator (AWG). The RF OFDM signal with a 16-QAM modulation is loaded into the AWG. The FFT size of the OFDM signal is 4096 in which 3420 subcarriers are filled. The cyclic prefix (CP) is 128 points. SV rotation training symbols are added before each OFDM frame with symbol length of 192 points. The AWG operates at a sampling rate of 10 GSa/s, leading to the optical bandwidth of 8.33 GHz for 1-band and total optical bandwidth 25 GHz for 3-band. The raw data rate is $25 \times 4 = 100$ Gb/s for one channel and 1 Tb/s for 10 channels. Counting the OFDM overhead, the data

rate is decreased to 969.7 Gb/s before 20 % FEC and 808.1 Gb/s after FEC. This corresponds to pre-FEC electrical spectral efficiency (SE) of 7.76 bits/s/Hz and post-FEC SE of 6.47 bits/s/Hz. The lower branch is a delay line whose fiber length is matched with the upper line to cancel the phase noise between the signal and the carrier. Signal carrier power ratio (CSPR) is maintained to be 0 dB. These two branches are combined with a polarization beam combiner (PBC) and then launched into a recirculation loop which consists of two spans of 80-km SSMF whose loss is compensated by the EDFAs. The inset (i) of Figure 6.9 shows the spectrum at the transmitter captured by the optical spectrum analyzer (OSA). Each channel has the baud rate of 25 Gbaud/s, corresponding to 0.2 nm in terms of wavelength; the channel spacing is 0.4 nm (or 50 GHz). Totally 4 nm bandwidth is occupied.

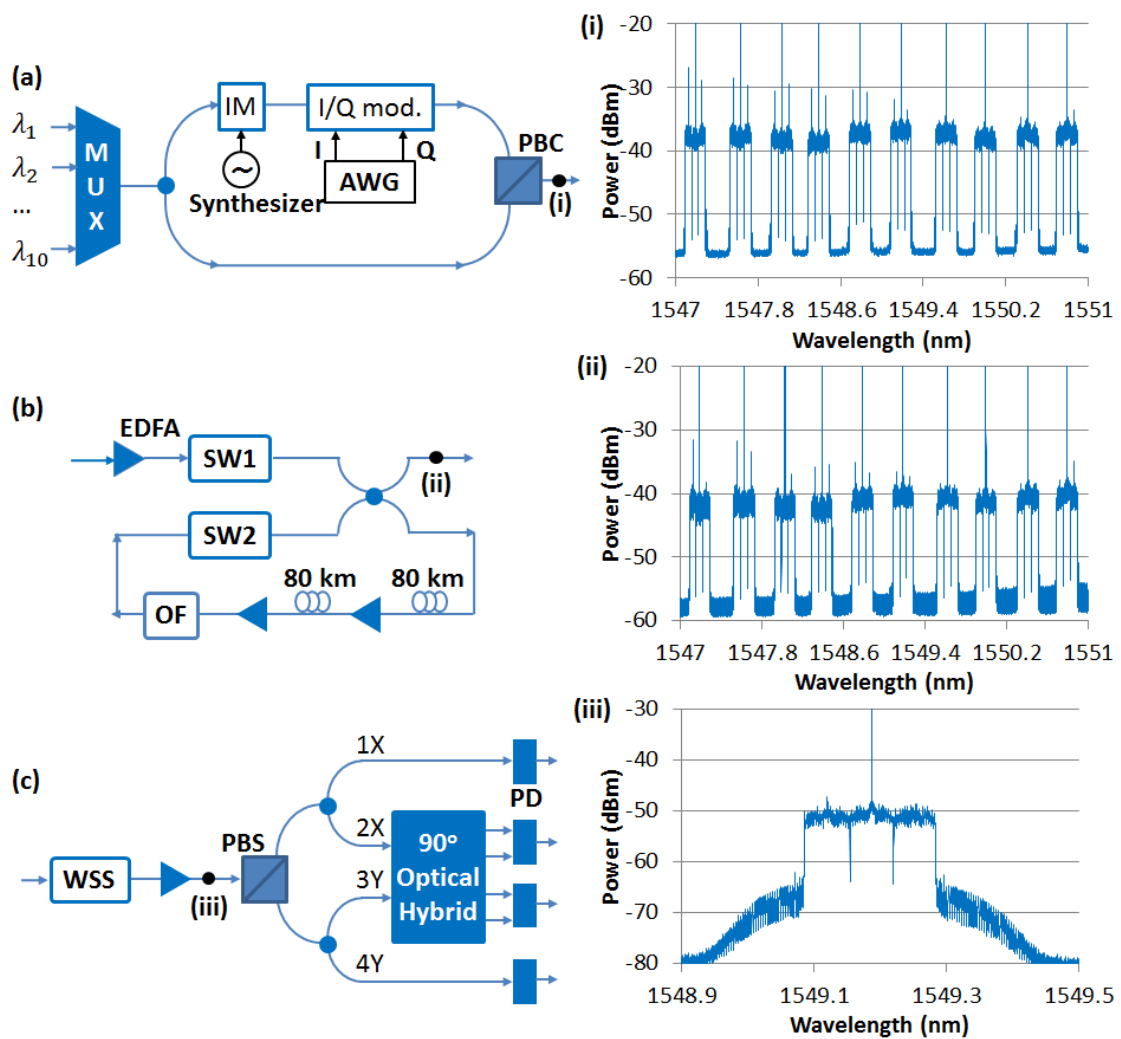


Figure 6.9 Experimental setup for 1-Tb/s SV-DD. (a) Transmitter; (b) fiber recirculating loop; (c) Receiver. (Inset (i) spectrum before transmission, (ii) spectrum after 480-km transmission, and (iii) spectrum of channel 6 after wave-shaper.) MUX: multiplexer (10x1 coupler); IM: intensity modulator; I/Q mod. I/Q modulator; AWG: arbitrary waveform generator; PBC/S: polarization beam combiner/splitter; EDFA: erbium doped fiber amplifier; SW: optical switch; BPF: band-pass filter; WSS: wavelength selective switch; PD: photo-detector.

At reception, the light is fed into a band pass filter to filter out one channel each time which occupies a 40 GHz bandwidth and carries 100 Gb/s data. The inset (iii) in Figure 6.9 shows the spectrum after the filter. The spectrum presents a double sideband modulation (DSB), and the carrier is shown by the power peak at the center. The optical signal is then split using a polarization beam splitter (PBS). Polarizations X and Y are equally split into two branches by two 3-dB couplers. Ports 2 and 3 are fed into a standard coherent receiver. Ports 1 and 4 can be fed into a balanced PD, while in experiment we send them to two single-ended PDs and balance them in DSP. The electrical signal is sampled by a real-time oscilloscope at a sampling rate of 50 GSa/s with 15-GHz electrical bandwidth. Totally 5.24 million bits are collected for BER calculation of one channel.

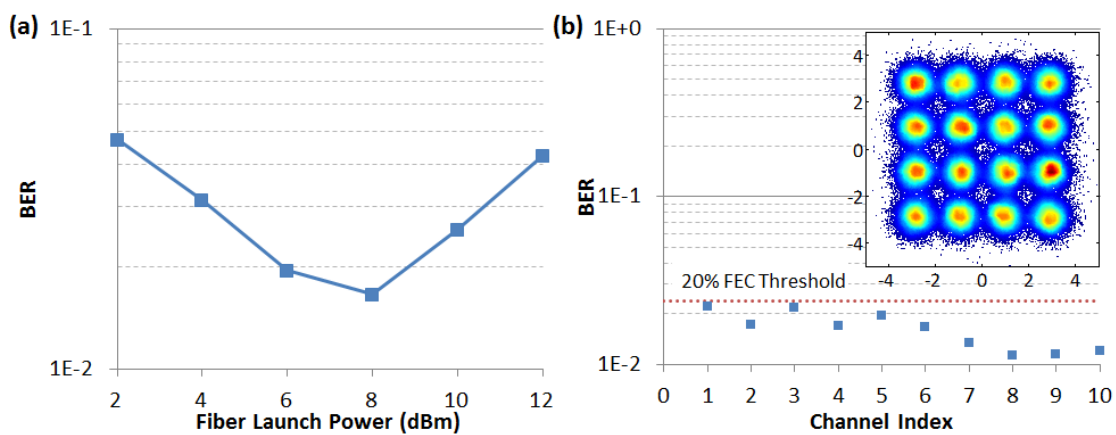


Figure 6.10 1-Tb/s SV-DD transmission performance. (a) BER performance as a function of fiber launch power; (b) BER performance for each 100-Gb/s channel after 480-km transmission.

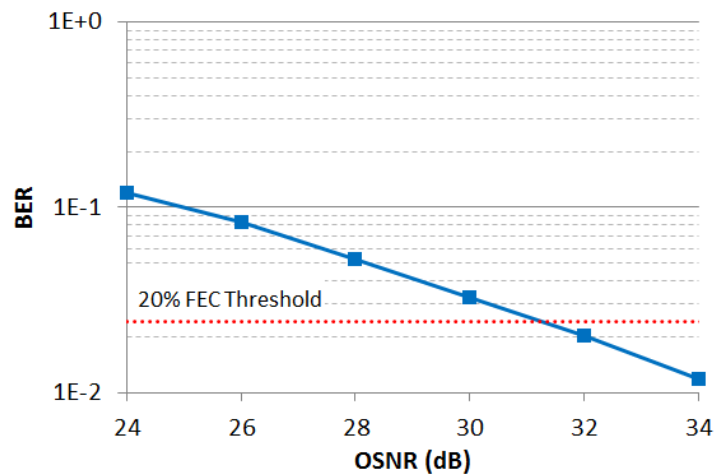


Figure 6.11 1-Tb/s SV-DD system OSNR sensitivity. The OSNR are for 10 wavelengths, and should be reduced by 10 dB for single wavelength.

We first measure the bit error rate (BER) as the function of fiber launch power as shown in Figure 6.10(a) to identify the fiber nonlinearity tolerance for this 1-Tb/s system. The optimum launch power is 8 dBm. Then, we measure the BER performance for all the 10 channels at the reach of 480 km with the launch power of 8 dBm. As shown in Figure 6.10(b), all the bands can achieve the BER lower than 0.024, the threshold of 20% FEC.

The inset of Figure 6.10(b) is a constellation measured for channel 6 at an OSNR of 34 dB with a BER of 8.8×10^{-3} .

Figure 6.11 shows the system OSNR sensitivity. For 480 km SSFM transmission, SV-DD requires an OSNR of about 31 dB for 10×25 -Gbaud 16-QAM signals to achieve the BER below 20% FEC threshold. Considering the highest OSNR of 34 dB achieved in the experiment, the system OSNR margin is about 3 dB between 31 dB (20% FEC threshold) and this value. Compared with previous 1-Tb/s POL-MUX coherent detection [13], the required OSNR at 20% FEC threshold is about 25 dB for 1 Tb/s coherent system. The experimental result indicates a 6 dB OSNR sensitivity penalty for SV-DD, which agrees with the theoretical prediction: since half of the optical power is shared by the carrier at the SV-DD transmitter, there is 3 dB intrinsic OSNR penalty; SV-DD suffers noise degradation for both carrier and signal from dual polarization, leading to another 3 dB OSNR penalty compared with POL-MUX system. Nevertheless, this OSNR sensitivity is still much better than the conventional single-end PD based DD, because SV-DD does not need a high CSNR to suppress the 2nd order nonlinearity.

The performance for this initial 1-Tb/s SV-DD transmission is limited primarily by the multi-tone generator, which has an EDFA inside sacrificing the system OSNR and therefore degrading the OSNR sensitivity. In practice, the 25 Gbaud signal can be generated with a higher sampling rate digital-to-analog converter (DAC). Moreover, by using higher baud rate transmitter with lower modulation format, SV-DD can even support a transmission distance of more than 1000 kilometers, which reveals the flexible capability for SV-DD to be deployed in short reach applications.

6.4 Experiment for polarization demultiplexing algorithms

We experimentally verify the polarization demultiplexing algorithms proposed above [137]. The experimental setup is the same as Figure 6.5. However, instead of using OFDM modulation, we use a 10-Gbaud single carrier signal. The receiver DSP procedures include: (i) chromatic dispersion compensation; (ii) time synchronization; (iii) polarization de-rotation in Stokes space; (iv) adaptive channel equalization using the recursive least square (RLS) algorithm; (v) constellation reconstruction and BER calculation. Instead of combining the polarization de-rotation and channel equalization mentioned in Section 6.2, we separate these two DSP procedures to directly evaluate the performance of the polarization de-rotation algorithms.

We first present the effectiveness of the blind RM estimation (B-E) by illustrating the 3-D polarization de-rotation in Stokes space. Figure 6.12 (a-b) depicts the received Stokes vector (SV) distributions in Poincare sphere (S_1, S_2, S_3). H and V represent for the linear horizontal and linear vertical polarization states, respectively. Figure 6.12(a) is the received 4-QAM SVs. The figure shows 400 data points in Stokes space. The 3×3 RM is

calculated from the normal of LSP (indicated by the “N” in Figure 6.12(a)) via Eq. (6-11). Figure 6.12(b) illustrates the SVs after multiplying the inverse of RM, in which the polarization has been aligned to H-V direction properly. The 2-D constellation of $S_2 + iS_3$ further reveals the effectiveness of B-E. After polarization de-rotation, the constellation cloud in Figure 6.12(c) become much visible in Figure 6.12(d), and the constellation is completely restored after the subsequent channel equalization as shown in Figure 6.12(e).

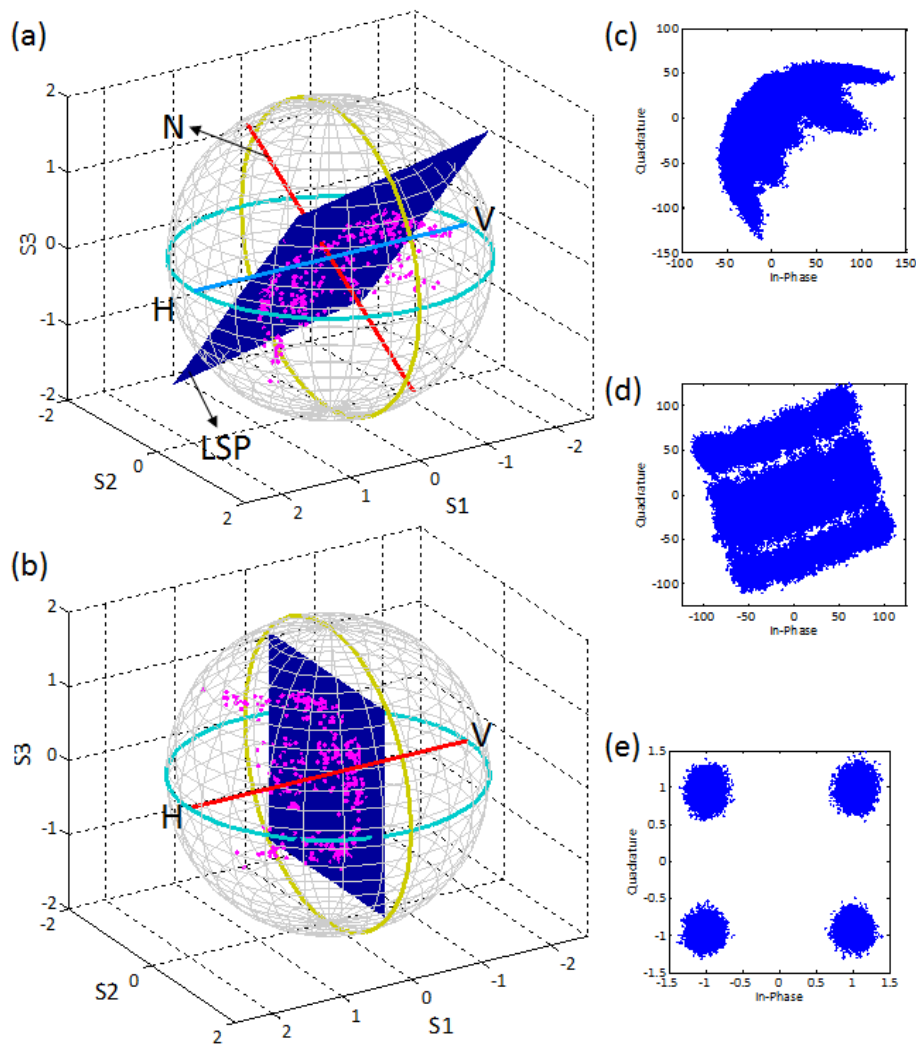


Figure 6.12 Received Stokes vectors in Poincare sphere with 4-QAM modulation (a) before polarization de-multiplexing; (b) after polarization de-multiplexing; 4-QAM constellation (c) before polarization de-multiplexing; (d) after polarization de-multiplexing; (e) after channel equalization.

We then compare the performance between the training assisted RM estimation (TA-E) and B-E. Considering the SV-DD system realizes a linear channel similar to the coherent detection, it supports the transmission over several hundreds of kilometers. In such a DD system, the channel additive white Gaussian noise (AWGN) dominates the noise source instead of the receiver noise. We thus evaluate the system with the metric of system OSNR sensitivity.

By loading the optical noise at the receiver front end, we first measure the BER as the function of OSNR in a 10-Gbaud 4-QAM system. For both back-to-back (B2B) and 160-km measurements, minor OSNR sensitivity difference can be distinguished between the TA-E and the B-E at 7% FEC threshold. TA-E presents a little bit advantage over B-E, revealing that the 3×3 polarization rotation process in practical system is not ideally behaved as the model shown by Eq. (6-11). As expected, the RM is more accurate when modeling by 9 parameters in TA-E than by 2 parameters in B-E, with the sacrifice of computational complexity. It is worth noting that the required OSNR for the BER of 7% FEC threshold is almost the same between the B2B and 160-km measurement, namely, the performance experiences little degradation even after 160-km transmission.

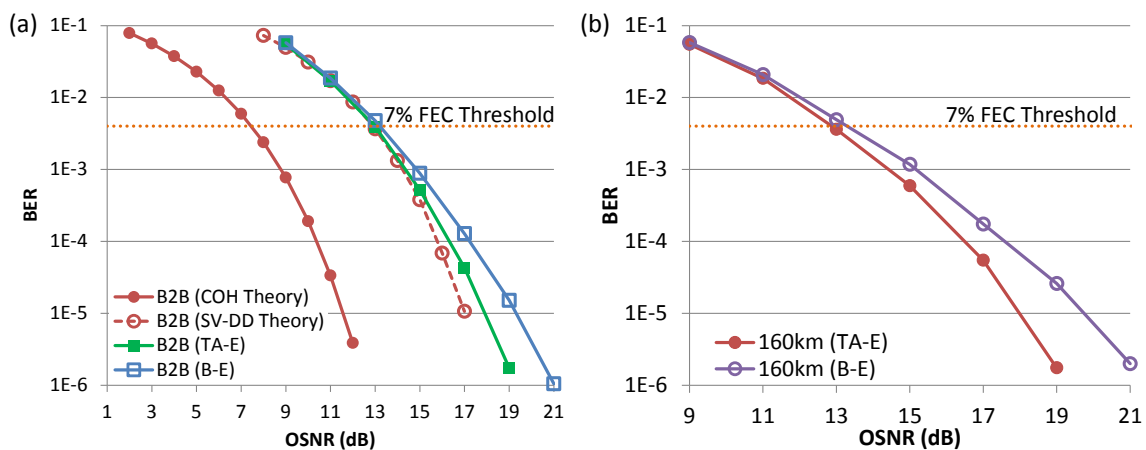


Figure 6.13 System OSNR sensitivity for 20-Gb/s 4-QAM system. (a) back-to-back (B2B); (b) 160km. COH: standard coherent detection; TA-E: training assisted estimation; B-E: blind estimation.

When switching the modulation format to 16-QAM while maintains the baud rate as 10 Gbaud/s, the OSNR sensitivity difference between the TA-E and B-E become slightly larger to 1-2 dB at 7% FEC threshold. This is because the system error floor is quite close to the FEC threshold.

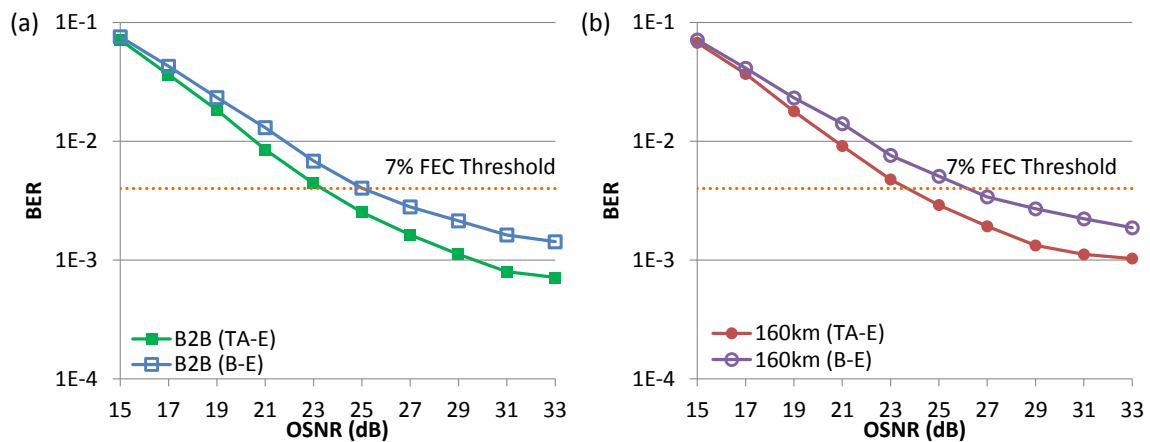


Figure 6.14 System OSNR sensitivity for 40-Gb/s 16-QAM system. (a) back-to-back (B2B); (b) 160km. TA-E: training assisted estimation; B-E: blind estimation.

6.5 PMD impact on Stokes vector direct detection

SV-DD uses single-polarization modulation to keep the simplicity of transmitter structure. Therefore, the SV rotation algorithm only provides the rotation information at the carrier frequency ω_c . Due to the polarization mode dispersion (PMD), the evolution of the polarization during fiber transmission varies with the frequency [70,149]. Under the first-order PMD approximation, the polarization rotation matrix in Jones space at frequency ω is:

$$U(\omega) = \begin{bmatrix} a_2 & b_2 \\ -b_2^* & a_2^* \end{bmatrix} \begin{bmatrix} e^{-j\omega\Delta\tau/2} & 0 \\ 0 & e^{j\omega\Delta\tau/2} \end{bmatrix} \begin{bmatrix} a_1 & b_1 \\ -b_1^* & a_1^* \end{bmatrix} \quad (6-17)$$

where the first and third matrices are frequency independent, denoting the polarization rotation at the fiber output and input. The second matrix is frequency dependent, denoting the differential group delay (DGD) $\Delta\tau$ between the principle polarizations. The signal at $\omega_c + \omega_i$ experience the channel of $U(\omega_c + \omega_i)$, however, we use the rotation matrix $U(\omega_c)$ to recover the signal at ω_i :

$$\begin{bmatrix} X_i \\ Y_i \end{bmatrix} = U^{-1}(\omega_c)U(\omega_c + \omega_i) \begin{bmatrix} S_i \\ 0 \end{bmatrix} \quad (6-18)$$

where S_i represents the transmitted signal at the frequency of $\omega_c + \omega_i$ and Eq. (6-18) represents the channel equalization at frequency domain. Therefore, the Y-POL after equalization is not the pure carrier as expected but the mixture of the signal and the carrier. Substituting Eq. (6-17) into Eq. (6-18), and assuming $\omega_i\Delta\tau \ll 1$ ($\cos \omega_i\Delta\tau \approx 1$, $\sin \omega_i\Delta\tau \approx 0$ and $\sin \omega_i\Delta\tau \cong \omega_i\Delta\tau$) for short-reach transmission, the signal after SV rotation algorithm can be expressed as:

$$X \cdot Y^* = \sum_i S_i e^{j\omega_i t} + 2ja_1^* b_1 \Delta\tau \sum_i S_i e^{j\omega_i t} \cdot (\omega_i S_i e^{j\omega_i t})^* \quad (6-19)$$

The first term on the right side is the desired signal, and the second term is the 2nd-order nonlinear noise. This PMD induced noise would degrade the system performance.

Adopting a simulation setup similar to that illustrated in Figure 6.5, we change the 160-km SSMF to the PMD emulator which adds arbitrary differential group delay (DGD) to the signal. We first investigate the Q-factor penalty as a function of the DGD with an optical signal bandwidth of 50 GHz as shown in Figure 6.15 by the blue rectangle line. The Q-penalty refers to the system BER level of 10^{-3} . The Q-penalty experiences a quasi-linear increase with respect to DGD. At DGD of 10 ps, the Q-penalty is less than 4 dB. Despite such a conspicuous penalty, DGD of 10 ps corresponds to a SSMF transmission distance of 1000 km, if a PMD parameter of $0.1 \text{ ps}/\sqrt{km}$ is used and maximum instantaneous DGD is assumed about 3 times of mean PMD. SV-DD is not designed for the long-haul transmission. If we only consider the distance within 400 km, which is sufficient for the short-reach application, the PMD is less than 2 ps for SSMF. The further

the frequency is away from the DC, the more the signal will mix into the carrier polarization. As a consequence, the Q-penalty increases when the bandwidth becomes broader. For a fixed DGD of 2 ps as shown in Figure 6.15, it is found that the PMD induced Q-penalty is less than 0.5 dB even with a 50 Gbaud system, revealing the capability for SV-DD to support high-speed transmission.

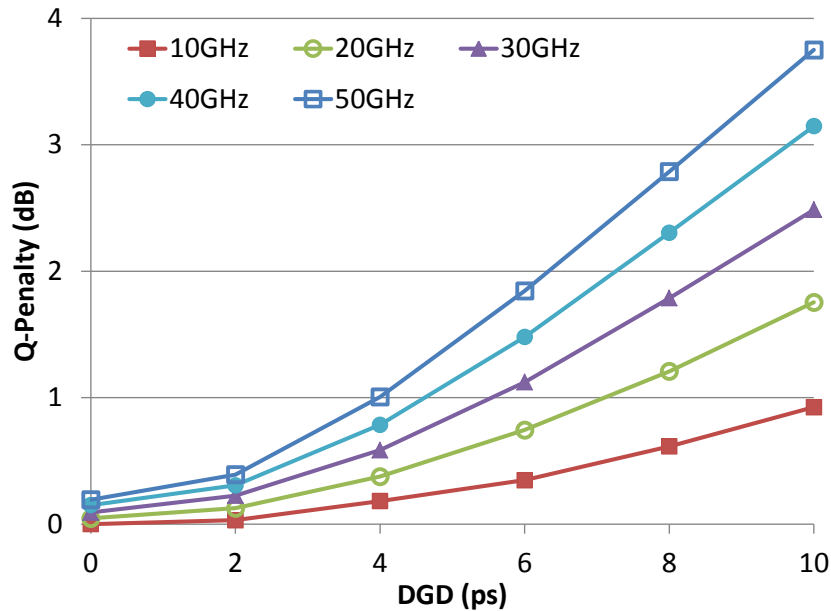


Figure 6.15 PMD induced Q penalty as a function of DGD at BER level of 10^{-3} . The curves are for different optical bandwidth.

6.6 Comparison between different self-coherent subsystems

In this section, we summarize the self-coherent detection subsystems discussed in Chapter 5 and 6. We present some experiment results in Table IV to show the feasibility of SCOH to undertake >100G and transmission over >100 km standard single mode fiber (SSMF), to prove the advantages of “coherent” detection in short reach applications we mentioned in Section 2.5.

The table IV indicates the improvement trend of spectral efficiency (SE) of SCOH subsystems. We normalize the SE to that of the single polarization coherent detection (as 100%). Early SCOH use extra bandwidth needs to be reserved for the SSBN [125], leading to the optical SE of 50%. Later, the iterative SSBN cancellation [127] avoids the frequency gap, increases the SE to 100%. BPS [130] and SCI [132] DD waste the optical SE, but increase the RF bandwidth (BW) utilization ratio at receiver to 100%, because they recover the DSB signal. SV-DD for the first time improves both the SE and RF BW ratio to 100%. The difference of SCOH hardware expense is mainly contributed by the number of photo-detectors. The balanced receiver increases the receiver cost, but improve the SE and simplify the DSP (especially the SSBN cancellation) compared with the single photo-detection based SCOH.

SCOH subsystems support the transmission over several hundred kilometers. In such systems, the amplifier spontaneous emission noise (ASE) dominates the noise source instead of the photo-detection noise. Thus, the system OSNR sensitivity is selected as the evaluation metric instead of the receiver sensitivity. We conduct several 100-Gb/s back-to-back simulations to measure the SCOH receiver sensitivity [62], as shown in Figure 6.16. As we mentioned in Chapter 5, the single-ended PD based SCOH requires a high carrier-to-signal power ratio (CSPR) to suppress the SSBN [130]. However, after applying the balance receiver to subtract the SSBN by optical hardware, the system optimal CSPR decreases to 0 dB [67]. We can observe a dramatic OSNR sensitivity improvement when balanced receiver is applied to SCOH systems. Small CSPR enhances the power of effective signal at transmitter; during transmission, the signal is much more immune to the optical noise; therefore, the receiver OSNR sensitivity improves dramatically.

Table IV. Experiments with self-coherent subsystems










Scheme [Ref.]	Speed (Gbps)	Distance (km)	SB	SSBN cancellation	Optical spectrum
Offset-SSB [125]	-	-	SSB	Frequency gap	
OFDM subc. interleaved [126]	10	260	SSB	Frequency gap	
Virtual SSB [127]	10	340	SSB	Iterative algorithm	
BPS-DD [130]	40	80	DSB	Iterative algorithm	
SCI-DD [132]	100	80	DSB	Balanced receiver	
DP-SCI-DD [133]	-	-	DSB	Balanced receiver	
POL-MUX DD [131]	100	500	SSB	Balanced receiver	
SV-DD [70]	1000	480	DSB	Balanced receiver	
Superchannel SSB [128]	214	720	SSB	Frequency gap	

Table IV (cont.)

Scheme [Ref.]	Optical SE (%)	RF BW ratio (%)	Mod.	PD	Detection dimension
Offset-SSB [125]	50	25	1 IM	1	1
OFDM subc. interleaved [126]	50	25	1 I/Q	1	1

Virtual SSB [127]	100	50	1 I/Q	1	1
BPS-DD [130]	50	100	1 I/Q	1	1
SCI-DD [132]	66.7	100	1 I/Q	2B	2
DP-SCI-DD [133]	100	100	1 I/Q	2B	2
POL-MUX DD [131]	100	25	2 I/Q	4B	4
SV-DD [70]	100	100	1 I/Q	3B	3
Superchannel SSB [128]	~100	<25	Multi. IM	Multi.	1

SB: sideband; SSB: single sideband; DSB: double sideband; SE: spectral efficiency with reference to the single polarization coherent detection; RF BW ratio: the RF bandwidth utilization ratio at receiver (100% ratio means the receiver recovers a DSB signal without frequency gap); subc.: subcarrier; Mod.: modulation; IM: intensity modulator; PD: photo-detector (the letter 'B' at this column means the PD is balanced one).

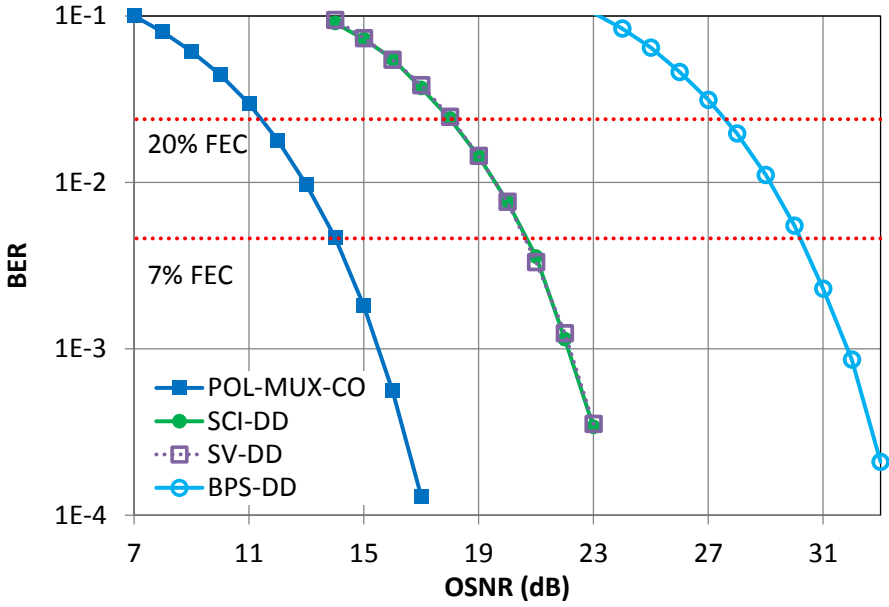


Figure 6.16 OSNR sensitivity comparison among 100G SCOH systems. 7% FEC: hard decision FEC threshold of 3.8×10^{-3} ; 20% FEC: soft-decision FEC threshold of 2.4×10^{-2} .

Compared with coherent detection, SCOH has the following advantages:

- (1) The optical hardware is greatly simplified, especially for receiver. SCOH does not require the LO, which is always expensive in coherent system due to its low linewidth and wide tunable range. Moreover, while dual polarization receiver is essential in coherent system for 2x2 MIMO polarization recovery, single polarization can be an option of SCOH, which aligns the polarizations of signal and carrier at transmitter.

- (2) Receiver requires less DSP. Without LO, there is no need to perform the sophisticated 2-stage carrier recovery which includes frequency offset and phase noise estimation.
- (3) SCOH can be uncooled. Coherent system needs to tightly control the laser wavelength at both transmitter and receiver. Coolers consume large power, and are too bulky to be integrated. In contrast, SCOH automatically aligns carrier and signal wavelength at transceiver.

SCOH offers great superiority beyond conventional IM-DD while maintains cost-efficiency for short and medium reach applications, which bridges the gap between the IM-DD and sophisticated coherent technology.

6.7 Conclusions

This chapter investigates the self-coherent detection in Stokes space. By placing signal and carrier to the 2 orthogonal polarizations, Stokes vector detection subsystems completely linearizes the direct detection optical channel, which realizes the direct detection closet to the coherent technology.

This chapter contains published contents from Ref. [62] [70] [137] and [148]. The thesis author is the primary author of the publications and has contributed more than 50 per cent of the work.

7. MULTI-DIMENSION POLARIZATION MODULATION

Stokes vector receiver (SV-R) was first proposed for the self-coherent detection, as presented in chapter 6. By linearizing the direct detection channel, Stokes vector direct detection (SV-DD) possesses superior performance over conventional DD subsystems:

- Chromatic dispersion can be electrically compensated, which effectively elongates the transmission distance.
- System OSNR sensitivity is only 6-dB away from the standard coherent system, which indicates its capability to handle >1000-km SSMF transmission.
- The RF device bandwidth utilization ratio is 100%, which is critical to maintain the low-cost feature of short-reach applications.
- The powerful DSP technology, which has been successfully applied to current coherent system to compensate fiber impairments, can be transplanted gracefully to direct detection system.

The self-coherent SV-DD is the direct detection closest to the coherent technology.

Soon after the first experiment demonstration of SV-DD system, researchers found out that the SV-R can be a powerful tool to increase the spectral efficiency of intensity modulation – direct detection (IM-DD) system, due to its 3-D detection capability. The Stokes space has 3 dimensions, which contain intensity information along 3 orthogonal polarizations. The Stokes space transmitter can perform 2-D or even 3-D polarization modulation in Poincare sphere, which double or even triple the IM-DD spectral efficiency. Multi-dimension IM-DD is very attractive in industry for very-short-reach applications (transmission Cat. I in Table I), such as the data center intra-connection and mobile convergence. Combined with the coarse-WDM (CWDM), it can cost-efficiently replace the bulky “fiber bundle” to a single optical fiber link.

Generally, the multi-dimension IM-DD using SV-R can no longer be regarded as a “coherent detection” concept, because it does not include an optical reference to detect the light phase. Its channel model is not linear to the optical field, but rather linear to the optical intensity. This channel is sensitive to the chromatic dispersion (CD) impairment, limiting its application to Cat. I in Table I (without the transmitter CD pre-compensation). However, the polarization modulation in Stokes space still utilizes the coherence between the two polarizations within the 2nd and 3rd elements of Stokes vector. For example, even in a POL-MUX IM system where the signal is modulated only on S_0 and S_1 , SV-R should recover the entire Stokes vector to retrieve all the modulated information. As such, multi-dimension polarization modulation in Stokes space could be

treated as the primary step of bringing coherent technology into the very-short-reach optical interconnect for the first time.

7.1 Multi-dimension Stokes-space modulation (SSM)

The Stokes space can modulate the signal from 1-D up to 3-D. In chapter 6, to linearize the optical channel [62], Figure 7.1(a) modulate only X polarization with the complex signal (S) while send the Y polarization as a constant carrier (C). The SV-R uses $S_2 + iS_3 = S \cdot C^*$ to recover a phase diverse signal. This is a typical 2-D SSM format. Another 2-D SSM in Figure 7.1(b) sends the polarization-multiplexed (POL-MUX) IM signal. The SV-R uses S_0 and S_1 to recover the intensity of the two polarizations. Previously, the POL-MUX IM-DD system requires the hardware supported polarization tracking, which is costly and limited by the polarization variation speed. In contrast, the SV-R technology brings the DSP enabled polarization demultiplexing in Stokes space, which offers a low-cost and powerful polarization recovery solution for short reach applications.

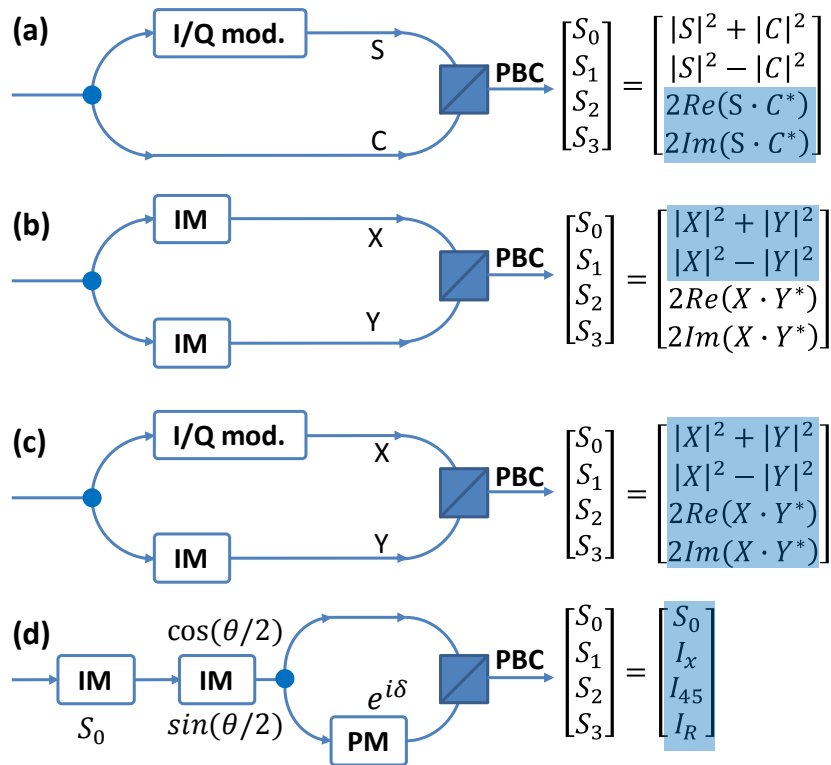


Figure 7.1 Transmitter structure for the SV-DD using (a) self-coherent complex modulation; (b) POL-MUX intensity modulation (IM); (c) X-POL complex modulation and Y-POL intensity modulation; (d) 3-D modulation in Stokes space with polar coordinates (S_0, θ, δ). PM: phase modulator; PBC: polarization beam combiner. The shaded elements of the Stokes vector are applied to recover the signal in SV-R.

To maximize the spectral efficiency, SSM can at most perform 3-D modulation as shown in Figure 7.1(c) [139]. The X polarization is complex modulated while Y is intensity modulated. SV-R recovers the complex value X and intensity $|Y|$. Another 3-D modulation in Stokes space uses the polar coordinates (S_0, θ, δ) in Figure 7.1(d) [72].

The first intensity modulator (IM) modulates the signal intensity S_0 . The second IM splits the signal into two output ports with an arbitrary splitting ratio of $\tan(\theta / 2)$. The phase modulator (PM) gives the phase difference δ between the split signals. Signals after the polarization beam combiner (PBC) forms the Stokes vector:

$$\begin{bmatrix} S_1 \\ S_2 \\ S_3 \end{bmatrix} = S_0 \cdot \begin{bmatrix} \cos \theta \\ \sin \theta \cos \delta \\ \sin \theta \sin \delta \end{bmatrix} \quad (7-1)$$

7.2 Revisit polarization demultiplexing: a universal MIMO perspective

Polarization demultiplexing is a crucial issue for the digital SV-R technology, considering the SV-DD exploits the polarization diversity. In section 6.2, we have proposed various polarization demultiplexing algorithms specially designed for the self-coherent SSM format. After the SSM concept is generalized as the multi-dimension polarization modulation in section 7.1, we briefly retrospect these algorithms to determine whether they are still suitable for other SSM formats.

At the first glance, the most straightforward method for polarization estimation is to send basis vectors in Stokes space: (1,0,0), (0,1,0), (0,0,1). Nevertheless, it has the following drawbacks. First, the training sequence is no longer the signal constellations, but 3 fixed polarization states. Second, the SSM transmitter is required to be capable of sending 3 basis vectors, namely, the capability of controlling the output phase of dual polarizations. This normally requires a shared single laser source for dual polarizations, and at least one phase modulator at SSM transmitter, which means an external I/Q modulator becomes essential. As comparison, very-short reach optical interconnect is dominant by the low-cost transmitter optical subassembly (TOSA).

The geometric method of finding the symmetric axis of constellations in Poincare sphere seems to be an easily-understood approach. However, the symmetric axis exists only for special signal distributions, namely, special modulation constraints of the polarizations, as we deduced in section 6.2.B.

In fact, a generalized polarization demultiplexing can be derived from section 6.3. The SV-R based direct detection channel is a linear 3×3 channel. By treating this channel as a general 3×3 real-value MIMO, there is no need to resort to any special polarization demultiplexing algorithms. To further understand this point, we should completely get rid of the Jones-Stokes conversion in Eq. (2-6), and the dual polarization illustration in Figure 7.1. Instead, the signal now should be regarded as being modulated in the 3-D Stokes space directly, and correspondingly, detected by the 3-D SV-R which recovers the optical signal in the same 3-D Stokes space. This linear MIMO channel is characterized by a 3×3 real-value matrix. Each element of the matrix can either be single-tap only, like

the training results from the basis vectors method in section 6.1.A; or be multiple taps to depict the frequency domain channel characteristics. This matrix can be estimated by various common methods, such as adaptive algorithms [17], least square method [142], or even blind search.

For 3-D SSM format, the above 3×3 MIMO equalization is essential to recover the transmitted polarization states. In terms of 2-D SSM, SV-R still needs to receive all the 3-D information, because the 3×3 channel matrix is always full rank, which spread the 2-D signal to all the 3 dimensions in Stokes space. However, the MIMO equalization can be simplified to 3×2, because only the 2 modulated Stokes vector elements should be picked up as the equalizer outputs. For example, in section 6.2.C, the signal is modulated on S_2 and S_3 , and the corresponding equalizer structure in Figure 6.4 only has 1 complex-value output (namely, 2 real-value outputs).

7.3 Frequency-domain MIMO in Stokes space

The above discussion on the Stoke-space MIMO assumes a time-domain concept of Stokes vector. We now focus on a more complicated modulation: OFDM. OFDM modulation can be realized by the I/Q modulator in Figure 7.1 (a) and (c), or even by the intensity modulator in Figure 7.1 (b) and (c) considering the real-value OFDM (namely, the discrete multitone, DMT) can simply be realized by the Hermitian-symmetric baseband spectrum.

In coherent system, it is common for single-carrier modulation to perform MIMO equalization in time domain based on the signal constellation [17]. In terms of OFDM, because the signal modulation is realized in frequency domain, normally the MIMO equalization is performed after the discrete Fourier transform (DFT) [10]. DFT converts the wide band OFDM signal to multiple low-symbol-rate subcarrier, so that the 1-tap equalizer could be applied per subcarrier for 2×2 MIMO. Correspondingly, in DD SV-R system, time-domain MIMO adaptive equalizers have been demonstrated for the single-carrier QAM [143] and PAM [138] signals. However, unlike coherent OFDM, previous OFDM SSM [69] uses time-domain POL-DEMUX, considering the Stokes parameter is normally regarded as a time-domain concept. In fact, for short-reach link, the polarization mode dispersion (PMD) is normally negligible. The 3×3 RM can be regarded as frequency independent, so that the polarization rotation can be performed after DFT [150]:

$$DFT \left(RM_{3 \times 3} \cdot \begin{bmatrix} S_1 \\ S_2 \\ S_3 \end{bmatrix} \right) = RM_{3 \times 3} \cdot \begin{bmatrix} DFT(S_1) \\ DFT(S_2) \\ DFT(S_3) \end{bmatrix} \quad (7-2)$$

Namely, after recovering the Stokes vector, the digital SV-R first performs DFT, and then estimate RM in frequency domain based on signal constellations.

We take the polarization multiplexed DMT as an example, whose transmitter structure is Figure 7.1(b). The useful Stokes vector elements are S_0 and S_1 . S_0 is independent on polarization variations. Thus, after DFT, the MIMO can be realized per subcarrier via the 1×1 single-input-single-output (SISO) for S_0 , and the 3×1 multi-input-single-output (MISO) for S_1 , as shown in Figure 7.2 below. To simplify POL-DEMUX, equalizer coefficients can be estimated by only a few pilot subcarriers, and other subcarriers directly use these coefficients to retrieve the transmitted S_0 and S_1 .

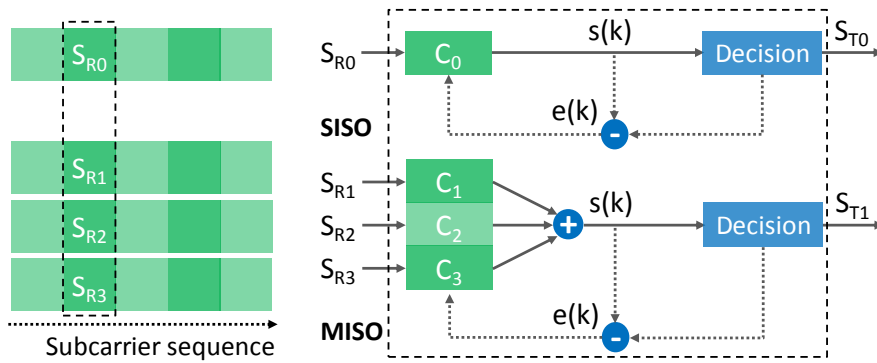


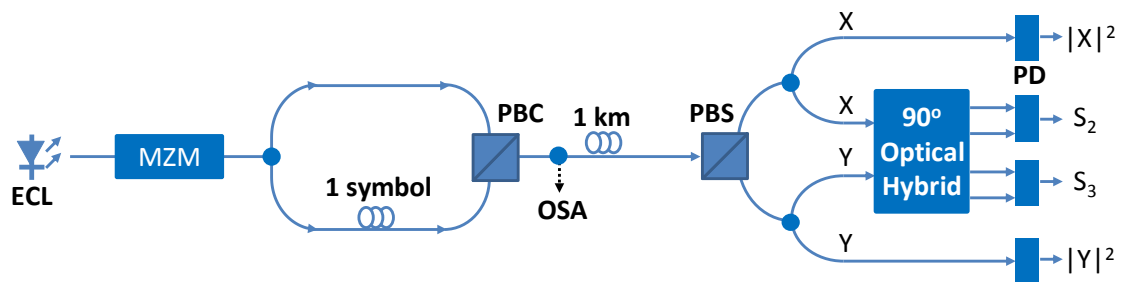
Figure 7.2 Structure of frequency-domain MIMO equalizer for the POL-MUX DMT (an example of adaptive decision-directed mode).

7.4 Polarization-multiplexed discrete multitone experiment

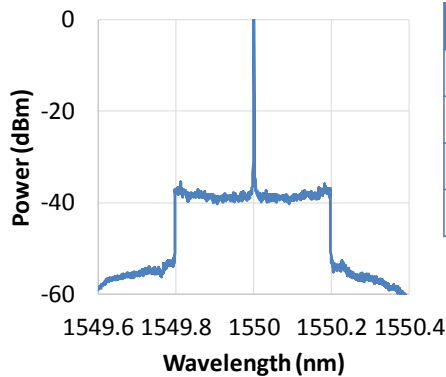
We experimentally demonstrate the OFDM SSM based on frequency domain MIMO using a PM DMT signal [150], with the setup in Figure 7.3. The baseband OFDM signal is modulated with 4-QAM or 16-QAM, with a Hermitian-symmetric spectrum to form a real-value stream. The FFT size is 512 filled with 320 subcarriers. This signal drives an arbitrary waveform generator (AWG) with sampling rate of 80 GSa/s, resulting in a baud-rate of 50 Gbaud and data-rate of 100/200 Gb/s for 4/16-QAM. A linear pre-equalization is performed to compensate the transmitter frequency response. The 1550-nm CW light is intensity-modulated with a 30-GHz MZM, and launched into a PM emulator, which delays the Y-POL by 1 OFDM symbol. It is noted that there is no need to guarantee a single light source for dual polarizations in practice, which means 2 independent transmitter optical subassembly (TOSA) can serve as the sources. The signal optical spectrum is shown in Figure 7.3(i). This signal is transmitted over 1-km single-mode fiber and then launched into a Stokes vector receiver, whose outputs are sampled by the 33-GHz 80-GSa/s oscilloscope. The offline DSP first performs the FFT, and then the MIMO POL-DEMUX per subcarrier basis. To accelerate the DSP, we pick up 10 (out of 160) pilot subcarriers to calculate MIMO coefficients and apply their average to all the subcarriers. The equalizer contains only 1 tap shown by Figure 7.2. We use the adaptive constant

modulus algorithm (CMA) to estimate the MISO coefficients. Because the transceiver may have small nonlinear response at high bandwidth, CMA is chosen to avoid the undesirable phase influence. After MIMO, the intensity of X and Y polarizations is recovered by Eq. (7-3). The conventional 1-tap OFDM channel equalization is performed for each polarization to remove the linear ISI.

$$\begin{aligned} |X|^2 &= \frac{S_0 + S_1}{2} \\ |Y|^2 &= \frac{S_0 - S_1}{2} \end{aligned} \quad (7-3)$$



(i) OSA Spectrum



(ii)

Tx DSP
QAM mapping
OFDM symbol mapping
Pre-equalization
IFFT and CP adding

(iii)

Rx DSP
OFDM window synchronization
CP removal and FFT
MIMO in Stokes space per subcarrier basis
1-tap channel equalization for each polarization
Symbol decision

Figure 7.3 Experiment setup. Inset (i) optical spectrum at transmitter; (ii) transmitter DSP; (iii) receiver DSP. ECL: external cavity laser; MZM: Mach-Zehnder modulator (biased at the quadrature point); PBC/PBS: polarization beam combiner/splitter; OSA: optical spectrum analyzer; PD: photodiode; CP: cyclic prefix.

The frequency domain MIMO equalization and its effects are shown in Figure 7.4. Figure 7.4 (a-d) illustrate 4-QAM while (e-h) are 16-QAM. To reveal the frequency dependence, we calculate the 3 coefficients for each subcarrier and obtain Figure 7.4 (a) and (d). Regardless of the fluctuation due to the random-noise induced estimation error, these coefficients roughly maintain flat across all the subcarriers, which proves it is reasonable to use the average of pilot subcarriers. Before MIMO, the constellations of $|X|^2$ shown by Figure 7.4 (b) and (f) are smeared out. In contrast, after MIMO, the intensity levels of constellation become distinguishable, shown by the single ring for 4-QAM in Figure 7.4(c) and 3 rings in (g). The constellations become clear after OFDM 1-tap channel equalization in (d) and (h).

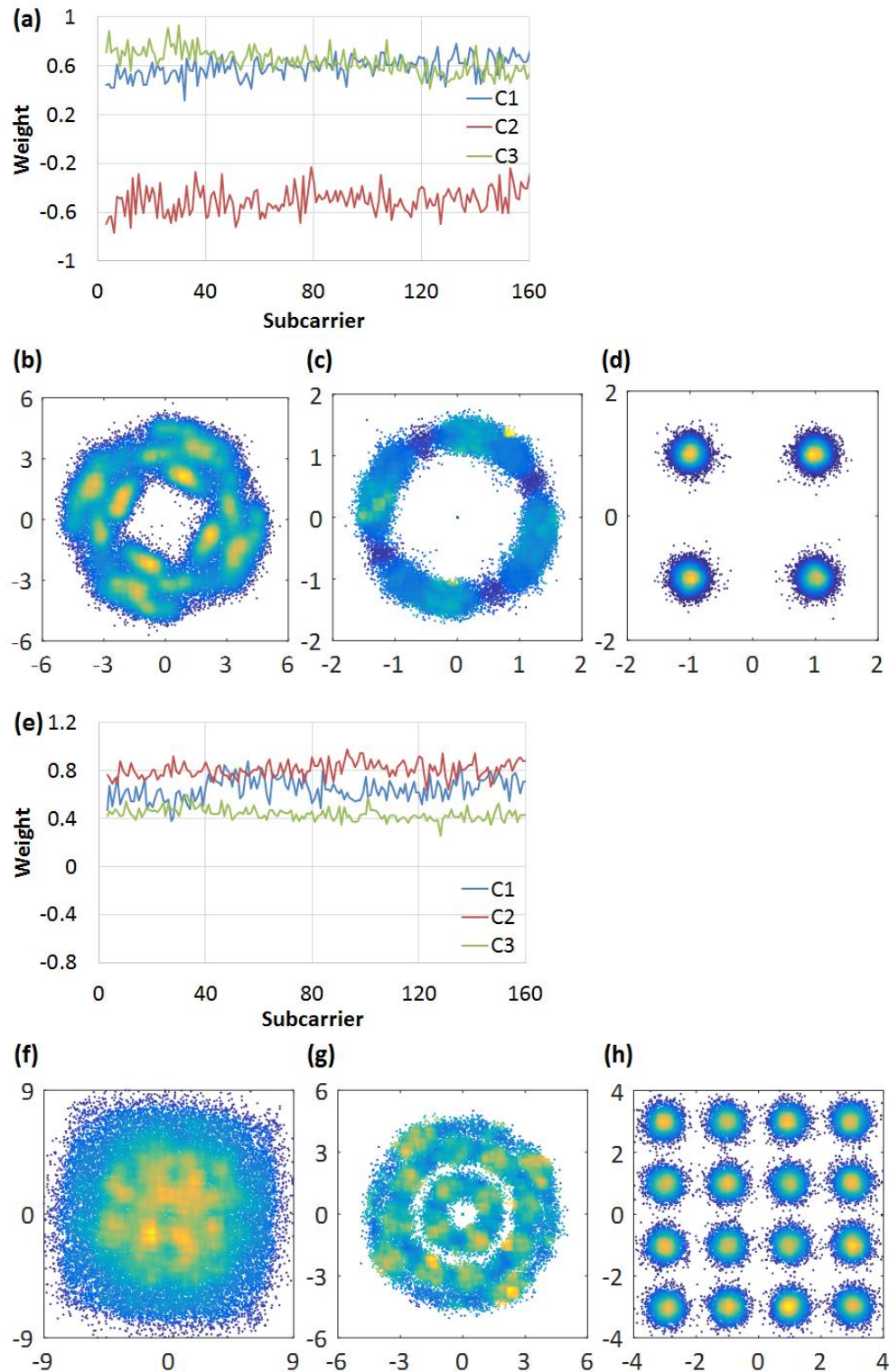


Figure 7.4 Frequency domain MIMO equalization. (a-d) 4-QAM; (e-h) 16-QAM. (a,e) 3x1 equalizer coefficients per subcarrier; received X-POL constellation: (b,f) before MIMO; (c,g) after MIMO; (d,h) after OFDM channel equalization.

Figure 7.5 shows the Q-factor for each subcarrier. A few subcarriers near DC suffers from Q-factor degradation, because of the high near-DC noise as shown near the 0 GHz in Figure 7.3(i). Despite this, all the subcarriers achieve the Q-factor requirement for 7% FEC threshold (around 15 dB for 16-QAM with BER of $4e-3$). The overall Q-factor

difference between the back-to-back and 1-km transmission is less than 0.5 dB. For longer distance, this high baud-rate signal may face severe Q degradation due to the fiber chromatic dispersion. This can be accommodated by either the DMT bit loading or O-band transmission.

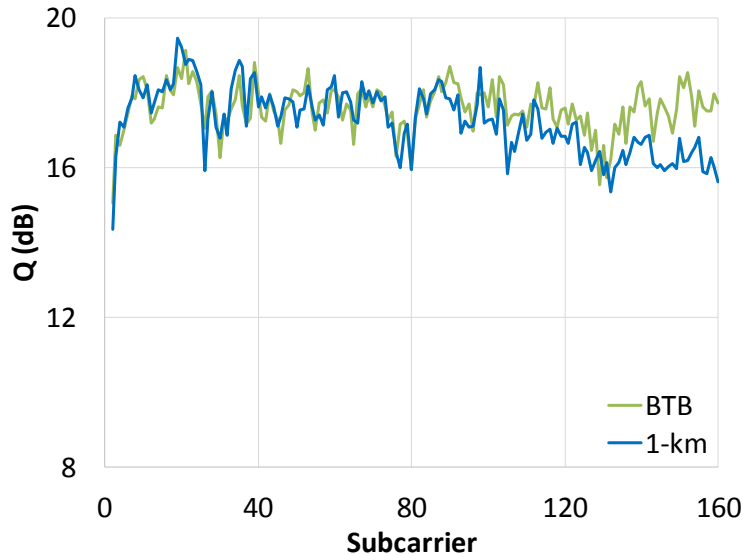


Figure 7.5 Q-factor per subcarrier. BTB: back-to-back.

7.5 Conclusions

This chapter generalizes the Stokes space modulation to multi-dimension polarization modulation, which doubles or even triples the achievable data rate compared with the conventional intensity modulation direct detection system. By regarding the channel in Stokes space as a 3×3 MIMO model, common MIMO equalizations can be applied to the Stokes vector detection system to digitally track the polarization variation.

This chapter contains published contents from Ref. [150]. The thesis author is the primary author of the publication and has contributed more than 50 per cent of the work.

8. SUMMARY

This thesis aims to bring coherent technologies to optical short-reach applications by cost-efficient solutions. In commercial optical communication products, coherent and DM-DD transceivers represents the 2 extremes of system design. Coherent transceivers gather the most advanced optical communication technologies, and offer the maximum achievable optical spectral efficiency and best transmission performance, at the sacrifice of system hardware expense and power consumption. As the counterpart, DM-DD offers the lowest hardware cost and power consumption, which are critical for the cost-sensitive and power-hungry short-reach optical interconnect. To bridge the application window between these two extremes, this thesis gradually modifies the standard coherent transceiver to simpler architectures fitting for various transmission distances.

Chapter 3 begins from the coherent transceiver, but the local oscillator is replaced to a low-cost large-frequency-drift laser. It demonstrates the attempt of exploiting adaptive FEC schemes to compensate the hardware imperfection. To further decrease the laser expense, chapter 4 offers an all-semiconductor-laser coherent transceiver, and the direct modulation of semiconductor laser avoids the sophisticated external modulation technology. Chapter 5 investigates the self-coherent detection without the receiver laser, which endows the simple direct detection receivers with the capability of optical field recovery. Following the self-coherent concept, chapter 6 proposes a simpler receiver structure (compared with the coherent receiver) to exploit fiber polarization diversity. Finally, chapter 7 terminates the hardware simplifications throughout the thesis, by offering a smooth upgrade from DM-DD to the multi-dimension IM-DD using polarization modulation. As a consequence of hardware simplifications, the achievable transmission distance decrease from thousands of km (long-haul, transmission Cat. IV in Table I) in chapter 3 all the way down to less than 10 km (Cat. I) in chapter 7.

Moreover, the thesis contributes the cost reduction from DSP perspective. For example, the self-coherent subsystems in chapter 5 and 6 get rid of the local oscillator. There is no need to the perform sophisticated carrier recovery (including frequency offset and phase noise estimation) for self-coherent detection. Another example is the polarization demultiplexing in chapter 6 and 7. Coherent detection requires the complex-value 2×2 MIMO equalization at receiver to recover the polarization in Jones space. In contrast, Stokes vector detection reduces the equalization dimension to real-value 3×2 (for 2-D modulation) or 3×3 (for 3-D modulation) by recovering the polarization in Stokes space. Table V indicates the contributions (and approaches) of the proposed schemes to overcoming the barriers of DM-DD discussed in Section 1.4.

Table V. Overcoming the DM-DD bottlenecks with the schemes in this thesis

	1-D modulation	Fiber dispersion	Frequency chirp
CH. 3	Field modulation POL-MUX	Coherent detection	External modulation
CH. 4	Complex DM POL-MUX	Coherent detection	Complex DM modulation
CH. 5	Field modulation	Self-coherent detection	External modulation
CH. 6	Field modulation	Self-coherent detection	External modulation
CH. 7	Multi-dimension polarization modulation	-	-

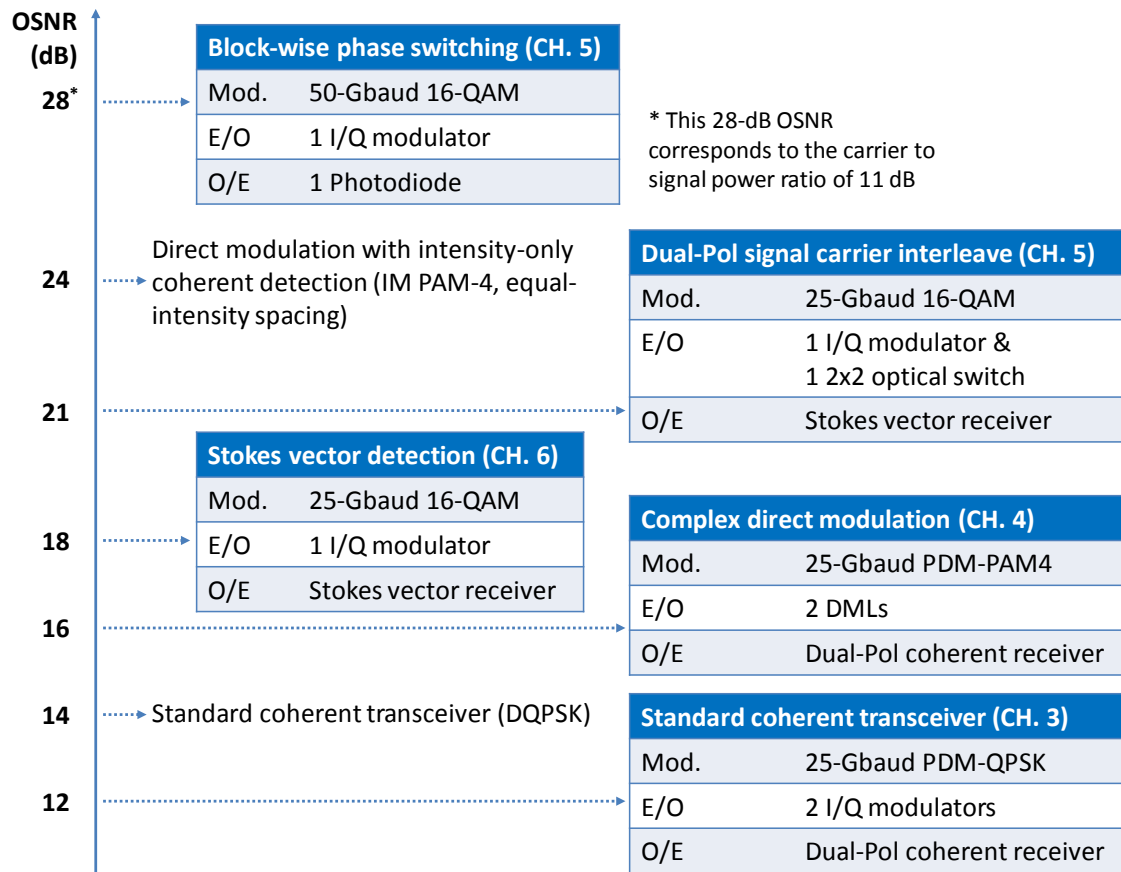


Figure 8.1 OSNR requirements of the 100-Gb/s (raw data-rate) signal at 20% FEC threshold (2.4×10^{-2}). In the figure, the OSNR are approximated values rounded to the integer. E/O: electrical-to-optical conversion; O/E: optical-to-electrical conversion.

Except chapter 7, all the schemes proposed in this thesis realize the signal field recovery by coherent or self-coherent detection. This enables the digital dispersion compensation. Without the dispersion impact, the achievable transmission distance is determined by the system OSNR sensitivity. Section 6.6 has provided the OSNR sensitivity comparison among various self-coherent subsystems. Here, Figure 8.1 summarizes the OSNR sensitivity for the schemes presented in the thesis, characterized by the OSNR requirement for 100-Gb/s (raw data-rate) signal at 20% FEC threshold ($2e-2$). For each system configuration, Figure 8.1 offers an example modulation format to realize 100-Gb/s data rate. After the comprehensive discussions throughout the thesis, Figure 8.1 now clearly explains the reason why the proposed schemes fit for the application ranges illustrated in Figure 1.4.

Besides the breakthrough of the data rate and transmission distance, this thesis also brings novel perspectives to optical communications.

- The self-coherent receiver used to be applied to detect only the optical differential phase (1-D); while here with sacrifice of the time efficiency, it becomes a 2-D receiver recovering both the intensity and phase.
- Moreover, instead of beating the signal with its own delay in conventional self-coherent receiver, the self-coherent concept in this thesis successfully linearizes the direct detection channel by beating the signal with a transmitted carrier.
- The Stokes vector receiver used to be a powerful tool for polarization characterization; while this thesis utilizes it for multiple dimension transmission, and for the first time experimentally demonstrate the >100 Gb/s direct detection in Stokes space.
- The frequency chirp of semiconductor lasers used to be a detrimental factor to the conventional intensity modulation direct detection systems; but when coherent detection is applied, this frequency modulation can be recovered at receiver and converted to phase modulation. The PAM system thus achieves much higher OSNR sensitivity, which becomes suitable to the medium-reach transmission with several hundred kilometres.
- The forward error correction used to be applied to correct the bit error after signal demodulation; while in this thesis, it becomes a powerful DSP tool to compensate the impairment from a specific optical hardware, by using the channel characteristics estimated from the advanced digital coherent detection.

Based on the schemes proposed in this thesis, there are a variety of extended works that can be further investigated in the future. Following are a few examples:

- DSP nowadays is a powerful companion of coherent transceiver. Chapter 3 attempts the advanced FEC to compensate the optical hardware imperfection. This can be further extended to other general DSP technologies. One of the promising schemes is to exploit multi-carrier modulation for the adaptation of colored-SNR optical channel, which allocates various data-rate and FEC to each carrier based on its SNR performance.
- Chapter 4 indicates that the best achievable performance of CDM system has a close relationship with the DML chirp parameters. It is very promising to collaborate with the DML manufacturers to manually control the chirp and achieve the highest system OSNR sensitivity. This will be a promising opportunity to exploit the powerful interaction between optical hardware and advanced DSP.
- Compared with the conventional DM-DD, the self-coherent subsystems as well as the Stokes vector receiver enables better system transmission performance, at the sacrifice of more complicated hardware architecture. This offers a promising opportunity for the photonics integration to significantly decrease the transceiver expense, especially in terms of the integration of these passive optical circuits (without the local oscillator).

By the coherent concept, we throughout reinvent optical short-reach communications. The old paradigms for “short-reach”, such as “1-D modulation”, “on-off-keying”, “very short distance”, “optical dispersion compensation”, “detrimental chirp”, now is completely outdated, except the feature “low cost”. With the on-going cost reduction, coherent technology will no doubt be the future of optical short-reach communications.

ABBREVIATIONS

Acronym	Full Name
ADC	Analog-to-digital converter
ASE	Amplified spontaneous emission
AWG	Arbitrary waveform generator
AWGN	Additive white Gaussian noise
B2B	Back-to-back
B-DPSK	Binary differential phase shift keying
B-E	Blind estimation
B-PD	Balanced photodetector
BER	Bit error rate
BPS	Block-wise phase switching
BW	Bandwidth
CD	Chromatic dispersion
CDM	Complex direct modulation
CM	Complex modulation
CM-DML	Complex modulation of directly modulated laser
CMA	Constant modulus algorithm
COHD	Coherent detection
CP	Cyclic prefix
CW	Continuous wave
CO-OFDM	Coherent optical OFDM
CSPR	Carrier to signal power ratio
DAC	Digital-to-analog converter
DCF	Dispersion compensating fiber
DD	Direct detection
DDO-OFDM	Direct detection optical OFDM
DFB	Distributed feedback (laser)
DGD	Differential group delay
DM	Direct modulation
DML	Directly modulated laser

DMT	Discrete multitone
DP	Dual polarization
DPSK	Differential phase shift keying
DQPSK	Differential quadrature phase shift keying
DSB	Double sideband
DSP	Digital signal processing
DTGC	Discrete time Gaussian channel
DTGC-ISI	DTGC with inter-symbol interference
DTGC-CISI	DTGC with conjugate inter-symbol interference
DWDM	Dense wavelength division multiplexing
EAM	Electro-absorption modulator
ECL	External cavity laser
EDFA	Erbium-doped fiber amplifier
EM	External modulation
FEC	Forward error correction
FFE	Feed-forward equalizer
FFT	Fast Fourier transform
FM	Frequency modulation
FWM	Four-wave mixing
HD	Hard decision
i.i.d.	Independent identically distribution
IFFT	Inverse fast Fourier transform
IM	Intensity modulation
IM-DD	Intensity modulation – direct detection
ISI	Inter-symbol interference
LDPC	Low density parity check
LMS	Least mean square
LO	Local oscillator
LSP	Least square plane
M-DPSK	<i>M</i> -level differential phase shift keying
MIMO	Multiple input multiple output
MLSE	Maximum likelihood sequence estimation
MZM	Mach-Zehnder modulator

NRZ	Non-return to zero
OBM	Orthogonal band multiplexing
OA	Optical amplifier
ODC	Optical dispersion compensation
OF	Optical filter
OFDM	Orthogonal frequency division multiplexing
OOK	On-off-keying
OSA	Optical spectrum analyzer
OSNR	Optical signal-to-noise ratio
PAM	Pulse amplitude modulation
PBC	Polarization beam combiner
PBS	Polarization beam splitter
PD	Photodetector
PDL	Polarization dependent loss
PLL	Phase locked loop
PM	Phase modulation
PMD	Polarization mode dispersion
POL	Polarization
POL-MUX	Polarization multiplexing
POL-DEMUX	Polarization demultiplexing
PON	Passive optical networks
PSK	Phase shift keying
QAM	Quadrature amplitude modulation
QPSK	Quadrature phase shift keying
RF	Radio frequency
RI	Refractive index
RLS	Recursive least square
RM	Rotation matrix
RS	Reed-Solomon (code)
Rx	Receiver
SCI	Signal carrier interleave
SCOH	Self-coherent
SD	Soft decision

SE	Spectral efficiency
SISO	Single input single output
SMF	Single mode fiber
SNR	Signal-to-noise ratio
SOP	State of polarization
SRA	Subcarrier reliability aware
SSMF	Standard single mode fiber
SSB	Single sideband
SSBN	Signal-to-signal beat noise
SV	Stokes vector
SV-DD	Stokes vector direct detection
SV-R	Stokes vector receiver
SW	(Optical) Switch
TA-E	Training aided estimation
TDM	Time-division multiplexing
TDS	Time-domain oscilloscope
TOSA	Transmitter optical sub-assembly
Tx	Transmitter
VA	Viterbi algorithm
VCSEL	Vertical-cavity surface-emitting laser
WDM	Wavelength division multiplexing
WSS	Wavelength selective switch
X-POL	X polarization
Y-POL	Y polarization

BIBLIOGRAPHY

- [1] K. C. Kao and G. A. Hockham, "Dielectric-fiber surface waveguides for optical frequencies," Proceedings of the Institution of Electrical Engineers 113(7), 1151-1158, 1966.
- [2] F. P. Kapron, D. B. Keck, and R. D. Maurer, "Radiation losses in glass optical waveguides," Applied Physics Letters 17, 423-425, 1970.
- [3] R. S. Tucker, "High-speed modulation of semiconductor lasers," IEEE Transactions on Electron Devices 32(12), 2572 – 2584, 1985.
- [4] J. L. Zyskind, C. R. Giles, J. R. Simpson, and D. J. DiGiovanni, "Erbium-doped fiber amplifiers and the next generation of lightwave systems," AT&T Technical Journal 71(1), 53-62, 1992.
- [5] C. R. Davidson, C. J. Chen, M. Nissov, A. Pilipetskii, N. Ramanujam, H. D. Kidorf, B. Pedersen, M. A. Mills, C. Lin, M. I. Hayee, J. X. Cai, A. B. Puc, P. C. Corbett, R. Menges, H. Li, A. Elyamani, C. Rivers, and N. S. Bergano, "1800 Gb/s Transmission of One Hundred and Eighty 10 Gb/s WDM Channels over 7,000 km using the Full EDFA C-Band," Optical Fiber Communication Conference, paper PD25, 2000.
- [6] K. Kikuchi, "Coherent detection of phase-shift keying signals using digital carrier-phase estimation," Optical Fiber Communication Conference, Paper OTu14, 2006.
- [7] S. Zhang, F. Yaman, Y. K. Huang, J. D. Downie, D. Zou, W. Wood, A. R. Zakharian, R. Khrapko, S. Mishra, V. Nazarov, J. E. Hurley, I. Djordjevic, E. Mateo, and Y. Inada, "Capacity-Approaching Transmission over 6375 km at Spectral Efficiency of 8.3 bit/s/Hz," Optical Fiber Communication Conference, paper Th5C.2, 2016.
- [8] Cisco Visual Networking Index, "Global Mobile Data Traffic Forecast Update 2015–2020," white paper, 2015.
- [9] Y. Han, and G. Li, "Coherent optical communication using polarization multiple-input-multiple-output," Optics Express 13(19), 7527-7534, 2005.
- [10] W. Shieh, H. Bao, and Y. Tang, "Coherent optical OFDM: theory and design," Optics Express 16(2), 841-859, 2008.
- [11] X. Liu, S. Chandrasekhar, T. Lotz, P. Winzer, H. Haunstein, S. Randel, S. Corteselli, B. Zhu, and D. Peckham, "Generation and FEC-Decoding of a 231.5-Gb/s PDM-OFDM Signal with 256-Iterative-Polar-Modulation Achieving 11.15-b/s/Hz Intrachannel Spectral Efficiency and 800-km Reach," Optical Fiber Communication Conference, paper PDP5B.3, 2012.
- [12] F. Buchali, G. Böcherer, W. Idler, L. Schmalen, P. Schulte, and F. Steiner, "Experimental demonstration of capacity increase and rate-adaptation by probabilistically shaped 64-QAM," European Conference on Optical Communication, paper PDP3.4, 2015.
- [13] Y. Ma, Q. Yang, Y. Tang, S. Chen, and W. Shieh, "1-Tb/s per Channel Coherent Optical OFDM Transmission with Subwavelength Bandwidth Access," Optical Fiber Communication Conference, paper PDPC1, 2009.
- [14] S. Chandrasekhar, X. Liu, B. Zhu, and D. W. Peckham, "Transmission of a 1.2-Tb/s 24-Carrier No-Guard-Interval Coherent OFDM Superchannel over 7200-km of Ultra-Large-Area Fiber," European Conference on Optical Communication, paper PD2.6, 2009.

- [15] Y. Yamamoto, and T. Kimura, "Coherent optical fiber transmission systems," *IEEE Journal of Quantum Electronics* 17(6), 919-935, 1981.
- [16] O. E. Agazzi, M. R. Hueda, H. S. Carrer, and D. E. Crivelli, "Maximum-likelihood sequence estimation in dispersive optical channels," *Journal of Lightwave Technology* 23(2), 749-763, 2005.
- [17] S. J. Savory, "Digital filters for coherent optical receivers," *Optics Express* 16(2), 804-817, 2008.
- [18] R. Kudo, T. Kobayashi, K. Ishihara, Y. Takatori, A. Sano, and Y. Miyamoto, "Coherent Optical Single Carrier Transmission Using Overlap Frequency Domain Equalization for Long-Haul Optical Systems," *Journal of Lightwave Technology* 27(16), 3721-3728, 2009.
- [19] Z. Zhuang, S. W. Suh, and J. S. Patel, "Polarization controller using nematic liquid crystals," *Optics Letters* 24(10), 694-696, 1999.
- [20] F. Roy, C. Francia, F. Bruyère, and D. Penninckx, "A simple dynamic polarization mode dispersion compensator," *Optical Fiber Communication Conference*, paper TuS4, 1999.
- [21] W. Shieh, "PMD-Supported Coherent Optical OFDM Systems," *IEEE Photonics Technology Letters* 19(3), 134-136, 2007.
- [22] E. Ip, and J. M. Kahn, "Digital Equalization of Chromatic Dispersion and Polarization Mode Dispersion," *Journal of Lightwave Technology* 25(8), 2033-2043, 2007.
- [23] M. A. Grant, W. C. Michie, and M. J. Fletcher, "The performance of optical phase-locked loops in the presence of nonnegligible loop propagation delay," *Journal of Lightwave Technology* 5(4), 592-597, 1987.
- [24] E. Ip, and J. M. Kahn, "Feedforward carrier recovery for coherent optical communications," *Journal of Lightwave Technology* 25(9), 2675-2692, 2007.
- [25] T. Pfau, S. Hoffmann, and R. Noe, "Hardware-Efficient Coherent Digital Receiver Concept With Feedforward Carrier Recovery for M-QAM Constellations," *Journal of Lightwave Technology* 27(8), 989-999, 2009.
- [26] R. J. Essiambre, and R. W. Tkach, "Capacity Trends and Limits of Optical Communication Networks," *Proceedings of the IEEE* 100(5), 1035-1055, 2012.
- [27] Y. Tang, W. Shieh, and B. S. Krongold, "DFT-Spread OFDM for Fiber Nonlinearity Mitigation," *IEEE Photonics Technology Letters* 22(16), 1250-1252, 2010.
- [28] E. Ip, A. P. T. Lau, D. J. F. Barros, and J. M. Kahn, "Compensation of Dispersion and Nonlinear Impairments Using Digital Backpropagation," *Journal of Lightwave Technology* 26(20), 3416-3425, 2008.
- [29] L. B. Du, and A. J. Lowery, "Improved single channel backpropagation for intra-channel fiber nonlinearity compensation in long-haul optical communication systems," *Optics Express* 18(16), 17075-17088, 2010.
- [30] "IEEE P802.3ba 40Gb/s and 100Gb/s Ethernet Task Force," official web site. IEEE. June 19, 2010. Retrieved June 24, 2011.
- [31] E. Haglund, P. Westbergh, J. S. Gustavsson, E. P. Haglund, A. Larsson, M. Geen, and A. Joel, "30 GHz bandwidth 850 nm VCSEL with sub-100 fJ/bit energy dissipation at 25–50 Gbit/s," *Electronics Letters* 51(14), 1096-1098, 2015.

- [32] Y. Matsui, T. Pham, T. Sudo, G. Carey, B. Young, J. Xu, C. Cole, and C. Roxlo, "28-Gbaud PAM4 and 56-Gb/s NRZ Performance Comparison Using 1310-nm Al-BH DFB Laser," *Journal of Lightwave Technology* 34(11), 2677-2683, 2016.
- [33] Y. Matsui, T. Pham, W. Ling, R. Schatz, G. Carey, H. Daghighian, T. Sudo, and C. Roxlo, "55-GHz Bandwidth Short-Cavity Distributed Reflector Laser and its Application to 112-Gb/s PAM-4," *Optical fiber communication conference*, paper Th5B.4, 2016.
- [34] C. Xie, S. Spiga, P. Dong, P. J. Winzer, A. Gnauck, C. Gréus, C. Neumeyr, M. Ortsiefer, M. Müller, and M. Amann, "Generation and transmission of 100-Gb/s PDM 4-PAM using directly modulated VCSELs and coherent detection," *Optical fiber communication conference*, paper Th5C.9, 2014.
- [35] P. Dong, J. Lee, YK. Chen, L. L. Buhl, S. Chandrasekhar, J. H. Sinsky, and K. Kim, "Four-Channel 100-Gb/s per Channel Discrete Multi-Tone Modulation Using Silicon Photonic Integrated Circuits," *Optical fiber communication conference*, paper Th5B.4, 2015.
- [36] S. Lange, S. Wolf, J. Lutz, L. Altenhain, R. Schmid, R. Kaiser, C. Koos, S. Randel, and M. Schell, "100 GBd Intensity Modulation and Direct Detection with an InP-based Monolithic DFB Laser Mach-Zehnder Modulator," *Optical fiber communication conference*, paper Th5C.5, 2017.
- [37] S. Kanazawa, H. Yamazaki, Y. Nakanishi, T. Fujisawa, K. Takahata, Y. Ueda, W. Kobayashi, Y. Muramoto, H. Ishii, and H. Sanjoh, "Transmission of 214-Gbit/s 4-PAM signal using an ultra-broadband lumped-electrode EADFB laser module," *Optical fiber communication conference*, paper Th5B.3, 2016.
- [38] G. P. Agrawal, "Effect of frequency chirping on the performance of optical communication systems," *Optics Letters* 11(5), 318-320, 1986.
- [39] B. W. Hakki, "Evaluation of transmission characteristics of chirped DFB lasers in dispersive optical fiber," *Journal of Lightwave Technology* 10(7), 964-970, 1992.
- [40] T. Lengyel, K. Szczerba, M. Karlsson, A. Larsson, and P. Andrekson, "Demonstration of a 71.8 Gbps 4-PAM 850 nm VCSEL-based Link with a Pre-emphasizing Passive Filter," *European conference on optical communication*, 2016.
- [41] Y. Matsui, D. Mahgerefteh, X. Zheng, C. Liao, Z. F. Fan, K. McCallion, and P. Tayebati, "Chirp-Managed Directly Modulated Laser (CML)," *IEEE Photonics Technology Letters* 18(2), 385-387, 2006.
- [42] Z. Li, L. Yi, H. Ji, and W. Hu, "100-Gb/s TWDM-PON based on 10G optical devices," *Optics Express* 24(12), 12941-12948, 2016.
- [43] L. Xue, L. Yi, H. Ji, P. Li, and W. Hu, "First Demonstration of Symmetric 100G-PON in O-band with 10G-Class Optical Devices Enabled by Dispersion Supported Equalization," *Optical fiber communication conference*, paper M3H.1, 2017.
- [44] A. Lender, "The Duobinary Technique for High-Speed Data Transmission," *Transactions of the American Institute of Electrical Engineers* 82(2), 214-218, 1963.
- [45] L. Suhr, J. J. V. Olmos, B. Mao, X. xu, G. N. Liu, and I. T. Monroy, "Direct modulation of 56 Gbps duobinary-4-PAM," *Optical Fiber Communication Conference*, paper Th1E.7, 2015.
- [46] D. V. Veen, V. E. Houtsma, and P. Winzer, and Peter Vetter, "26-Gbps PON Transmission over 40-km using Duobinary Detection with a Low Cost 7-GHz APD-Based Receiver," *European Conference on Optical Communication*, paper Tu.3.B.1, 2012.

- [47] K. Yonenaga and S. Kuwano, "Dispersion-tolerant optical transmission system using duobinary transmitter and binary receiver," *Journal of Lightwave Technology* 15(8), 1530-1537, 1997.
- [48] Y. Kai, M. Nishihara, T. Tanaka, T. Takahara, L. Li, Z. Tao, B. Liu, J. C. Rasmussen, and T. Drenski, "Experimental comparison of pulse amplitude modulation (PAM) and discrete multi-tone (DMT) for short-reach 400-Gbps data communication," *European Conference on Optical Communication*, paper Th.1.F.3, 2013.
- [49] H. Zhang, S. Fu, J. Man, W. Chen, X. Song, and L. Zeng, "30km Downstream Transmission Using 4x25Gb/s 4-PAM Modulation with Commercial 10Gbps TOSA and ROSA for 100Gb/s-PON," *Optical Fiber Communication Conference*, paper M21.3, 2014.
- [50] Q. Zhang, N. Stojanovic, C. Prodaniuc, F. Karinou, and C. Xie, "Cost-effective single-lane 112 Gb/s solution for mobile fronthaul and access applications," *Optics Letters* 41(24), 5720-5723, 2016.
- [51] D. R. Morgan, Z. Ma, J. Kim, M. G. Zierdt, and J. Pastalan, "A Generalized Memory Polynomial Model for Digital Predistortion of RF Power Amplifiers," *IEEE Transactions on Signal Processing* 54(10), 3852-3860, 2006.
- [52] X. Li, S. Zhou, H. Ji, M. Luo, Q. Yang, Y. Lilin, R. Hu, C. Li, S. Fu, A. Arokiaswami, W. D. Zhong, and C. Yu, "Transmission of 4x28-Gb/s PAM-4 over 160-km Single Mode Fiber using 10G-Class DML and Photodiode," *Optical Fiber Communication Conference*, paper W1A.5, 2016.
- [53] G. D. Forney, "Maximum-likelihood sequence estimation of digital sequences in the presence of intersymbol interference," *IEEE Transactions on Information Theory* 18(3), 363-378, 1972.
- [54] H. Bülow, F. Buchali, and A. Klekamp, "Electronic Dispersion Compensation," *Journal of Lightwave Technology* 26(1), 158-167, 2008.
- [55] J. McNicol, M. O'Sullivan, K. Roberts, A. Comeau, D. McGhan, and L. Strawczynski, "Electronic Domain Compensation of Optical Dispersion," *Optical Fiber Communication Conference and Exposition and The National Fiber Optic Engineers Conference*, paper OThJ3, 2005.
- [56] F. Ouellette, P. A. Krug, T. Stephens, G. Dhosi, and B. Eggleton, "Broadband and WDM dispersion compensation using chirped sampled fibre Bragg gratings," *Electronics Letters* 31(11), 899-901, 1995.
- [57] Z. Pan, Y. W. Song, C. Yu, Y. Wang, Q. Yu, J. Popelek, H. Li, Y. Li, and A. E. Willner, "Tunable Chromatic Dispersion Compensation in 40-Gb/s Systems Using Nonlinearly Chirped Fiber Bragg Gratings," *Journal of Lightwave Technology* 20(12), 2239-2246, 2002.
- [58] S. Chandrasekhar, C. R. Doerr, L. L. Buhl, D. Mahgerefteh, Y. Matsui, B. Johnson, C. Liao, X. Zheng, K. McCallion, Z. Fan, and P. Tayebati, "Flexible transport at 10-Gb/s from 0 to 675km (11,500ps/nm) using a chirp-managed laser, no DCF, and a dynamically adjustable dispersion-compensating receiver," *Optical Fiber Communication Conference*, paper PDP30, 2005.
- [59] S. C. J. Lee, F. Breyer, S. Randel, H. P. A. van den Boom, and Antonius M. J. Koonen, "High-speed transmission over multimode fiber using discrete multitone modulation," *Journal of Optical Networking* 7(2), 183-196, 2008.
- [60] R. Puerta, M. Agustin, L. Chorchos, J. Tonski, J.-R. Kropp, N. Ledentsov, V. A. Shchukin, N. N. Ledentsov, R. Henker, I. T. Monroy, J. J. V. Olmos, and J. P. Turkiewicz, "107.5 Gb/s 850 nm multi- and single-mode VCSEL transmission over 10 and 100 m of multi-mode fiber," *Optical Fiber Communication Conference*, paper Th5B.5, 2016.

- [61] G. Meslener, "Chromatic dispersion induced distortion of modulated monochromatic light employing direct detection," *IEEE Journal of Quantum Electronics* 20(10), 1208-1216, 1984.
- [62] D. Che, Q. Hu, and W. Shieh, "Linearization of Direct Detection Optical Channels using Self-Coherent Subsystems," *Journal of Lightwave Technology* 34(2), 516-524, 2016.
- [63] Osinski, and J. Buus, "Linewidth broadening factor in semiconductor lasers--An overview," *IEEE Journal of Quantum Electronics* 23(1), 9-29, 1987.
- [64] J. M. Tang, and K.A. Shore, "30-gb/s signal transmission over 40-km directly modulated DFB-laser-based single-mode-fiber links without optical amplification and dispersion compensation," *Journal of Lightwave Technology* 24(6), 2318-2327, 2006.
- [65] W. Shieh, H. Khodakarami, and D. Che, "Polarization diversity and modulation for high-speed optical communications," *APL Photonics* 1, 040801, 2016.
- [66] X. Liu, S. Chandrasekhar, and A. Leven, "Digital self-coherent detection," *Optics Express* 16(2), 792-803, 2008.
- [67] X. Chen, D. Che, A. Li, J. He, and W. Shieh, "Signal-carrier interleaved optical OFDM for direct detection optical communication," *Optics express* 21(26), 32501-32507, 2013.
- [68] J. P. Gordon, and H. Kogelnik, "PMD fundamentals: Polarization mode dispersion in optical fibers," *Proceedings of the National Academy of Sciences of the United States of America* 97(9), 4541-4550, 2000.
- [69] D. Che, A. Li, X. Chen, Q. Hu, Y. Wang, and W. Shieh, "160-Gb/s Stokes vector direct detection for short reach optical communication," *Optical Fiber Communication Conference*, paper Th5C.7, 2014.
- [70] D. Che, A. Li, X. Chen, Q. Hu, Y. Wang, and W. Shieh, "Stokes Vector Direct Detection for Linear Complex Optical Channels", *Journal of Lightwave Technology* 33(3), 678-684, 2015.
- [71] D. Che, A. Li, Q. Hu, X. Chen, and W. Shieh, "Implementing Simplified Stokes Vector Receiver for Phase Diverse Direct Detection", *Optical Fiber Communication Conference*, paper Th1E.4, 2015.
- [72] K. Kikuchi, and S. Kawakami, "Multi-level signaling in the Stokes space and its application to large-capacity optical communications," *Optics Express* 22(7), 7374-7387, 2014.
- [73] I. B. Djordjevic, M. Cvijetic, L. Xu, and T. Wang, "Using LDPC-Coded Modulation and Coherent Detection for Ultra Highspeed Optical Transmission," *Journal of Lightwave Technology* 25(11), 3619-3625, 2007.
- [74] I. B. Djordjevic, M. Arabaci, and L. L. Minkov, "Next Generation FEC for High-Capacity Communication in Optical Transport Networks," *Journal of Lightwave Technology* 27(16), 3518-3530, 2009.
- [75] H. Bülow, and E. S. Masalkina, "Coded Modulation in Optical Communications," *Optical Fiber Communication Conference*, paper OTh01, 2011.
- [76] T. Mizuochi, Y. Miyata, K. Kubo, T. Sugihara, K. Onohara, and H. Yoshida, "Progress in Soft-Decision FEC", *Optical Fiber Communication Conference*, paper NWC2, 2011.
- [77] F. Chang, K. Onohara, and T. Mizuochi, "Forward Error Correction for 100 G Transport Networks," *IEEE Communications Magazine* 48(3), S48-S55, 2010.
- [78] Q. Yang, Y. Ma, and W. Shieh, "107 Gb/s coherent optical OFDM reception using orthogonal band multiplexing," *Optical Fiber Communication Conference*, paper PDP7, 2008.

- [79] J. Luo, A. Kortke, and W. Keusgen, "Efficient Channel Estimation Schemes for MIMO OFDM Systems with NULL Subcarriers," Vehicular Technology Conference, 2008.
- [80] B. G.Lindsay, K. A.Smith, and F. B. Dunning, "Control of long-term output frequency drift in commercial dye lasers," Review of Scientific Instruments 62(6), 1656-1657, 1991.
- [81] Y. Muroya, T. Nakamura, H. Yamada, and T. Torikai, "Precise wavelength control for DFB laser diodes by novel corrugation delineation method," IEEE Photonics Technology Letters 9(3), 288-290, 1997.
- [82] W. D. Grover, "Forward error correction in dispersion-limited lightwave systems," Journal of Lightwave Technology 6(5), 643-654, 1988.
- [83] S. Yamamoto, H. Takahira, and M. Tanaka, "5 Gbit/s Optical Transmission Terminal Equipment using Forward Error Correcting Code and Optical Amplifier," Electronics Letters 30(3), 254-255, 1994.
- [84] R. Gallager, "Low-density parity-check codes," IRE Transactions on Information Theory 8(1), 21-28, 1966.
- [85] D. J. C. MacKay, and R. M. Neal, "Near Shannon limit performance of low density parity check codes," Electronics Letters 32(18), 1645-1646, 1996.
- [86] D. Che, H. Khodakarami, A. Li, X. Chen, T. Anderson and W. Shieh, "Subcarrier reliability aware soft-decision LDPC code in CO-OFDM systems," IEEE Photonics Technology Letters 26(11), 1157-1160, 2014.
- [87] F. R. Kschischang, B. J. Frey, and H. A. Loeliger, "Factor Graphs and the Sum-Product Algorithm," IEEE Transactions on Information Theory 47(2), 498-519, 2001.
- [88] J. Zhao, F. Zarkeshvari, and A. H. Banihashemi, "On implementation of min-sum algorithm and its modifications for decoding low-density Parity-check (LDPC) codes," IEEE Transactions on Communications 53(4), 549-554, 2005.
- [89] M. P. C. Fossorier, "Quasicyclic low-density parity-check codes from circulant permutation matrices," IEEE Transactions on Information Theory 50(8), 1788-1793, 2004.
- [90] S. Y. Chung, T. J. Richardson, and R. L. Urbanke, "Analysis of Sum-Product Decoding of Low-Density Parity-Check Codes Using a Gaussian Approximation," IEEE Transactions on Information Theory 47(2), 657-670, 2001.
- [91] Q. Yang, W. Shieh, and Y. Ma, "Bit and Power Loading for Coherent Optical OFDM," IEEE Photonics Technology Letter 20(15), 1305-1307, 2008.
- [92] C. Xie, "WDM coherent PDM-QPSK systems with and without inline optical dispersion compensation," Optics Express 17(6), 4815-4823, 2009.
- [93] Z. Liu, J. Kakande, B. Kelly, J. O'Carroll, R. Phelan, D. J. Richardson, and R. Slavík, "Modulator-free quadrature amplitude modulation signal synthesis," Nature Communications 10, article 6911, 2014.
- [94] D. Che, Q. Hu, F. Yuan, and W. Shieh, "Enabling Complex Modulation Using the Frequency Chirp of Directly Modulated Lasers," European Conference on Optical Communication, paper Mo.4.5.3, 2015.
- [95] Q. Hu, D. Che, Y. Wang, A. Li, J. Fang, and W. Shieh, "Beyond amplitude-only detection for digital coherent system using directly modulated laser," Optics Letters 40(12), 2762-2765, 2015.

- [96] I. N. Cano, A. Lerín, and J. Prat, "DQPSK Directly Phase Modulated DFB for Flexible Coherent UDWDM-PONs," *IEEE Photonics Technology Letters* 28(1), 35-38, 2016.
- [97] D. Che, F. Yuan, Q. Hu, and W. Shieh, "Frequency chirp supported complex modulation of directly modulated lasers," *Journal of Lightwave Technology* 34(8), 1831-1836, 2016.
- [98] D. Che, F. Yuan, and W. Shieh, "Towards high-order modulation using complex modulation of semiconductor lasers," *Optics Express* 24(6), 6644-6649, 2016.
- [99] A. P. Lathi, and Z. Ding, "Modern Digital and Analog Communication Systems," Oxford University Press, 2009.
- [100] R. S. Vodhanel, A. F. Elrefaie, M. Z. Iqbal, R. E. Wagner, J. L. Gimlett, and S. Tsuji, "Performance of Directly Modulated DFB Lasers in 10-Gb/s ASK, FSK, and DPSK Lightwave Systems," *Journal of Lightwave Technology* 8(9), 1379-1386, 1990.
- [101] D. Che, F. Yuan, H. Khodakarami, and W. Shieh, "Duobinary pulse shaping for frequency chirp enabled complex modulation," *Optics Letters* 41(17), 3968-3971, 2016.
- [102] C. Harder, K. Vahala, and A. Yariv, "Measurement of the linewidth enhancement factor α of semiconductor lasers," *Applied Physics Letter* 42(4), 328-330, 1983.
- [103] M. Osinski, and J. Buus, "Linewidth broadening factor in semiconductor lasers--An overview," *IEEE Journal of Quantum Electronics* 23(1), 9-29, 1987.
- [104] Y. Yu, G. Giuliani, and S. Donati, "Measurement of the linewidth enhancement factor of semiconductor lasers based on the optical feedback self-mixing effect," *IEEE Photonics Technology Letters* 16(4), 990-992, 2004.
- [105] F. Yuan, D. Che, Q. Hu, and W. Shieh, "Characterization of Thermal Frequency Modulation of a DFB Laser Using Digital Coherent Detection," *Optical Fiber Communication Conference*, paper W2A.25, 2016.
- [106] G. D. Forney, "The Viterbi algorithm," *Proceedings of the IEEE* 61(3), 268-278, 1973.
- [107] F. Breyer, S. C. J. Lee, S. Randel, and N. Hani, "PAM-4 signalling for gigabit transmission over standard step-index plastic optical fibre using light emitting diodes," *European Conference on Optical Communication*, paper We.2.A.3, 2008.
- [108] K. Zhong, W. Chen, Q. Sui, J. Man, A. P. Lau, C. Lu, and L. Zeng, "Experimental Demonstration of 500Gbit/s Short Reach Transmission Employing PAM4 Signal and Direct Detection with 25Gbps Device," *Optical Fiber Communication Conference*, paper Th3A.3, 2015.
- [109] A. H. Gnauck, and P. J. Winzer, "Optical Phase-Shift-Keyed Transmission," *Journal of Lightwave Technology* 23(1), 115-130, 2005.
- [110] S. Chandrasekhar, X. Liu, D. Kilper, C. R. Doerr, A. H. Gnauck, E. C. Burrows, and L. L. Buhl, "Terabit Transmission at 42.7-Gb/s on 50-GHz Grid Using Hybrid RZ-DQPSK and NRZ-DBPSK Formats Over 16 x 80 km SSMF Spans and 4 Bandwidth-Managed ROADMs," *Journal of Lightwave Technology* 26(1), 85-90, 2008.
- [111] K. Sato, S. Kuwahara, and Y. Miyamoto, "Chirp Characteristics of 40-Gb/s Directly Modulated Distributed-Feedback Laser Diodes," *Journal of Lightwave Technology* 23(11), 3790-3797, 2005.
- [112] S. Matsuo, T. Kakitsuka, T. Segawa, R. Sato, Y. Shibata, R. Takahashi, H. Oohashi, and H. Yasaka, "4x25 Gb/s Frequency-Modulated DBR Laser Array for 100-GbE 40-km Reach Application," *IEEE Photonics Technology Letters* 20(17), 1494-1496, 2008.

- [113] D. Che, F. Yuan, and W. Shieh, "100-Gb/s Complex Direct Modulation over 1600-km SSMF Using Probabilistic Transition Estimation," Optical Fiber Communication Conference, paper M3C.5, 2017.
- [114] C. R. S. Fludger, T. Duthel, D. V. den Borne, C. Schulien, E. D. Schmidt, T. Wuth, J. Geyer, E. D. Man, G.-D. Khoe, and H. D. Waardt, "Coherent Equalization and POLMUX-RZ-DQPSK for Robust 100-GE Transmission," Journal of lightwave technology 26(1), 64-72, 2008.
- [115] X. Liu, F. Buchali, and R. W. Tkach, "Improving the Nonlinear Tolerance of Polarization-Division-Multiplexed CO-OFDM in Long-Haul Fiber Transmission," Journal of Lightwave Technology 27(16), 3632-3640, 2009.
- [116] Y. Koizumi, K. Toyoda, M. Yoshida, and M. Nakazawa, "1024 QAM (60 Gbit/s) single-carrier coherent optical transmission over 150 km," Optics Express 20(11), 12508-12514, 2012.
- [117] R. Schmogrow, M. Winter, M. Meyer, D. Hillerkuss, S. Wolf, B. Baeuerle, A. Ludwig, B. Nebendahl, S. Ben-Ezra, J. Meyer, M. Dreschmann, M. Huebner, J. Becker, C. Koos, W. Freude, and J. Leuthold, "Real-time Nyquist pulse generation beyond 100 Gbit/s and its relation to OFDM," Optics Express 20(1), 317-337, 2012.
- [118] R. Rios-Müller, J. Renaudier, P. Brindel, H. Mardoyan, P. Jennevé, L. Schmalen, and G. Charlet, "1-Terabit/s Net Data-Rate Transceiver Based on Single-Carrier Nyquist-Shaped 124 GBaud PDM-32QAM," Optical Fiber Communication Conference, paper Th5B.1, 2015.
- [119] J. Cai, Y. Cai, C. Davidson, A. Lucero, H. Zhang, D. Foursa, O. Sinkin, W. Patterson, A. Pilipetskii, G. Mohs, and N. Bergano, "20 Tbit/s capacity transmission over 6,860 km", Optical Fiber Communication Conference, paper PDPB4, 2011.
- [120] A. Li, A. A. Amin, X. Chen, and W. Shieh, "Transmission of 107-Gb/s mode and polarization multiplexed CO-OFDM signal over a two-mode fiber", Optics Express 19(9), 8808-8814, 2011.
- [121] R. Ryf, S. Randel, A. H. Gnauck, C. Bolle, R. Essiambre, P. Winzer, D. W. Peckham, A. McCurdy, and R. Lingle, "Space-division multiplexing over 10 km of three-mode fiber using coherent 6×6 MIMO processing", Optical Fiber Communication Conference, paper PDPB10, 2011.
- [122] J. Sakaguchi, Y. Awaji, N. Wada, A. Kanno, T. Kawanishi, T. Hayashi, T. Taru, T. Kobayashi, and M. Watanabe, "109-Tb/s (7x97x172-Gb/s SDM/WDM/PDM) QPSK transmission through 16.8-km homogeneous multi-core fiber", Optical Fiber Communication Conference, paper PDPB6, 2011.
- [123] B. Zhu, T. Taunay, M. Fishteyn, X. Liu, S. Chandrasekhar, M. Yan, J. Fini, E. Monberg, and F. Dimarcello, "Space-, wavelength-, polarization-division multiplexed transmission of 56-Tb/s over a 76.8-km seven-core fiber", Optical Fiber Communication Conference, paper PDPB7, 2011.
- [124] A. Dochhan, L. Nadal, H. Griesser, M. Eiselt, M. S. Moreolo, and JP. Elbers, "Experimental Investigation of Discrete Multitone Transmission in the Presence of Optical Noise and Chromatic Dispersion," Optical Fiber Communication Conference, paper Tu2G.7, 2014.
- [125] A. J. Lowery, and J. Armstrong, "Orthogonal-frequency-division multiplexing for dispersion compensation of long-haul optical systems," Optics Express 14(6), 2079-2084, 2006.
- [126] WR. Peng, X. Wu, V. Arbab, B. Shamee, L. Christen, J. Yang, K. Feng, A. E. Willner, and S. Chi, "Experimental Demonstration of a Coherently Modulated and Directly Detected Optical OFDM System Using an RF-Tone Insertion," Optical Fiber Communication Conference, paper OMU2, 2008.
- [127] WR. Peng, X. Wu, K. Feng, V. R. Arbab, B. Shamee, J. Yang, L. C. Christen, A. E. Willner, and S. Chi, "Spectrally efficient direct-detected OFDM transmission employing an iterative estimation and cancellation technique," Optics Express 17(11), 9099-9111, 2009.

- [128] WR. Peng, I. Morita, H. Takahashi, and T. Tsuritani, "Transmission of High-Speed (> 100 Gb/s) Direct-Detection Optical OFDM Superchannel," *Journal of Lightwave Technology* 30(12), 2025-2034, 2012.
- [129] X. Xiao, T. Gui, S. You, Q. Yang, R. Hu, Z. He, M. Luo, C. Li, X. Zhang, D. Xue, Z. Li, X. Chen, and S. Yu, "432 Gb/s Direct-Detection Optical OFDM Superchannel Transmission Over 3,040 km SSMF," *Advanced Photonics Congress*, paper NW2C.3, 2013.
- [130] X. Chen, A. Li, D. Che, Q. Hu, Y. Wang, J. He, and W. Shieh, "Block-wise phase switching for double-sideband direct detected optical OFDM signals," *Optics Express* 21(11), 13436-13441, 2013.
- [131] B. J. C. Schmidt, Z. Zan, L. B. Du, and A. J. Lowery, "120 Gbit/s Over 500-km Using Single-Band Polarization-Multiplexed Self-Coherent Optical OFDM," *Journal of lightwave technology* 28(4), 328-335, 2010.
- [132] D. Che, X. Chen, J. He, A. Li, and W. Shieh, "102.4-Gb/s Single-Polarization Direct-Detection Reception using Signal Carrier Interleaved Optical OFDM," *Optical Fiber Communication Conference*, paper Tu3G.7, 2014.
- [133] D. Che, H. Khodakarami, and W. Shieh, "Dual-Polarization Signal Carrier Interleaved Direct Detection Through Discrete-time Gaussian Channel with Conjugate Inter-symbol Interference," *Opto Electronics and Communications Conference*, 2015.
- [134] Z. Li, M. S. Erkilinc, S. Pachnicke, H. Griesser, R. Bouziane, B. C. Thomsen, P. Bayvel, and R. I. Killey, "Signal-signal beat interference cancellation in spectrally-efficient WDM direct-detection Nyquist-pulse-shaped 16-QAM subcarrier modulation," *Optics Express* 23(18), 23694-23709, 2015.
- [135] W. Hirt and J. L. Massey, "Capacity of the discrete-time Gaussian channel with intersymbol interference," *IEEE Transactions on Information Theory* 34(3), 380-388, 1988.
- [136] D. Che, X. Chen, A. Li, and W. Shieh, "Signal-Carrier Interleaved Direct-Detection in Optical Single-Carrier Communication Systems," *OptoElectronics and Communication Conference*, paper WE8D-1, 2014.
- [137] D. Che, and W. Shieh, "Polarization demultiplexing for Stokes vector direct detection," *Journal of Lightwave Technology* 34(2), 754-760, 2016.
- [138] M. Morsy-Osman, M. Chagnon, M. Poulin, S. Lessard, and D. V. Plant, "1 λ \times 224 Gb/s 10 km Transmission of Polarization Division Multiplexed PAM-4 Signals Using 1.3 μ m SiP Intensity Modulator and a Direct-Detection MIMO-based Receiver," *European Conference on Optical Communication*, paper PD4.4, 2014.
- [139] M. Chagnon, M. Osman, D. Patel, V. Veerasubramanian, A. Samani, and D. Plant, "1 λ , 6 bits/symbol, 280 and 350 Gb/s Direct Detection Transceiver using Intensity Modulation, Polarization Multiplexing, and Inter-Polarization Phase Modulation," *Optical Fiber Communication Conference*, paper Th5C.2, 2015.
- [140] J. Estarán, M. Usuga, E. Porto da Silvia, M. Piels, M. Iglesias Olmedo, D. Zibar, and I. Tafur Monroy, "Quaternary polarization-multiplexed subsystem for high capacity IM/DD optical data links," *Journal of Lightwave Technology* 33(7), 1408-1416, 2015.
- [141] B. Szafraniec, B. Nebendahl, and T. Marshall, "Polarization demultiplexing in Stokes space," *Optics Express* 18(17), 17928-17939, 2010.
- [142] G. H. Golub, and C. Reinsch, "Singular value decomposition and least squares solution," *Numer. Math.* 14(5), 403-420, 1970.

- [143] A. Li, D. Che, X. Chen, and W. Shieh, "Spectrally efficient optical transmission based on Stokes vector direct detection," *Optics Express* 22(13), 15662-15667, 2014.
- [144] K. Kikuchi, "Simple and Efficient Algorithm for Polarization Tracking and Demultiplexing in Dual-polarization IM/DD Systems," *Optical Fiber Communication Conference*, paper Th1E.3, 2015.
- [145] N. J. Muga, and A. N. Pinto, "Adaptive 3-D Stokes Space-Based Polarization Demultiplexing Algorithm," *Journal of Lightwave Technology* 32(19), 3290-3298, 2014.
- [146] M. Visintin, G. Bosco, P. Poggiolini, and F. Forghieri, "Adaptive Digital Equalization in Optical Coherent Receivers With Stokes-Space Update Algorithm," *Journal of Lightwave Technology* 32(24), 4157-4165, 2014.
- [147] D. Che, A. Li, X. Chen; Q. Hu, Y. Wang, and W. Shieh, "Stokes vector direct detection for short-reach optical communication", *Optics Letters* 39(11), 3110-3113, 2014.
- [148] D. Che, Q. Hu, X. Chen, A. Li, and W. Shieh, "1-Tb/s Stokes Vector Direct Detection over 480-km SSMF Transmission," *OptoElectronics and Communication Conference*, paper THDP1-3, 2014.
- [149] Q. Hu, D. Che, Y. Wang, and W. Shieh, "Advanced modulation formats for high-performance short-reach optical interconnects," *Optics Express* 23(3), 3245-3259, 2015.
- [150] D. Che, F. Yuan, and W. Shieh, "200-Gb/s Polarization-Multiplexed DMT using Stokes Vector Receiver with Frequency-Domain MIMO," *Optical Fiber Communication Conference*, paper Tu3D.4, 2017.



Minerva Access is the Institutional Repository of The University of Melbourne

Author/s:

Che, Di

Title:

Coherent optical short-reach communications

Date:

2016

Persistent Link:

<http://hdl.handle.net/11343/129708>

File Description:

Coherent optical short-reach communications

Terms and Conditions:

Terms and Conditions: Copyright in works deposited in Minerva Access is retained by the copyright owner. The work may not be altered without permission from the copyright owner. Readers may only download, print and save electronic copies of whole works for their own personal non-commercial use. Any use that exceeds these limits requires permission from the copyright owner. Attribution is essential when quoting or paraphrasing from these works.